DEVELOPMENT AND APPLICATION OF A PULSED IONIZATION CHAMBER-BASED MULTIPROBE PLASMA DIAGNOSTIC SYSTEM

By

WON YOUNG CHOI

A DISSERTATION PRESENTED TO THE GRADUATE SCHOOL OF
THE UNIVERSITY OF FLORIDA
IN PARTIAL FULFILLMENT OF THE REQUIREMENTS FOR THE
DEGREE OF DOCTOR OF PHILOSOPHY

UNIVERSITY OF FLORIDA
1991

TO

MY PARENTS

ACKNOWLEDGEMENTS

The author wishes to express his sincere gratitude for the guidance and encouragement received from Dr. William H. Ellis as the chairman of his supervisory committee. He is also grateful to Dr. Isaac Maya and the Innovative Nuclear Space Power Institute for the academic and financial support. He is deeply indebted to the other members of his supervisory committee, Dr. Samim Anghaie, Dr. William G. Vernetson, Dr. Robert J. Hanrahan, Dr. Calvin C. Oliver for their interest, support and many constructive comments on the work.

Appreciation is also expressed to the staff members of the University of Florida Training Reactor for the many hours spent in system installation and reactor operation. Dr. J.S. Park and Mr. S. Huh made many contributions to the sophisticated electronics development. Thanks are also extended to the staff members of the Microcalvin Lab. of the Physics Department for their help to use the liquid helium cold trap facility.

Acknowledgment is expressed for financial support received from the Department of Nuclear Engineering Sciences, the Innovative Nuclear Space Power Institute, and the Department of Physics at the University of Florida.

Finally, words fail to express the thanks which is extended to the author's wife, Haeja. Her patience, love and support in this long endeavor proved to be the difference between success and failure.

TABLE OF CONTENTS

page

ACKNOWLEDGEMENTS iii

LIST OF TABLES vii

LIST OF FIGURES viii

KEY TO SYMBOLS xiii

ABSTRACT xv

CHAPTERS

1. INTRODUCTION.. 1

2. NUCLEAR-GENERATED PLASMA KINETICS.................... 13

   2.1. Nuclear-Generated Plasma Kinetics 14
      2.1.1. Plasma Generation Processes 16
      2.1.2. Plasma Loss Processes 19
         2.1.2.1. First order loss mechanism 19
         2.1.2.2. Second order loss mechanism 21

3. DEVELOPMENT OF AN IMPROVED PULSED IONIZATION CHAMBER (PIC) SYSTEM AND ITS APPLICATION TO NUCLEAR-GENERATED PLASMA DIAGNOSTICS 25

   3.1. Pulsed Ionization Chamber (PIC) System 25
      3.1.1. Operational Principle of PIC Technique 27
      3.1.2. Development of a New PIC System 31

   3.2. PIC Plasma Diagnostic Experiments 46
      3.2.1. Experimental Method 46
      3.2.2. Data Acquisition and Analysis 48

   3.3. Experimental Results and Discussion 60
      3.3.1. Plasma Source Production Rate 62
      3.3.2. Plasma Loss Coefficient 67
      3.3.3. Discussion 82

4. DEVELOPMENT OF MULTIPROBE IONIZATION CHAMBER (MPIC) PLASMA DIAGNOSTIC SYSTEM 89

4.1. Design and Construction of Multiprobe Ionization Chamber System 89
4.1.1. Description of MPIC 91
4.1.2. Theory of Measurement 103
4.1.3. Multiprobe Ionization Chamber System Electronics 109

4.2. Multiprobe Ionization Chamber Preliminary Test 127
4.2.1. Multiprobe Ionization Chamber Preparation 127
4.2.2. Multiprobe Ionization Chamber Characteristics Measurements 129

4.3. Multiprobe Ionization Chamber Performance Test and Validation 137
4.3.1. Multiprobe Ionization Chamber Test Using the Co-60 Irradiator 137
4.3.2. Multiprobe Ionization Chamber Test Using the UFTR 147
4.3.3. Discussions 161

5. CONCLUSIONS 165

APPENDICES

A. PIC SYSTEM ELECTRONICS 170

B. SAFETY REPORT SUBMITTED TO UFTR SAFETY COMMITTEE 189

C. LABVIEW PROGRAMS 217

LIST OF REFERENCES 233

BIOGRAPHICAL SKETCH 237

LIST OF TABLES

Table .... Page

3.1. Specifications of the Ionization Chambers Used in the PIC Plasma Diagnostic System 38

3.2. Summary of 1st Order Loss Results 68

3.3. Summary of 2nd Order Loss Results 73

3.4. Summary of Mobility Results of He(UF_6) Gas 73

4.1. MPIC Parts List 93

4.2. Multiprobe Ionization Chamber Specifications 94

4.3. Specifications of High Voltage Pulser 114

4.4. Mode Selection by Manual Switch 119

B.1 Activation of Experimental Assembly Materials 201

B.2. Measured Reactivity Contribution to the UFTR by inserting an experimental assembly 203

B.3 Activation of Type 304 S.S.(7640 g) 210

B.4 Activation of Aluminum (7450 g) 210

B.5 Activation of Molybdenum (398 g) 210

B.6 Activation of Alumina (1000 g) 210

B.7: Fission Products from Fast Fission of U^{238} at the Fast Flux of 10^{10} n/cm^2-sec for 6 hrs 213

B.8: Fission Products from Thermal Fission of U^{235} at the Thermal Flux of 10^{10} n/cm^2-sec for 6 hrs 213

LIST OF FIGURES

Figure Page

1.1 Bimodal Gas Core Reactor Power System 3

3.1 Operation of System Electronics (PIC mode) 28

3.2 Block Diagram of the PIC System 33

3.3 Electronic Circuit Diagram for the PIC System (Pulse Generator and Timing Circuit) 34

3.4 Electronic Circuit Diagram for the PIC System (HV Pulser and HI Switching Circuit) 35

3.5 A Photograph of the PIC system circuitry 37

3.6 Dimensions of Ion Chamber Filled with He(UF_6) 40

3.7 Heater Assembly 41

3.8 Gas Purge System 43

3.9 Ionization Chamber Housing and Heater Assembly 44

3.10 PIC Plasma Diagnostics Plot at 573 K Using Co-60 Source, 1 Atm He(1.0% UF_6) 50

3.11 1st Order Loss Coefficient at 573 K Using Co-60 Source, 1 Atm He(1.0% UF_6) 52

3.12 PIC Plasma Diagnostics Plot at 453 K Using the UFTR, 1 atm He(3.9% UF_6) 53

3.13 2nd Order Loss Coefficient Analysis Plot using the UFTR, 1 atm He(3.9% UF_6) 55

3.14 T-dependency of 2nd Order Loss Coefficient using the UFTR, 1 atm He(3.9% UF_6) 56

3.15 Typical PIC Voltage Pulse; (a)Electron (b)ion Collection.. 58

3.16 Electrical Conductivity Calculated by PIC Measurement at 453K using UFTR, 1 atm He(3.9% UF_6) ... 59

3.17 PIC Plasma Diagnostics Plot at Room Temperature Using Co-60 Source, Rare Gases (He, Ar, Xe) 61

3.18 Ionization Source Rate Measured by using UFTR, 1 atm He(0.1% UF_6) 63

3.19 Ionization Source Rate Measured by using UFTR, 1 atm He(1.0% UF_6) 64

3.20 Ionization Source Rate Measured by using UFTR, 1 atm He(3.9% UF_6) 65

3.21 Ionization Source Rate Measured by using UFTR, 1 atm He(7.5% UF_6) 66

3.22 2nd Order Loss vs Temperature Plot using the UFTR, 1 atm He(varying UF_6 percentages) 69

3.23 2nd Order Loss vs Temperature Plot using the Co-60 Source, 10 atm He(Fission Chamber)................... 71

3.24 2nd Order Loss vs Temperature Plot using the Co-60 Source, 20 atm N_2 72

3.25 Electrical Conductivity vs Neutron Flux Plot using the UFTR, 931 torr He(0.1% UF_6) 74

3.26 Electrical Conductivity vs Neutron Flux Plot using the UFTR, 981 torr He(1.0% UF_6) 75

3.27 Electrical Conductivity vs Neutron Flux Plot using the UFTR, 960 torr He(3.9% UF_6) 76

3.28 Electrical Conductivity vs Neutron Flux Plot using the UFTR, 981 torr He(7.5% UF_6) 77

3.29 Electron Density vs Source Rate Curve for 10 atm He Filled Fission Chamber in UFTR Compared with N-S Curve in Co-60 Source 80

3.30 Comparison of N vs S for with and without Fission Fragments in the UFTR, (1 atm Ar(5% N_2) Fission Chamber) 81

3.31 2nd Order Plasma Loss Coefficient Obtained from 10 atm He Ionized with Fission Fragment and γ-Rays 83

4.1 MPIC and Chamber Housing 92

4.2 Anode and Guard Electrodes Detail 95

4.3 Photographs of the MPIC System; a) assembled MPIC b) Cathode and Guard Electrodes 96

4.4 Experimental Assembly Inserted In the Thermal Column of the UFTR 97

4.5 Resistivity vs Temperature For Typical MgO Type I Test Cable 99

4.6 Block Diagram of Computer Controlled Multiprobe Plasma Diagnostic System 104

4.7 Semi-log Langmuir Cylindrical Probe Plot of Probe Current Against Probe Voltage 107

4.8 Electronic Circuit Diagram for the MPIC System 110

4.9 Electronic Circuit Diagram for the MPIC System (continued) 111

4.10 Circuit Diagram for Conductivity Measurement 112

4.11 Timing Diagram For the High Voltage Pulse and High Impedance Switching 116

4.12 Impedance Switching Transistor and Capacitance Compensation Circuit 121

4.13 Waveform at the Collector of Transistor (TR-4) Without Compensation 121

4.14 Typical Triangular-Wave Generator Output Waveform 124

4.15 Photographs of the MPIC System; (a) System Layout (b) MPIC Circuitry 126

4.16 Resistance vs Time Plot During Heating and Cooling of ZIRCAR AL30AA Alumina 128

4.17 Measurement of Electrical Resistance Between the Probes of MPIC 131

4.18 Measured Resistance Between the Probes of MPIC 132

4.19 Temperature vs Time Plot at the Center of the MPIC and Outside Wall of Coolant Tube (Coolant Flow Rate = 5 g/sec) 134

4.20 Leakage Current Measured as a Function of Inside Temperature of the MPIC 136

4.21 Characteristic I-V Curve of the MPIC (1 atm He) 139

4.22 Typical PIC Voltage Signal From the 1 atm He Filled MPIC 140

4.23 PIC Plasma Diagnostic Plot Using Co-60 Source, 1 atm He Filled MPIC 141

4.24 Electron Density vs Ionization Source Rate Using Co-60 Source, 1 atm He Filled MPIC 142

4.25 Electrical Conductivity vs Ionization Source Rate Using Co-60 Source, 1 atm He Filled MPIC 144

4.26 2nd Loss CoefficientUsing Co-60 Source, 1 atm He Filled MPIC 145

4.27 Gas Filling System 148

4.28 A Photograph of the MPIC Experimental Assembly 149

4.29 PIC Plasma Diagnostic Plot Using the UFTR Source, 16.7 psi He (3.5% ^{3}He) Filled MPIC 151

4.30 PIC Signal Voltage Profies With & Without Negative Ion Presence.......... 153

4.31 Electrical Conductivity vs Ionization Source Rate 16.7 psi He (3.5% ^{3}He) Filled MPIC 156

4.32 Conductivity Probe Measurement Results, 16.7 psi He (3.5% ^{3}He) Filled MPIC 157

4.33 Electrical Conductivity Measured by the Conductivity Probe, 16.7 psi He (3.5% ^{3}He) Filled MPIC 158

4.34 Langmuir Probe Measurement Results, 16.7 psi He (3.5% ^{3}He) Filled MPIC 160

A.1 Block Diagram of the PIC System 171

A.2 Circuit Diagram of the PIC System (Pulse Generator and Timing Circuit) 173

A.3 Pulse Generator Timing Diagram 174

A.4 Circuit Diagram of the PIC System (HV Pulser and HI Switching Circuit) 177

A.5 High Voltage Pulser Timing Diagram 178

A.6 MOSFET Switching 181

A.7 Timing Relationship Between the High Voltage Pulse and the Impedance Switching Signal. 181

A.8 Timing Diagram of the Impedance Switching Signal Generator 183

A.9 Impedance Switching Transistor and the Capacitance Compensation Circuit 184

A.10 Waveform at the Collector of the Transistor (TR-4) Without Compensation 184

A.11 Installation of the PIC system 187

B.1 Multiprobe Ionization Chamber 192

B.2 Experimental Assembly Inserted In the Thermal Column of the UFTR.................................. 193

B.3 Gas Purge System 195

B.4 Cross-sectional View of the Experimental System 214

C.1 Program "485 Picoammeter" 220

C.2 Program "Running 485" 222

C.3 Program "Voltage at Time" 223

C.4 Program "Running 2430" 226

C.5 Program "PIC Instrument" 227

C.6 Program "113DR DDG" 229

C.7 Program "Conductivity Probe" 230

KEY TO SYMBOLS

α_1 = first order plasma loss coefficient [/sec]
α_2 = second order plasma loss coefficient [m^3/sec]
a = radius of inner electrode of coaxial chamber [m]
b = radius of outer electrode of coaxial chamber [m]
C = anode load capacitance [F]
D = diffusion coefficient [m^2/sec]
e = electron charge = 1.6×10^{-19} [Coulomb]
E = electric field [V/m]
f.f.= fission fragment (or fast ion)
h = Planck's constant = 6.62×10^{-34} [J-sec]
I_s = saturation current of ion chamber [A]
J = current density [A/m^2]
k = Boltzmann constant = 1.38×10^{-23} [J/K]
m_e = electron mass = 9.11×10^{-31} [kg]
Λ = characteristic diffusion length [m]
λ_D = Debye shielding length [m]
n_e = electron density [/m^3]
n_i = ion density [/m^3]
n^+ = positive ion density [/m^3]
n^- = negative ion density [/m^3]
n_a = neutral particle density [/m^3]
ϕ_f = fast neutron flux [/cm^2-sec]
ϕ_{th} = thermal neutron flux [/cm^2-sec]

S = ionization source generation rate [$/m^3$-sec]

σ = electrical conductivity [S/m]

t_c = PIC signal collection time [sec]

T_g = gas temperature [K]

T_e = electron temperature [K]

T_i = ion temperature [K]

μ_e = electron mobility [m^2/V-sec]

μ_i = ion mobility [m^2/V-sec]

U = sensitive volume of an ionization chamber [m^3]

Abstract of Dissertation Presented to the Graduate School
of the University of Florida in Partial Fulfillment of the
Requirements for the Degree of Doctor of Philosophy

DEVELOPMENT AND APPLICATION OF A PULSED IONIZATION CHAMBER-BASED MULTIPROBE PLASMA DIAGNOSTIC SYSTEM

By

Won Young Choi

December, 1991

Chairman: Dr. William H. Ellis
Major Department: Nuclear Engineering Sciences

An experimental system based on the Pulsed Ionization Chamber (PIC) technique was developed and applied to the investigation of the characteristics of nuclear-generated plasmas, which are related to critical engineering design parameters of uranium fluoride based gas-core reactor/MHD converter systems. Plasma parameters measured included ionization production rate, recombinational loss coefficient, electron density, mobility, and electrical conductivity for plasmas containing various concentration of UF_6 and rare gases such as He, Ar and Xe. The measurements demonstrated the advantage of the PIC technique in obtaining multiple plasma

simultaneously. The PIC system was subsequently upgraded to the Multi-Probe Ionization Chamber (MPIC) to improve its capabilities and to extend its range of measurement to higher plasma densities and temperatures by providing with it additional measurement features in the form of conductivity and Langmuir probes. To accommodate these additional capabilities and to obtain complete automation of experiment, a technique was developed for remote switching between several GPIB instruments controlled by a software system.

Performance tests of the MPIC system using both ^{60}Co and ^{3}He(n,p)T ionization sources showed that the chamber functions according to design. Of particular importance, leakage current, the limiting factor in high temperature chamber operation, was negligible at temperature of 1000K due to the new electrode design. In addition, the responses of the three measurement features (PIC, Conductivity, Langmuir) exhibit regions of overlap under high plasma density conditions with good agreement and reproducibility.

At higher pressures and for electronegative species such as UF_6, evidence of cluster formation was observed with an approximate T^{-4} plasma loss temperature dependence. The measured electrical conductivity of 1 atm He(1% UF_6) gas was in the range of 5×10^{-7} to 1×10^{-4} (S/m) over the thermal neutron flux range of 5×10^{8} to 7×10^{11} (n/cm^2-sec) and temperatures of 523 K to 723 K. At these temperatures, the measured conductivity was somewhat low and would not be sufficient to support useful electrical conversion for

GCR/MHD systems. The principal cause for low conductivity appeared to be due to electron attachment to UF_6 and its decomposition products. However, extension of these measurements to the higher temperatures of system's capability should provide useful information with respect to temperature dependent trends by which extrapolation to higher temperature could be performed.

CHAPTER 1
INTRODUCTION

The uranium fluoride gas core reactor/MHD converter concept for space power has been pursued and developed through the conceptual design stage at the University of Florida's Innovative Nuclear Space Power Institute (INSPI) [1]. Parametric and design studies of such complex systems require the availability of and access to reliable and accurate parametric resources. Often, however, dependable values of such needed parameters are not readily available, making it necessary for new experimental tools, techniques and facilities to be developed for their measurement and evaluation. Such is true for the innovative gas core reactor/MHD converter concepts pursued by INSPI, where the enhancement of the electrical conductivity of the uranium fluoride fuel gas/MHD working medium by fission fragment induced ionization is a critical issue with respect to attaining a more efficient MHD electrical power generation with the system [1]. To be able to design, develop and evaluate properly the role that nuclear induced ionization can play therein, more accurate information is needed with respect to the fission plasma source term, attained ionization densities, electron/ion temperatures, realistic plasma loss coefficients, electron/ion drift velocities, as well as electrical conductivities. An example of such a reactor system [2] is illustrated in Figure 1, where the reactor utilizes a gaseous uranium compound or uranium vapor as its fuel. To achieve criticality, the core would be surrounded by a reflector such as beryllium. The working fluids proposed for these systems have been either an inert gas such as helium or alkali metal vapor such as potassium. Closed Rankine cycle or Brayton cycle systems have been proposed for electrical power generation. As customary, a Brayton cycle would be used when the working fluid remains in the gaseous state at all times.

Achievement of a sufficient level of conductivity in the working fluid is one of the basic problems in MHD power generation technology. Since, for a given ionization density, the output power of a MHD generator is proportional to the square of the flow velocity [3], use of working fluids of low molecular mass is essential, where helium is preferred. However, helium requires the highest ionization energy of all the elements. Thus, if thermal ionization alone is to be used, it would be necessary to add a seed material such as potassium or cesium which have low ionization energy. This, of course, causes an additional problem such as the need for seed recovery. Thereby, it would be advantageous to use a working fluid which has both a low molecular weight and a low ionization energy. ^{3}He gas using the ^{3}He(n,p)t reaction has been proposed as a potential candidate for the needed nuclear ionization source [4,5].

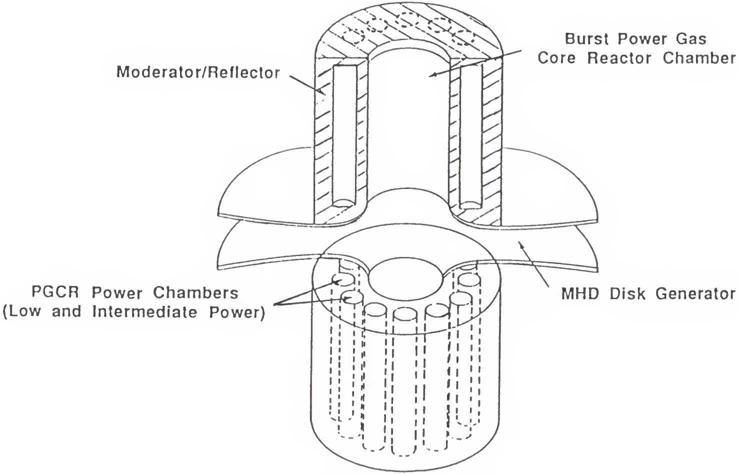

Figure 1.1: Bimodal Gas Core Reactor Power System

However, an alternative would be gaseous uranium with the $^{235}U(n,fission)f.f.$ reaction as an ionization source since it has much higher reaction energy than that of the $^{3}He(n,p)t$ reaction. Early on, UF_6 was considered as a prime component of fuel gas for the reactor since it is the only chemical compound of uranium available that is a gas at close to room temperature.

It is essential to have as good an understanding of the behavior of the plasma in the gas core reactor/MHD converter system as possible, especially since electronegative species such as UF_6, its decomposition products and fluorine can play a major role in determining the ultimate utility of such a system. The presence of these species constitutes a major problem with respect to producing sufficient numbers of electrons in such a gas, that would provide adequate levels of electrical conductivity, thereby to assure efficient MHD generator operation. For the above examples, the electrical conductivity of the plasma in the MHD channel is determined primarily by the conditions established in the fissioning gas core and subsequent processes occurring in the generator channel. Therefore, large errors or uncertainties in the values of characteristic parameters of the candidate reactor fuel and working fluids, and in particularly at high temperature (1500 K ~ 4000 K) and high pressure (1 ~ 100 atm), lead to similar uncertainties in the operational characteristics of such systems and in the properties of the materials and systems under study, making it difficult or impossible to arrive at a definitive set of operational and design characteristics.

The critical physical issue in the design problem is whether or not high enough electron densities can be produced in the UF_6 gas mixture by fissioning and subsequent ionizations by fission fragments, or whether the enhanced ionization rate due to fission fragments will be diminished and overcome by electron attachment due to the high electron affinity characteristics of the uranium fluoride and its dissociative molecular components, as well as elemental fluorine, which will exist under the expected conditions. To resolve this problem, one needs a set of values for the parameters that influence the nuclear ionization source, the plasma loss coefficients (diffusion, electron attachment, recombination) and the electrical conductivity of the plasma of interest as functions of both temperature and pressure.

To date, there are only a few measurements reported in the literature on the characteristics of plasmas generated by nuclear enhanced ionization techniques. Braun et al. [4] measured the electrical conductivity of helium plasmas generated by the $^3He(n,p)T$ nuclear reaction at temperatures up to 1600 K and at pressures at or near 1 atmosphere. Later, the same group [6] measured the electrical conductivity of a helium mixture afterglow plasma, which was generated by means of an electrical discharge, over a gas pressure range of 1-8 atms. They used a direct conductivity measurement technique that involved the determination of the total plasma resistance from which the plasma electrical conductivity was calculated. Subsequently, when the dimensions of the plasma were determined, an average value for the conductivity could be computed, based on the best estimate of the dimensions of the active plasma region. Use of the latter method was limited to the measurement of the electrical conductivity. Of the other important parameters, only the plasma density could be deduced from the value measured for the electrical conductivity. Leffert et al.[7,8] reported the generation of plasmas by fission fragment ionization of noble gases. They calculated the ion generation rate from the energy loss rate of the fission fragments in the gas. Deese and Hassan [9] developed a theoretical model for characterizing plasmas generated by high energy fission fragments and for use in the analysis of nuclear pumped lasers. Ellis and Imani [10] studied the kinetics of fission fragment, $^3He(n,p)T$ and γ-ray produced plasmas in high pressure (1-27 atms) rare gases such as He and Ar, using the pulsed ionization chamber technique which will be discussed later in detail.

Since UF_6 gas is toxic and highly corrosive, few, if any, results have been reported on the measurement of its electrical conductivity generated by nuclear method, particularly at high temperatures and pressures. However, the role of UF_6 seeding in lightly ionized argon plasmas was studied by J.C. Wu et al. [11]. They concluded that when a trace amount of UF_6 (0.025% of Argon gas) was added to lightly ionized Ar plasmas, the electron density was reduced by as much as 98 percent. In this example, however, UF_6 was not a component of the gas when it was initially subjected to the electron ionization source, but rather was added later, downstream as the plasma relaxed. More recent studies on the loss characteristics of UF_6 plasma electron loss by Ellis and Baumgartner [12] showed similar electron loss results.

Several different methods of simulating the gas core reactor conditions using UF_6 gas have been reported. Krascella [13] conducted an experimental study to determine the spectral characteristics of UF_6 and possible UF_6 thermal decomposition products as a function of temperature and pressure. He used a plasma torch-optical plenum assembly, and the monochromator to generate and investigate high temperature (800 ~ 3600 K) UF_6/Ar mixture plasma. Roman [14] also investigated the properties of UF_6/Ar mixture plasmas, but he used the RF induction heating method and could reach plasma temperatures of 9600 K. He was able to determine the radial variation of total uranium atom density within the RF plasma based on the measurement of line emission and absorption of uranium plasma. A unique approach to simulate a gas core reactor condition was reported by Lee et al. [15]. They used the dense plasma focus (DPF) technique to generate a localized uranium plasma in a focussed column of the DPF device and measured plasma emission characteristics. However, none of the methods described above could provide a means for investigating the kinetics of UF_6 plasmas under gas core reactor operational conditions.

Therefore, if serious engineering design work is to be undertaken for a gas core reactor/MHD converter system, there needs to be a strong parallel experimental effort that can provide pertinent information on the plasma kinetic parameters for not only the components of the principal candidate system under consideration for the GCR/MHD converter system but also for mixtures thereof. One needs to have information that has been obtained under conditions that duplicate or closely emulate those of the actual reactor/MHD converter environments anticipated, or, at least of such a nature that it can be logically and realistically extrapolated into the regions of interest. One such system that offers to provide information on the plasma loss coefficients of nonequilibrium plasmas, especially those produced in high pressure gases by nuclear radiations, is the pulsed ionization chamber (PIC) technique developed and investigated by Ellis et al. [10,16,17] at the University of Florida.

The PIC technique has been successfully used to measure steady state plasma generation and loss rates, and the mobility of electrons and ions in nuclear-induced ionized gas. Further, by using measured parameters, one can also calculate the electrical conductivity of the plasma. The nature of the experimental circumstances of the PIC technique, which utilizes a variety of ionization chambers exposed to radiation sources (neutrons and/or gammas), can be a good simulation of the gas core reactor environment. Therefore, the PIC technique appears to meet most, if not all, of the elements of the experimental system necessary for studying nuclear-induced plasmas in high pressure gaseous media.

However, some problems encountered during the high temperature, high density plasma diagnostics measurements with the PIC system needed to be resolved [16]. Thus, the main goal in initiating the research described in the subsequent chapters of this dissertation was further development of the PIC system and its upgrade in the form of a PIC-based Multiprobe Ionization Chamber (MPIC) system, and its application to the study of characteristics of nonequilibrium plasmas generated by nuclear method using candidate gases for GCR/MHD systems. The MPIC system has additional probes to increase the capabilities and extend the range of measurements to higher temperatures and densities.

In order to establish an initial base on which to develop the research topic, the general aspects of nuclear-generated plasma kinetics are discussed in the following chapter with emphasis placed on the study of plasmas generated in UF_6 and ^3He gases.

In CHAPTER 3, the development of a nuclear-generated plasma diagnostic system based on the PIC technique and its application is presented in detail, including a review of the PIC system's basic operational characteristics. The PIC plasma diagnostic system is based on state-of-the-art electronics that was designed and developed as a part of the research. Its performance as a versatile plasma diagnostic tool, particularly for the plasma generated by nuclear methods, has been evaluated by studying selected series of fuel and buffer gas compositions (UF_6, He, Ar, Xe, etc.). Both the University of Florida Training Reactor (UFTR) and the ^{60}Co irradiator have been used as nuclear ionization sources for the study. The parameters measured include plasma source generation rate, plasma loss coefficients (diffusion and recombination), plasma density, electron/ion mobility and electrical conductivity. Fission chambers filled with helium and argon, which are the most highly recommended buffer gases for the gas core reactor, have been used for the study of buffer gas plasmas characteristics for those generated by fission fragment. These measurements were also aimed at verifying earlier reports on the enhanced columnar recombination loss of the plasmas which were generated by heavy charged particles such as fission fragments. For the study of candidate fuel and buffer gas mixtures, UF_6 gas mixed with a helium buffer gas was also investigated using the newly developed PIC plasma diagnostic system. The main property of the He(UF_6) gas investigated was electrical conductivity of the gas as a function of the neutron flux and gas temperature.

In CHAPTER 4, the development of the concepts and implementation of a computerized multiprobe ionization chamber (MPIC) plasma diagnostic system are presented. The multiprobe ionization chamber has been developed as a further extension of the PIC system, complemented by conventional plasma diagnostic techniques (conductivity probe and Langmuir (or electrostatic) probe). The principal idea behind this concept is to provide redundant methods which can be used to verify or cross-check the PIC measurement results, as well as to provide capabilities which the PIC technique may not be applicable. The conductivity probe is designed to measure the electrical conductivity of the plasma directly. The Langmuir probe can provide information on plasma density, temperature and electron energy distribution.

The multiprobe plasma diagnostic system that was developed as a part of this research consists of the multiprobe ionization chamber, associate electronics including computer-controlled data acquisition and analysis and subsidiary experimental system. The multiprobe ionization chamber which was designed to perform measurements at higher temperature than that which was used during earlier PIC measurements, was able to meet design requirement by incorporating a unique guard electrode design and thereby reducing leakage current at such elevated gas temperatures. The detailed description of the design and fabrication, as well as evaluation procedures for the multiprobe ionization chamber is also presented in this chapter. Evaluation of the multiprobe plasma diagnostic system's overall capabilities was performed using both ^{60}Co irradiator and UFTR with the chamber filled with ^{4}He and/or ^{3}He gas.

Finally, in CHAPTER 5, the author's conclusions are put forward and areas requiring additional research are stated.

Associated work supporting the research topic are presented in Appendices. Appendix A has detailed descriptions of the PIC system electronics. Presented in Appendix B is a safety report for the use of the experimental assembly in the UFTR. Appendix C includes a brief introduction of LabVIEW software and programs developed for data acquisition and analysis for the multiprobe plasma diagnostic system.

CHAPTER 2

NUCLEAR-GENERATED PLASMA KINETICS THEORY

The plasma diagnostic experiments that were undertaken during the dissertation research program can be briefly described as follows; ionization chambers, equipped with conventional and/or special probes and filled with either a He(UF_6) fissionable gas or a ^{3}He gas mixture, and exposed to a volumetric neutron source (UFTR) were used to simulate gas core reactors with the above gases serving as the working fluids. Under neutron bombardment, reactions with the active components (^{235}U, ^{3}He) yield fission fragments or fast ions which are generated volumetrically within the chamber. The slowing down of these charged particles results in energy being transferred to the electrons, causing ionization and excitation of the gas, resulting in nonequilibrium ionization of the fill gas (thermal equilibrium ionization is not expected to contribute significantly under the temperature conditions of the experiments). Measurements were then performed with the plasmas produced therein, to obtain values for the experimental plasma production and loss coefficients, as well as other pertinent plasma parameters, such as electrical conductivity and electron temperature. The parameters were evaluated to determine whether or not a sufficiently high electrical conductivity could be attained in the gas fill to be used as an input to an MHD converter.

In order to provide a foundation on which the experiments could be based, the general aspect of nuclear generated plasma kinetics, with emphasis on the fissioning plasma generated by using He(UF_6) and ^{3}He gas, are presented below.

2.1. Nuclear-Generated Plasma Kinetics

The concentration (or density) of a plasma in any ionized gas is a function of a balance established between the production and loss processes and can be represented most easily by a balance equation of the form:

$$\frac{dn}{dt} = S - \sum_{i=1}^{\infty} \alpha_i n^i \qquad (2.1)$$

where S represents the ionization source rate (#ion pairs/m^3-sec) and the loss rate is represented by a summation over a series of i-th ordered loss terms.

The first order ion loss is a depletion process which typically is dependent only on a single ionic species, usually in the form of diffusion to the wall and/or electron loss by attachment to electronegative species such as oxygen or halogen molecules. It is convenient to consolidate all of these first order loss processes under one coefficient,

$$\frac{dn}{dt} = - \alpha_1 n \qquad (2.2)$$

where α_1 (1/sec) is the first order loss coefficient.

The second order loss is also a depletion process but it is one which involves two ionic species, an electron and a positive ion or a positive and a negative ion. This type of loss is often called volume recombination and can be depicted mathematically as:

$$\frac{dn}{dt} = - \alpha_2 n^+ n^- \qquad (2.3)$$

where, α_2 = the second order loss coefficient

n^+ = the positive ion concentration

n^- = the negative ion concentration

If the positive and negative ion concentrations are assumed to be equal, then equation (2.3) becomes

$$\frac{dn}{dt} = - \alpha_2 n^2 \qquad (2.4)$$

As in the case of first order loss, the second order loss coefficient also represents the grouping of a number of individual second order loss processes, some of which will be discussed separately later.

The final form of the equation (2.1) thus takes on a more specific form involving first and second order loss components assuming 3rd order losses are negligible,

$$\frac{dn}{dt} = S - \alpha_1 n - \alpha_2 n^2 \qquad (2.5)$$

In the following section, summarized descriptions of various methods of nuclear generated plasma production are presented and mechanisms of their loss in a confined medium are discussed.

2.1.1. Plasma Generation Processes

A gas may be ionized in a number of ways. Some of the methods normally employed are thermal ionization by using electrical or RF heating, exposure to ionizing radiation, and collisional/coulomb interactions with other charged particles/electric field. Since the gas temperature of the current study is lower than that required for thermal ionization (typically between 2000 to 4000 K), the thermal ionization method is not considered to be a major contributing process.

Of the several nuclear methods that could be used for non-equilibrium charge production, the ones chosen for the study were

1. ^{60}Co gamma field ionization
2. fission fragment ionization, and
3. ionization of the chamber fill gas by the charged particles released during the ^{3}He(n,p)T reaction.

For the first option, γ-rays undergoing photoelectric and Compton scattering with the chamber walls and fill gas, release energetic electrons into the chamber fill gas, causing non-equilibrium ionization and excitation, which rapidly relaxes back toward a thermal equilibrium distribution.

Fission of ^{235}U produces a number of energetic particles. They can be characterized into light and heavy groups, a light group with atomic number ranging from 80 to 110 and a heavy group with mass numbers ranging from 125 to 155. The two fragments typically have energies of 98 MeV and 67 MeV for the light and heavy groups, respectively. This high kinetic energy provides the fragments with more than sufficient energy to ionize surrounding atoms through collisions. These fragments carry charges of approximately +20 to +22 [19]. This strong positive charge enables the fission fragment to ionize surrounding atoms through Coulomb interactions. The net result of these two characteristics (high energy, large positive charge) is that fission fragments produce dense concentrations of electron-ion pairs along their respective tracks through the gas.

A possible simulation of the plasma generated by fission fragments can be achieved using the plasma generated by the $^3He(n,p)T$ reaction. The protons and tritons produced by $^3He(n,p)T$ reactions have total energy of 0.76 MeV; the kinetic energies of the proton and triton are 0.51 MeV and 0.25 MeV, respectively. The fast ions lose energy by exciting and ionizing neutral atoms. The primary electrons produced by ionization of atoms have an average energy much higher than the ionization energy of the neutral atoms; hence, the electrons can also ionize the atoms. The cross section for electron impact ionization varies approximately linearly with excess energy just above the ionization threshold (24.5 eV).

The cross section is rather broad in energy, with the peak value occurring at around five times the threshold energy.

The possible major plasma generation and subsequent energy transfer reactions by fission fragments (or fast ions) in rare gases (which are part of the working media of this study) are listed as follows:

1. Ionization by fission fragment (or fast ions)
   $X + ff \rightarrow X^+ + e + ff$ (2.6)

2. Excitation by fission fragment (or fast ion)
   $X + ff \rightarrow X^* + ff$ (2.7)

3. Ionization by high energy electron
   $X + e \rightarrow X^+ + e + e$ (2.8)

4. Electron excitation
   $X + e \rightarrow X^* + e$ (2.9)

5. Superelastic collision (electron de-excitation)
   $X^* + e(\text{slow}) \rightarrow X + e(\text{fast})$ (2.10)

6. Associative ionization
   $X + X \leftrightarrow X_2^+ + e$ (2.11)

7. Metastable ionization
   $X^* + X^* \rightarrow X^+ + X + e$ (2.12)

8. Penning ionization
   $X^* + Y \rightarrow Y^+ + X + e$ (2.13)
   $X^* + X^* \rightarrow X_2^+ + e$ (2.14)

9. Charge transfer
   $X^+ + Y \rightarrow X + Y^+$ (2.15)

where the symbol f.f. indicates the fission fragment (or fast ions), and superscript (*) means that the specific atom (or molecule) is in an excited state. The symbols X and Y represent the noble working gas and other trace impurity gases, respectively.

2.1.2. Plasma Loss Processes

2.1.2.1. First order loss mechanism

The first order loss process may be classified as a diffusion loss for both electron and ions, and electron attachment to neutral particles for electron loss.

Diffusional loss. In this case, charged particles are lost by diffusion to the walls of the container. The diffusion process has three forms which are dependent on charged particle density: free, ambipolar and transition diffusion.

Free diffusion is the process in which electrons/ions migrate from a region of relatively high density to a region of low density. It happens when the charge density is so low that the Coulomb forces are ineffective.

Ambipolar diffusion is very similar to free diffusion in that charged particles are migrating from regions of high density to regions of low density. However, in this case, the ions are attempting to migrate through a dense plasma. An important characteristic of plasmas which is relevant is that they try to remain electrically neutral over their entire volume. Thus, as ions try to migrate, they try to form local areas of positive or negative charge. The resulting space charge will then retard the electron diffusion and increase the ion diffusion so that space charge neutrality is maintained at all points in space. Under these conditions, the electrons and ions will diffuse at the same rate as determined by the ambipolar diffusion coefficient. By the definition of the Debye length as being the distance over which substantial deviation from space charge neutrality is possible, the comparison of the diffusion length to the Debye length is an excellent manner in which to define the diffusion regime. During ambipolar diffusion, the Debye shielding length λ_D is much smaller than the characteristic diffusion length Λ.

There is gradual transition between free and ambipolar diffusion which is known as transition diffusion. In the middle of transition to ambipolar diffusion, the Debye shielding length λ_D and the characteristic diffusion length Λ become comparable. Gerber and Gerardo [20] performed detailed measurements of the decay of electrons and ions in a helium afterglow and concluded that the onset of transition diffusion occurs for ratios of the characteristic diffusion length to the Debye length as high as $\Lambda/\lambda_D = 86$.

Electron attachment. An important process for electron loss is electron attachment. In this process electrons are captured by electronegative atoms, or molecules, to form negative ions. To facilitate electron capture by a neutral atom or molecule, it is desirable that the total energy of the negative ion be lower than the energy of the neutral atom or molecule. This is related to the electron affinity, which is the difference in the ground state energies of the neutral atom and the negative atom. Larger electron affinities give rise to more stable negative ions.

Attachment is a collisional process and, like recombination, several different processes can occur which will result in the formation of a negative ion. The important attachment processes are [21]: radiative attachment, dissociative attachment and 3-body attachment.

1. Radiative capture

$$e + X \rightarrow X^- + h\nu \tag{2.15}$$

2. 3-body attachment

$$e + X + Y \rightarrow X^- + Y \tag{2.16}$$

3. Dissociative attachment

$$e + XY \rightarrow [XY]^{-*} \rightarrow X + Y^- \tag{2.17}$$

2.1.2.2. Second order loss process

Volume recombination. The second major electron/ion loss process is recombination. The totality of microscopic processes involved in the capture of electrons to form an excited atom or molecule and the subsequent decay to the ground state neutral is known as recombination. Recombination is essentially a volume process and acts to flatten any non-uniformities in the plasma density. The recombination process, being of a collisional microscopic nature, is considerably more complicated in its detail than diffusion. The probability that a recombination event will take place will depend upon the relative kinetic energies of the electron and the ion and, of more importance, how energy and momentum can be conserved in the recombination process. There are several different processes by which energy and momentum can be conserved and these give rise to different types of recombination. These processes are briefly outlined as follows, with more detailed analysis being available in references [21,22]:

1. Radiative recombination: this process is important only at low densities where other types of recombination are very week.
   $X^+ + e \rightarrow X^*(\text{or } X) + h\nu$ (2.18)
   $X^+ + Y^- \rightarrow XY + h\nu$ (2.19)

2. Electron collisional 3-body recombination: the probability of an electron-ion recombination is substantially increased if an electron is present to take away the excess energy.
   $X^+ + e + e \rightarrow X + e$ (2.20)
   $X_2^+ + e + e \rightarrow X + X + e$ (2.21)

3. Neutral collisional 3-body recombination: even though neutral atom or molecules are less efficient in removing excess energy than the electrons, they play role in high pressure ionized media (multi-atmospheres).
   $X_2^+ + e + Y \rightarrow X + X + Y$ (2.22)
   $X^+ + X + X \rightarrow X_2^+ + X$ (2.23)

4. Dissociative recombination: this is an important process for rare gas (except helium) discharge because of its high efficiency and large recombination coefficient.
   $X_2^+ + e \leftrightarrow (X_2)^* \rightarrow X^* + X$ (2.24)
   $XY^+ + e \leftrightarrow (XY)^* \rightarrow X + Y^*$ (2.25)

Columnar recombination. Columnar recombination is the last second order loss mechanism to be discussed. It is actually a combination of all high ion density recombination reaction mechanisms. The reason it is discussed separately is due to its nature of formation. Unlike uniform method of ionization such as thermal heating or exposure to gamma rays, when a gas is exposed to highly energetic and heavy charged particles like fission fragments, dense regions of ionization form along the particle's track. These ionization columns will exhibit recombination characteristics of a gas with a much higher density until the newly formed inhomogeneous electrons and ions diffuse to form a uniform concentration throughout the gas volume. The rapid recombination along the fission fragment's track is the reason for classifying columnar recombination as a separate form of loss. Wilhelm [23] developed a columnar recombinational theory based on the dynamics of the individual ionization columns and showed that the effective columnar recombination coefficient is considerably larger than the volume recombination coefficient for the time until the diffusion of column ionization is complete. Thus a special property of the columnar recombination coefficient is its explicit time dependence caused by the internal dynamics of the ionization columns. It is also predicted that columnar recombination is a considerably faster process than ordinary volume recombination.

Temperature dependence of recombination. Recombination is very sensitive to electron temperature with rather sharp decreases in recombination coefficients α as electron temperature increases. The theoretical form of the electron temperature dependence of the recombination coefficient depends on the process under consideration. It is not always possible to provide a general formular for the electron temperature dependence for recombination, however, as a first approximation:

1. for radiative recombination [23]
   $\alpha \sim T_e^{-0.7}$ (2.26)
2. for dissociative recombination [23]
   $\alpha \sim T_e^{-0.5}$ (2.27)
3. for collisional-radiative recombination [24]
   $\alpha \sim T_e^{-4.5}$ (2.28)

In the following chapter, the development of a nuclear-generated plasma diagnostic system based on the PIC technique and its application is presented in detail, including a review of the PIC system's basic operational characteristics. The experimental research was aimed at studying the rates of electron production and loss due to diffusion and recombination occurring as a result of interaction of neutron and gamma radiation fields with selected series of gas compositions. Throughout the experimental work validation of the PIC technique and demonstration of its capability for measurement of the various parameters of interest was undertaken.

CHAPTER 3
DEVELOPMENT OF AN IMPROVED PULSED IONIZATION CHAMBER (PIC) SYSTEM AND ITS APPLICATION TO NUCLEAR-GENERATED PLASMA DIAGNOSTICS

3.1. Pulsed Ionization Chamber (PIC) System

The PIC technique, originally developed and investigated by Ellis and his students at the University of Florida, had been successfully used in the 1960's and 1970's in the study of nuclear-generated plasmas and diagnostics [10,16]. As discussed in the introductory chapter, the PIC system should be capable of providing useful information on the generation and loss of plasmas, especially those produced in high pressure gases by nuclear radiation, in good simulation of the gas core reactor environment. In the current chapter, detailed descriptions of the development of a new PIC system are provided. Descriptions of some of the experiments performed for the study of the characteristics of nuclear-generated plasmas with the system are also presented.

The experiments undertaken with the improved PIC system and technique can be described briefly in the following manner: An ionization chamber filled with either a He(UF_6) fissionable gas or a ^{3}He gas mixture serving as the working fluid, is exposed to a volumetric neutron source (UFTR). Fission fragments or fast ions generated volumetrically under neutron bombardment would produce nonequilibrium ionization and excitation of the background noble gas. Then, measurements were performed on the plasmas produced, to obtain values for the experimental plasma parameters, and to determine whether a sufficiently high electrical conductivity can be attained to be useful as an input to an MHD converter. The ^{60}Co γ-ray source was also utilized to study the loss characteristics of plasma generated by uniform ionization versus nonequilibrium ionization by fission fragments (or fast ions). The experimental work has been focused mainly on the study of $He(UF_6)$ plasma with varying degree of UF_6 gas composition, which was undertaken prior to, in conjunction with and subsequent to work reported by Ellis and Baumgartner [12]. In addition, the experiments were performed for other gas mixtures including N_2 and high purity buffer gases such as He, Ar and Xe to study plasma kinetics of the candidate buffer gases. Fission chambers filled with He and Ar have been used for the study of buffer gas plasmas characteristics for those generated by fission fragment. These measurements were also aimed at verifying earlier reports [10,23] on the enhanced columnar recombination loss of the plasmas which were generated by heavy charged particles such as fission fragments.

3.1.1. Operational Principles of PIC Technique

The PIC technique involves the periodic application of a single polarity collection potential across the electrodes of an ionization chamber. Sufficient time is allowed between high voltage pulses for the ionization density in the gas filled gap to approach its asymptotic steady state limit. The application of the collection voltage results in the collection of electrons and ions of the equilibrium ionization density. The PIC technique principally utilized the steady state (equilibrium) mode of plasma diagnostics because of the constant field intensity characteristics of the γ-source and the neutron flux of nuclear reactor.

A schematic diagram illustrating the operational principles of the PIC technique is shown in some detail in Figure 3.1. The electronics used with the PIC system are capable of operating in one of two modes; a conventional ionization chamber current mode and the pulsed ionization chamber (PIC) mode. The high voltage (V_o, S-1) is pulsed at a repetition rate (~ 1 Hz) which allows the ionization density to grow to its asymptotic limit N_S between pulses. The chamber output impedance (S-2) is dropped momentarily (for $\leq$ 100 nsec, which is equivalent to the HV pulse rise time) to coincide with application of the high voltage pulse allowing rapid charging of the system capacitance, and then is raised for observation of the PIC output voltage signal $v(t_c)$, which

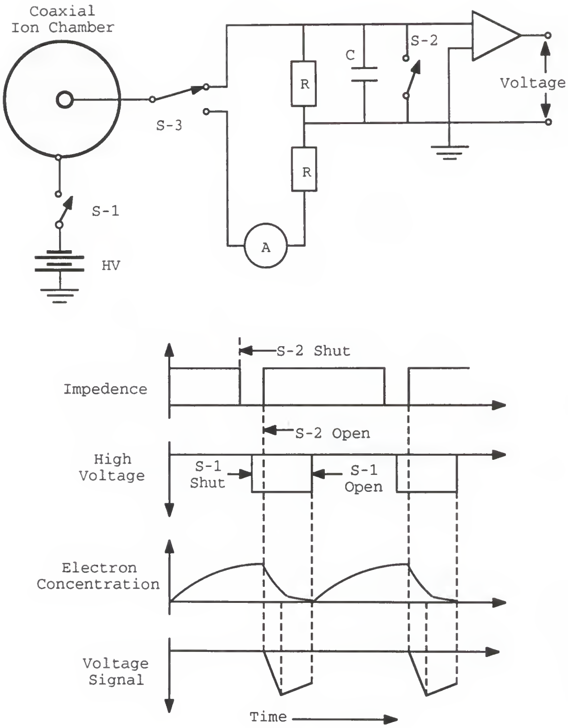

Figure 3.1: Operation of System Electronics (PIC mode)

is proportional to N_S, and can be used for its determination as described below.

The steady state equilibrium ionization density, N_S, for an ion chamber having cylindrical coaxial electrode geometry, and operated in the pulsed ion chamber mode has been shown [16] to be related to the output voltage signal $v(t_c)$, at the time of electron collection t_c, in the following manner (without space charge effect),

$$v(t_c) = -\left[\frac{N_s eU}{C}\right]\left[1 - \frac{1}{2\ln(b/a)}\right] \qquad (3.1)$$

$$\text{or} \quad N_s = -\frac{v(t_c)C}{eU\left[1 - \frac{1}{2\ln(b/a)}\right]} \qquad (3.2)$$

where C is the anode circuit load capacitance, (b/a) is the ratio of the cathode to anode radii, and U is the effective volume of the ionization chamber.

The source term (ionization rate) S is obtained from saturation ion current I_S measurements by applying a constant bias voltage across the chamber (S-1 shut, S-3 connected to picoammeter) where

$$S = \frac{I_S}{eU} \qquad (3.3)$$

Since the pulsed mode of operation involves pulsing the collection potential at a rate which allows sufficient time between pulses to permit the ionization density within the sensitive volume of the chamber to grow to its asymptotic steady state limiting value N_s, the general kinetic equation

$$\frac{dn}{dt} = S - \sum_{i=1}^{\infty} \alpha_i (N_s)^i = 0 \text{ (steady state)} \qquad (3.4)$$

under steady state conditions, reduces to an expression for the source dependence on the ionization density N_s,

$$S = \alpha_1 N_s + \alpha_2 N_s^{\,2} + \alpha_3 N_s^{\,3} + \cdots\cdots \qquad (3.5)$$

For regions of the ionization density, where one particular order of loss predominates, simple first and second order expressions for the source dependence of ionization can be written, i.e.,

$$N_s = \frac{S}{\alpha_1} \qquad \text{for } \frac{\alpha_1}{N_s} >> \alpha_2 \qquad (3.6)$$

$$N_s = \sqrt{\frac{S}{\alpha_2}} \qquad \text{for } \alpha_2 >> \frac{\alpha_1}{N} \text{ or } \alpha_3 N_s \qquad (3.7)$$

And for $\frac{\alpha_1}{N_s} >> \alpha_2 >> \alpha_3 N_s$, the combined first and second order effects are given by the expression

$$N_s(S) = \frac{1}{2\alpha_2} [\sqrt{\alpha_1^{\,2} + 4\alpha_2 S} - \alpha_1] \qquad (3.8)$$

Thus by determining the values for S and N, one can calculate the loss coefficients for the gas under study. Additionally, since observed electron/ion collection times (t_c) are related to electron/ion mobilities (μ) by the expression

$$\mu = \frac{(b^2 - a^2)\ln(b/a)}{2V_o t_c}, \qquad (3.9)$$

one can calculate the electrical conductivity of a plasma by using the relationship

$$\sigma = Ne\mu \tag{3.10}$$

where N and μ are given in equation (3.2) and (3.9), respectively.

3.1.2. Development of a New PIC System

The most recent time when the PIC system was improved occurred more than 10 years ago and was implemented by Kaiser [17]. Also, the system he developed was built mainly for use with wide-range reactor flux measurement systems. It was based on the technology of that date, using analog circuitry and an early desktop computer and was designed and used for the pulsed ion measurement mode. When the current plasma diagnostic research was initiated, the Kaiser-era PIC system was modified for electron collection by changing the polarity of the high voltage pulse and was utilized for nuclear generated plasma diagnostics. Subsequently, when it was found that the circuits were not sufficiently stable to allow accurate measurements, and also were limited with respect to the maximum operational high voltage, partly because of aging problems of the circuit components, it was decided to develop a new PIC system based on digital components and systems using available state-of-the-art electronic components.

The resulting PIC experimental system designed and constructed for use in the early stages of the study consisted of: (1) PIC electronics and associated instruments (2) an experimental assembly which included an ion chamber filled with a specific gas (or mixture) under study, and a heater system for use with temperature dependence studies (3) a gas purge system utilized for safety purposes for experiment where UF_6 gas was involved. A block diagram of the PIC system is shown in Figure 3.2 and a detailed description of each components is presented below.

System electronics. The PIC system has been upgraded several times as the technology of electronic devices has advanced [16,17]. The most important and challenging part of the PIC system is the high voltage pulser. It requires an extremely fast rising time (to minimize charge loss during pulse rise), low ripple and ringing of the pulse (to maintain a constant E-field across the chamber electrode gap), high voltage (to be versatile to accommodate various possible geometries of the ion chambers) and long pulse width sufficient to sweep the charges free from the chamber electrode gap. In addition, it requires long term stability of pulse repetitions. The earlier version of the PIC system was based on transistor switching techniques [17]. The more recently developed PIC system, alluded to above, is based on state-of-the-art semiconductor technology which enabled the construction of a high voltage pulser which met all the requirements presented above.

The PIC system electronics consist of three main parts: (1) the pulse generator, (2) the high voltage pulser, and (3) the signal detector. The circuit diagrams of the system are shown in Figures 3.3 and 3.4. The pulse generator provides

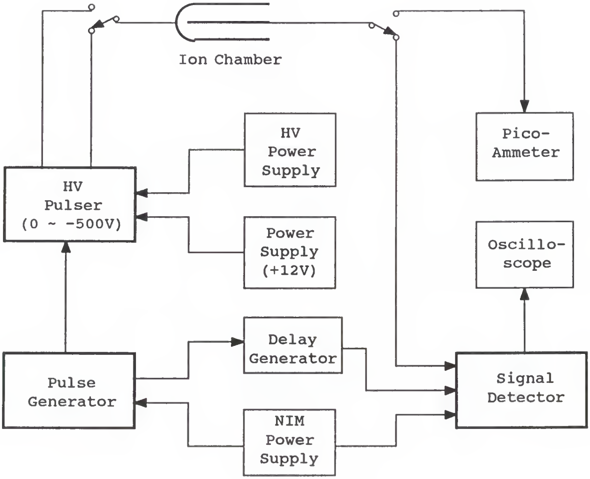

Figure 3.2: Block Diagram of the PIC System

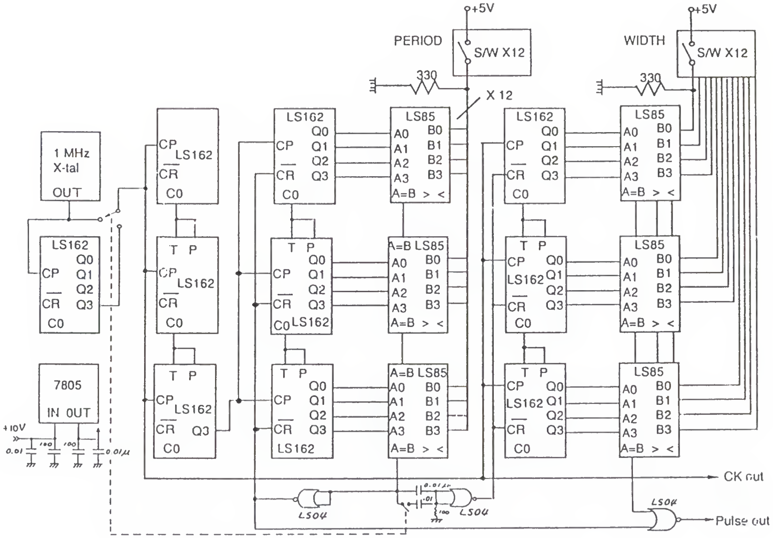

Figure 3.3 : Electronic Circuit Diagram for the PIC System
(Pulse Generator and Timing Circuit)

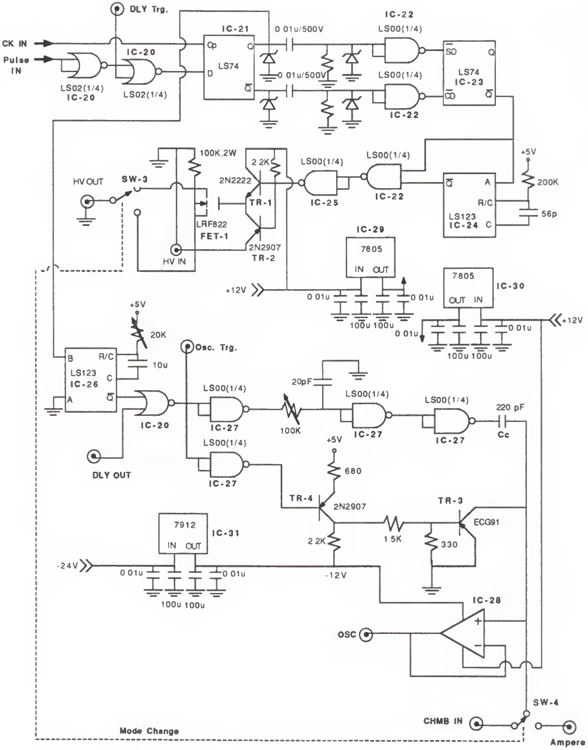

Figure 3.4: Electronic Circuit Diagram for the PIC system (HV Pulser and HI Switching Circuit)

TTL pulses whose period and width are controlled by two thumbwheel switches mounted on the front panel of the instrument with ranges from 1 msec to 10 sec and 1 μsec to 10 msec, respectively. The high voltage pulser converts the TTL level pulses, which are derived from the pulse generator, into high voltage pulses by using a high speed MOSFET (Metal-Oxide-Semiconductor Field-Effect Transistor) operated as a switching device. With this version of the high voltage pulser, rise times as fast as 30 nsec have been obtained under capacitive loading of approximately 400 pF for high voltage pulses of up to 500 volts. The signal detector consisted mainly of an impedance switching circuit, capacitance compensation circuit, and a buffer amplifier. The heart of the signal detector is the impedance switching system. The use of a fast PNP-type bipolar transistor with an f_t of 150 MHz has allowed the fast switching speed requirement of this circuit to be met with a rise time of approximately 50 nsec. A special technique has been used to compensate the effect of the switching transistor capacitance so as to linearize the base line of the signal. A FET input operational amplifier, which has an extremely high input impedance of 10^{14} Ω, has been used to provide a signal for the oscilloscope without disturbing the measurement system. Figure 3.5 shows a photograph of the circuits. A more detailed explanation of the circuits and their performance characteristics is presented in Appendix A.

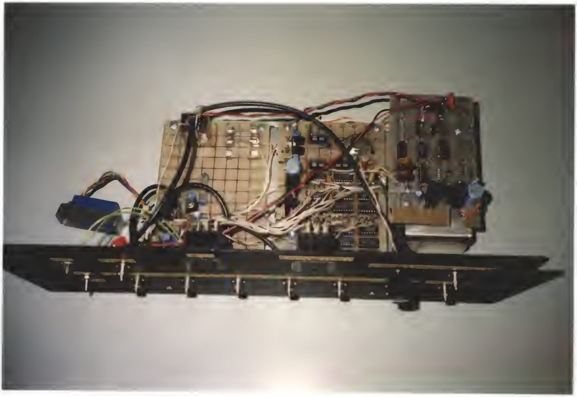

Figure 3.5: A Photograph of the PIC System Circuitry

Ionization chambers. The ionization chambers used in the early rare gas plasma kinetics phase of the study were obtained from commercial sources and their original gas filling had been retained. Specifications for the ionization chambers used in this study are listed in Table 3.1. The ionization chambers used for the $He(UF_6)$ measurements were originally filled with BF_3 or He(F) and were manufactured by LND Inc [25]. The chambers were manufactured under customer specifications. They were rated to a maximum temperature of 450 °C and a maximum pressure of 20 atmospheres. Prior to

Table 3.1: Specifications of the Ion Chambers Used in the PIC Plasma Diagnostic System

Gas	Chamber Pressure (atm)	Anode Radius, a (cm)	Cathode Radius, b (cm)	Chamber Length, *l* (cm)
He(%UF_6)	~1	0.00254	0.7696	8.585
^{3}He (2% CO_2)	1 6 10	0.00254	1.22	10.2
Ar(5% N_2) Fission Chamber	1	0.88	1.20	10.2
Xe	10	0.00254	4.842	14
^{4}He filled Fission Chamber	1 10	0.00254	1.2	12.7

being filled with BF_3, they were fluorine passivated up to their rated temperature. Each chamber contained a valved fill tube, a signal connection and a guard ring connection. High voltage was applied to the chamber outer case. The chamber material was type 304 stainless steel and their dimensions and configuration are shown in Figure 3.6. To study the effect of UF_6 concentration on plasma production and loss, the ion chambers were filled with four He(UF_6) gas compositions. The total pressure for each chamber was ~1 atm, while the mole percentages of UF_6 were 0.1, 1.0, 3.9 and 7.5, respectively. Further information on the UF_6 gas filling facility and procedure is described in the work, which was undertaken in conjunction with the author, reported by Ellis and Baumgartner [12].

Heater system. A chamber heater system was designed and constructed that was large enough to hold a range of chamber sizes including that of the UF_6 chambers but, at the same time, small enough to fit into either the ^{60}Co γ-ray irradiator or the thermal column of the UFTR. Figure 3.7 shows the heater system which met the above requirements. It consisted of a commercial cylindrical heater coil assembly (Thermcraft model) embedded in alumina thermal insulation (Zircar Products model ZAL-45). The heater was rated to 1447 K, while the rating of its alumina insulation was rated up to 1773 K. The insulation was enclosed with 1/8" thick type TL

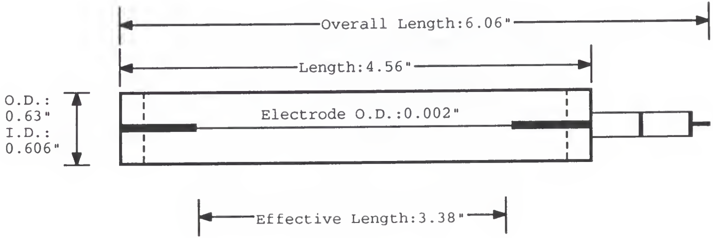

Figure 3.6: Dimension of Ion Chamber filled with He(UF6)

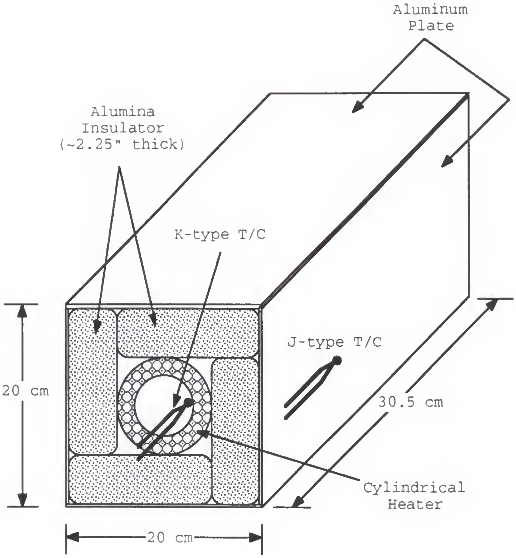

Figure 3.7: Heater Assembly

6061 aluminum plating. Also included in the heater assembly were K- and J-type thermocouples; the K-type for measuring the ion chamber temperature and the other for monitoring temperature of the aluminum plating.

Gas purge system. Operation and use of the experimental assembly within the UFTR required prior approval of the Reactor Safety Review Subcommittee. One of the requirements necessary for approval, when the measurement involved He(UF_6) gas mixtures, was that there must be a means by which a UF_6 leak could be detected and the effluent subsequently scrubbed without contaminating the UFTR graphite moderator or entering the core vent system. The gas purge system which satisfied both of these requirements is shown in Figure 3.8. The main component of this system is a type 304 stainless steel cylinder called the chamber housing in which the ion chamber was enclosed. The chamber housing, shown in Figure 3.9, had alumina spacers in its interior to hold the ion chamber and its thermocouple in place. It also had a feedthrough in a cap which was bolted over the single open end of the chamber so that the ion chamber connections could still be made with the chamber enclosed in a pressure-tight enclosure. Inlet and outlet supply lines allowed a nitrogen purge to be continuously circulated through the chamber housing while the heater system was in operation. The rest of the gas purge system consisted of a nitrogen gas supply, the chamber housing, a fluorine detector, a two liter bottle of 5 M NaOH solution, a two liter bottle of 2 M NaI solution,

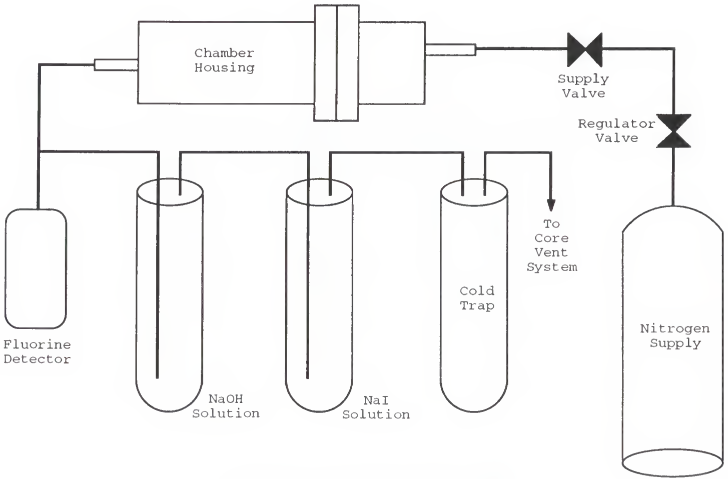

Figure 3.8: Gas Purge System

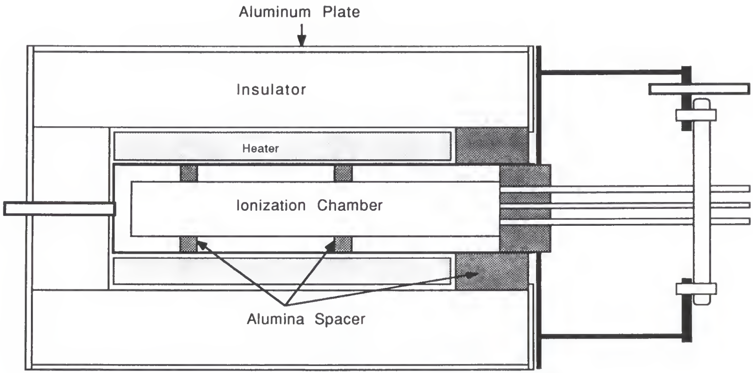

Figure 3.9: Ionization Chamber Housing and Heater Assembly

and a liquid nitrogen cooled cold trap. The nitrogen bottle supplied the system with 1~2 ml/sec nitrogen purge at a pressure of 2.5 psig. The nitrogen flowed into the chamber housing, around the installed ion chamber, and exited out the back of the housing. It then flowed through 0.25" polyethylene tubing and past the pump-style halogen detector (TIF model 5500). The detector took suction on the return line and passed the sample through a small ion chamber. Any change in the gas conductivity would cause the detector to respond. It was sensitive to halogen concentrations of 3 ppm and greater. Next, the nitrogen gas bubbled through the 5 M NaOH solution. This solution removed the uranium from the gas purge (if any were present) by the following reaction:

$$UF_6 + 4\ OH^- \rightarrow UO_2^{++} + 6F^- + 2H_2O \qquad (3.10)$$

$$2UO_2^{++} + 6\ OH^- + 2Na^+ \rightarrow Na_2U_2O_7 + 3H_2O \qquad (3.11)$$

The gas was then bubbled through a 2 M NaI solution to remove any fluorine that might be released in the above reactions. Finally the gas was sent through a liquid nitrogen cooled cold trap to remove any impurities or entrap liquid which had passed through the solutions. After passing through the cold trap, the expanded nitrogen gas was exhausted to the atmosphere through the reactor core vent system. The requirement for the utilization of this system applied only for experiments which involved placing the experimental assembly, in which He(UF_6) gas filled ion chamber was included, inside the UFTR thermal column.

Radiation source. The ^{60}Co irradiator which was used to provide γ-ray flux was located in the Nuclear Science Center of the University of Florida and had activity of approximately 50 Curies. The source γ-rays of 1.17 MeV and 1.33 MeV ionized the gas mixtures with primary interaction in this energy range being Compton scattering. The University of Florida Training and Research Reactor (UFTR) was used to produce both a neutron and γ-ray flux to ionize gas mixtures. The experimental assembly was placed into the thermal column of the UFTR in place of the graphite stringers to locate the ion chambers as close as possible to the reactor core. This resulted in positioning the chamber approximately 8" from the fuel box wall with the distance being filled by reactor grade graphite. The resultant thermal neutron flux at the ion chamber was approximately 7×10^6 (neutrons/cm^2-sec-watt) with a fast neutron flux of 1×10^5 (neutrons/cm^2-sec-watt) [26].

3.2. PIC Plasma Diagnostic Experiments

3.2.1. Experimental Method

An ionization chamber filled with a specific gas or gas mixture under study was exposed to either a neutron source (UFTR) or γ-ray flux to generate a plasma inside the chamber. Prior to making measurements, the experimental system was checked for proper operation. This involved testing the mechanical as well as electronic portions of the experimental assembly. When the experiment used an ionization chamber filled with a He(UF_6) fissionable gas in the UFTR, the gas purge line and chamber housing were checked and pressure tested before the experimental assembly was inserted into the thermal column of the UFTR (the other gases used in the study did not require the use of a pressure tight chamber housing). After the experimental assembly was inserted into the thermal column of the UFTR, using the shut-down γ-ray background in the reactor core, the system's electrical continuity was checked by setting the system to the steady state current measurement mode and using the picoammeter to observe an appropriate γ-ray induced saturation current. The capacitance of the system was also measured at this time. For the test of the PIC mode operation, the PIC signal base line was calibrated at zero reactor power, After this, the reactor was brought up and set at medium power level (100W ~ 1KW) to observe characteristic PIC voltage signal which provides information on the electron and ion collection time. When the ^{60}Co γ-source was being used as the ionization source, a procedure similar to that used with the UFTR was followed. However, in this case, the PIC signal base line was calibrated when the source was positioned in the storage position. Measurements have been carried out for a range of gas temperatures, pressures and compositions, as well as nuclear ionization sources. Nuclear generated plasmas have been studied with both γ-ray and neutron fields. The ^{3}He(n,p)t and ^{235}U(n,f)FF charged particle producing reaction source and γ-rays have been used with helium gases, while fission fragments and γ-ray field ionization have been used for the Ar filled chamber. Only the γ-ray ionization source has been utilized in the diagnostic experiments with Xe gas.

3.2.2. Data Acquisition and Analysis

Data acquisition. The evaluation of the ionization rate, steady state ion density, first and second order loss coefficients involves the measurement of two parameters. These were saturation current (I_s) and PIC peak voltage (V_{pic}). In addition, to help in characterizing the type of loss process involved, a third parameter, the signal collection time (t_c), was obtained. Data was acquired by performing a series of measurements at a given temperature. For example, if the ^{60}Co γ-source was being used as the ionization source, the source was positioned at a given distance from the ion chamber to produce a certain ionization rate. The temperature of the heater was stabilized at the desired level and then, with the source in the same position, both the saturation current (ion chamber current measurement mode) and voltage signal (PIC mode) were obtained. Upon completion of this step, the source was repositioned and another two measurements (I_s and V_{pic}) were obtained for the same temperature. This process was continued until the source had traversed its full range of travel or, if the UFTR was used as the ionization source, until the reactor power had reached its maximum allowed level (100 KW). After I_s-V_{pic} measurement had been obtained for the full source/reactor power range of either the ^{60}Co γ-source or the UFTR, the temperature would be raised to a new value and the entire sequence would be repeated. The complete process was continued until the temperature had reached the ion chamber's maximum rating or the leakage current exceeded tolerable noise level, whichever came first.

Data analysis. The steady state ionization current (I_s) and the PIC peak voltage (V_{pic}) were used to find the ionization source rate (S) and steady state plasma density (N_s) using the corresponding equations (3.3) and (3.2), respectively. In order to solve for the first and second order loss coefficients, a graphical analysis was performed using the ionization source rate and the steady state plasma density measured for various ^{60}Co γ-source positions or reactor power levels. Both the ionization source rate (or steady state ionization current) and the steady state plasma density (or PIC peak voltage) were plotted on the log-log graph as shown in Figure 3.10. If the ionization source rate was proportional to the plasma density (as the slope of the fitted line in this graph depicts, slope = 1), it implies that the second and higher order losses were negligible and that the first order loss mechanisms predominate, i.e.,:

$$S = \alpha_1 N_s \quad (\text{or } \log(N_s) = \log(S) - \log(\alpha_1)) \qquad (3.10)$$

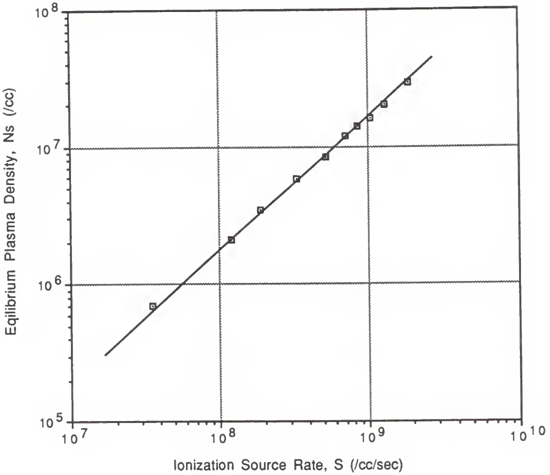

Figure 3.10: PIC Plasma Diagnostic Plot at 573 K using the 50 Ci Co-60 Source, 1 atm He(1.0% UF6)

Thus, the first order loss coefficient could be solved for by use of the relation:

$$\alpha_1 = S/N_s \tag{3.11}$$

The values for the ratio S/N_s were then plotted as a function of N_s as shown in Figure 3.11 and a first order loss coefficient α_1 was determined for that particular gas component and temperature by extrapolation to the origin. A series of such determinations were made to find the temperature dependence of the first order loss coefficients. When diffusional processes were dominant, equation (3.10) for first order loss could be expressed as:

$$S = \alpha_1 N_s = -D\nabla^2 N_s = (D/\Lambda^2)N_s \tag{3.12}$$

where Λ is the characteristic diffusion length for a cylindrical chamber of radius r and length L and is given as,

$$1/\Lambda^2 = (\pi/L)^2 + (2.405/r)^2 \tag{3.13}$$

Since Λ is determined directly from the ion chamber geometry, values for α_1 could be used to calculate the diffusion coefficient, D.

A similar graphical analysis was followed for the determination of the second order loss coefficient. When the $\log(N_s)$-$\log(S)$ plot shows that the ionization rate is proportional to the square root of the plasma density (as shown in Figure 3.12), it implies that the first order loss is negligible and that:

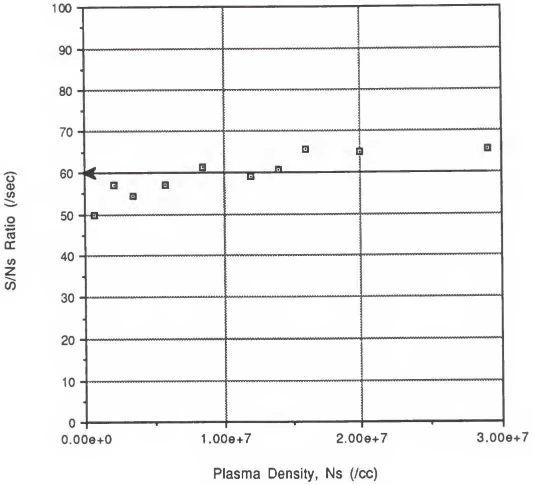

Figure 3.11: 1st Order Loss Coefficient Plot at 573 K using the Co-60 Source, 1 atm He(1.0% UF6)

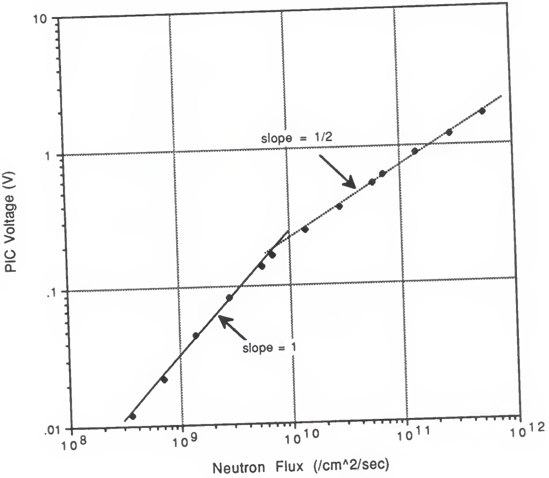

Figure 3.12: PIC Plasma Diagnostic Plot at 453 K using UFTR, 1 atm He(3.9% UF6)

$$S = \alpha_2 N_s^2 \quad (\text{or } \log(N_s) = \tfrac{1}{2}\log(S) - \tfrac{1}{2}\log(\alpha_2)) \qquad (3.14)$$

Thus, the second order loss coefficient could be solved by the equation:

$$\alpha_2 = \frac{S}{N_s^2} \qquad (3.15)$$

As with α_1, the ratio S/N_s^2 was plotted as a function of ionization density N_s (as shown in Figure 3.13) and its asymptotic limit obtained as the limiting value of the second order loss coefficient α_2 for that particular temperature and gas composition. A series of these analyses were also plotted for varying temperatures (Figure 3.14) and fitted to examine the variation of the second order loss coefficient with temperatures. For example, the particular set of data measured with 1 atm He(3.9% UF_6), as shown in Figure 3.14, was fitted to the power of temperature and the resultant curve was represented as:

$$\alpha_2 = 4.5961\text{x}10^4 \ (T)^{-4.0528} \qquad (3.16)$$

The fitted curve enabled the extrapolation to α_2 values at higher temperatures where experimental measurements, from a practical stand point, could not be conducted.

The final experimental parameter determined in this study, for which values were obtained by means of PIC mode operation, was the signal collection time, t_c. This parameter represents the time required for the electrons and ions inside the ionization chamber to cross the electrode gap, under the influence of local electric field due to an

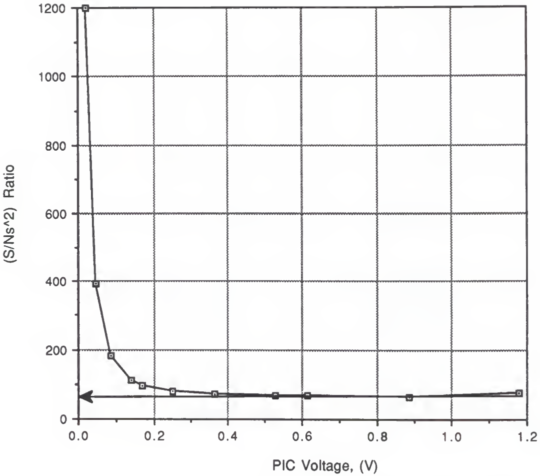

Figure 3.13: 2nd Order Loss Coefficient Analysis Plot using UFTR, 1 atm He(3.9% UF6)

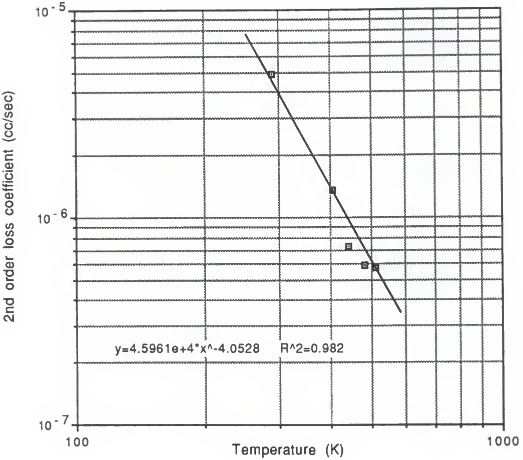

Figure 3.14: T-Dependency of 2nd Order Loss Coefficient for 1 atm He (3.9% UF6) using the UFTR

externally applied potential. The collection time was measured using an oscilloscope trace and was equivalent to the PIC voltage signal pulse rise time. Typical PIC voltage signals are shown in Figure 3.15. These signal profiles, obtained with a 10 atm Xe filled ionization chamber, show an electron collection time of ~3 μsec in Fig.3.15(a) and an ion collection time of ~1.2 msec in Fig.3.15(b) for a chamber bias of -400V. For cylindrical coaxial electrodes, the collection time is expressed analytically as:

$$t_c = \frac{(b^2 - a^2)\ln(b/a)}{2V_o\mu} \qquad (3.16)$$

allowing the mobility μ of charge carriers to be calculated as:

$$\mu = \frac{(b^2 - a^2)\ln(b/a)}{2V_o t_c} \qquad (3.9)$$

The electron/ion density and mobility data, thus obtained, were used to evaluate the electrical conductivity of the gas by using the relationship:

$$\sigma = \sigma_e + \sigma_i = N_e e\mu_e + N_i e\mu_i \qquad (3.17)$$

where σ_e and σ_i represent electronic and ionic conductivity, respectively. The results were plotted as a functions of the neutron flux, as shown in Figure 3.16. In the absence of electron attachment, where negative ions are formed, the electrical conductivity would be due mainly to electrons, since the electron mobility is at least two orders higher than that of ions [27].

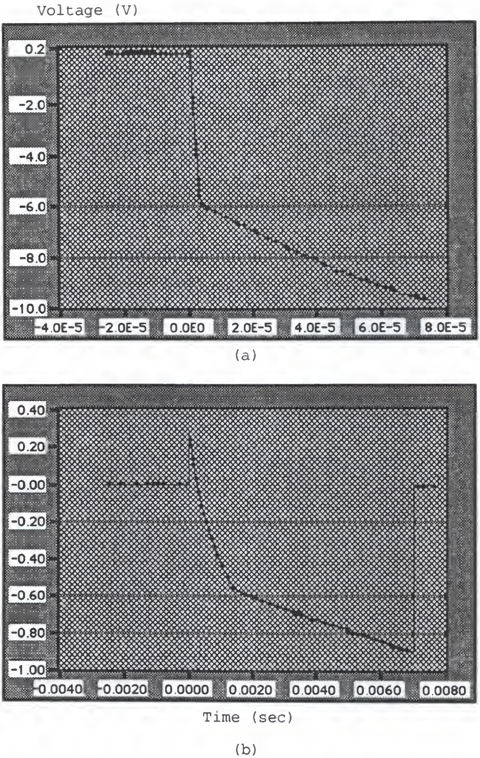

Figure 3.15 : Typical PIC Voltage Signal;
(a) Electron, (b) Ion Collection

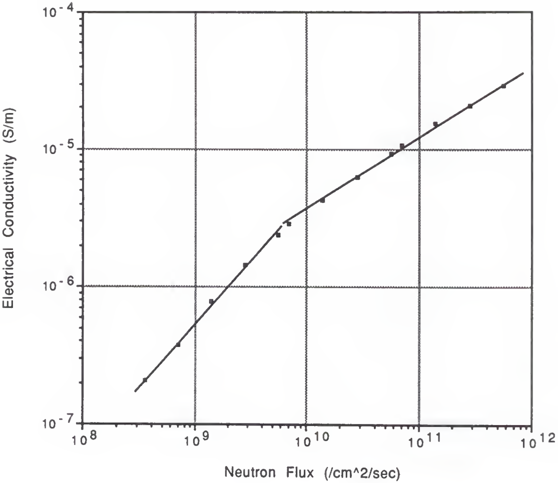

Figure 3.16: Electrical Conductivity Calculated by PIC Measurement at 453 K using UFTR, 1 atm He(3.9% UF6)

Since the diffusion of charged particles is related to their mobilities, the Einstein's relationship [28] allows one to calculate the temperature of the charged particles using known values for the diffusion coefficient and mobility;

$$\frac{D}{\mu} = \frac{kT}{e} \tag{3.18}$$

where D is the diffusion coefficient, k is Planck's constant and T is the absolute temperature of the gas. In addition, if the gas temperature is known, the diffusion coefficient can be calculated using the mobility data.

3.3. Experimental Results and Discussion

In addition to the basic studies of the fuel gas He(UF_6) type mixtures, plasma diagnostic experiments were also performed for other gas systems including high purity buffer gases such as He, Ar and Xe, and their mixtures with molecular species such as N_2. Measurements have been carried out for a range of gas temperatures, pressures and compositions, as well as nuclear ionization sources. Typical of the results obtained for the PIC plasma diagnostic experiments performed with rare buffer gases of He, Ar and Xe using the ^{60}Co source are those shown in Figure 3.17. This figure shows a great contrast in plasma production and loss characteristics as the PIC plasma diagnostic signal voltages range over almost 3.5 decades, from 1 mV to up to approximately 30 V. The upper curve is for gamma ionization of a 10 atm Xe filled chamber having the dimension shown in

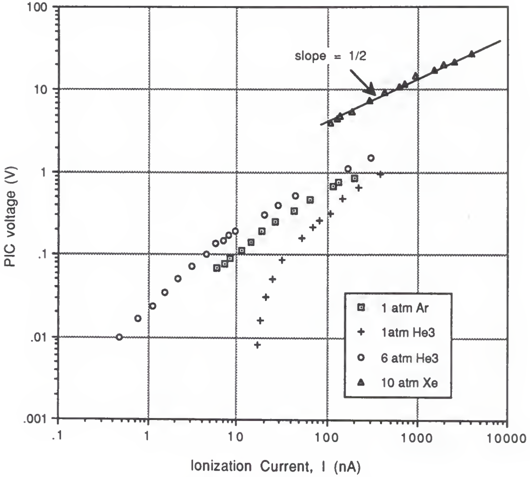

Figure 3.17: PIC Plasma Diagnostic Plot at Room Temperature using Co-60 Source, Rare Gases (He, Ar, Xe)

Table 3.1. The combination of high gas pressure and large chamber electrode gap greatly reduces diffusional first order loss, thereby, allowing the second order loss processes to predominate.

3.3.1. Plasma Source Production Rate

Theory predicts that the plasma production rate should be directly proportional to the neutron flux, whereas the ionization density should be a function of gas composition and system kinetics, as well as the gas temperature and pressure. The results of PIC plasma diagnostic measurements performed with $He(UF_6)$ gas mixtures, which are plotted and shown in Figures 3.18 through 3.21 demonstrate this to be true. Data for $He(UF_6)$ compositions of 0.1, 1.0 and 3.9 mole percent UF_6 were taken by Ellis and Baumgartner [12] with the participation of the author and use of the new PIC system. Some of the measurements were repeated by the author and measurements were extended to include 7.5 mole percent UF_6. In these figures it can be seen that with increasing gas temperature there is also an increase in the plasma generation rate. This may be due to the decrease of mean free path of neutron in the gas as it was pressurized. However, as the temperature increased, a leakage current effect was also observed to increase. This was especially true for the low neutron flux ranges where the leakage current was comparable to the steady state ionization

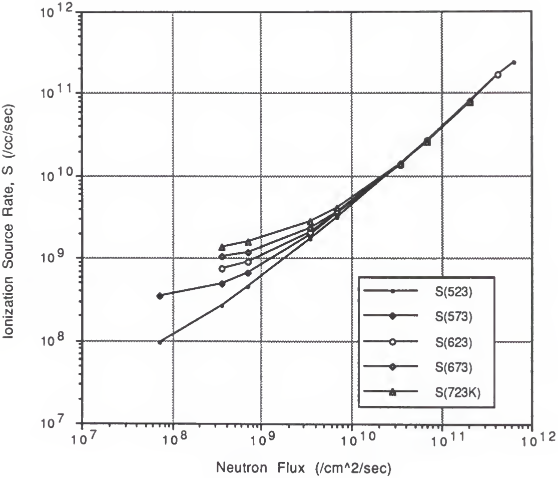

Figure 3.18: Ionization Source Rate Measured by using the UFTR, 1 atm He(0.1% UF6)

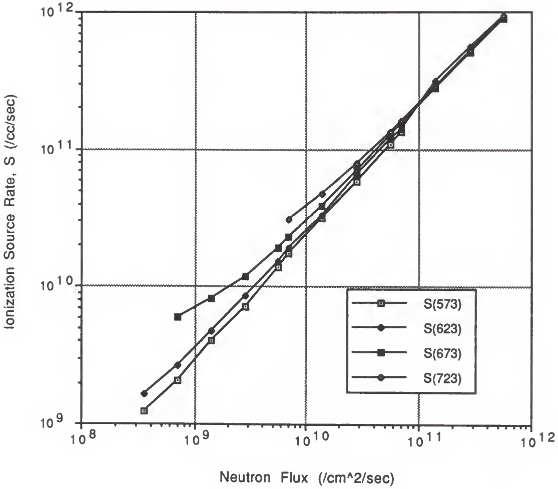

Figure 3.19: Ionization Source Rate Measured by Using the UFTR, 1 atm He(1% UF6)

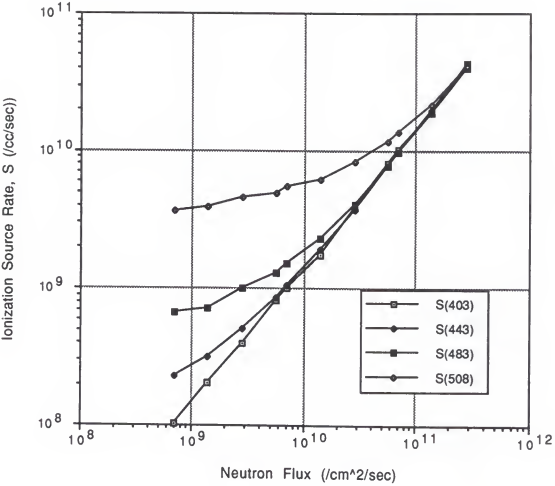

Figure 3.20: Ionization Source Rate Measured by Using UFTR, 1 atm He(3.9% UF6)

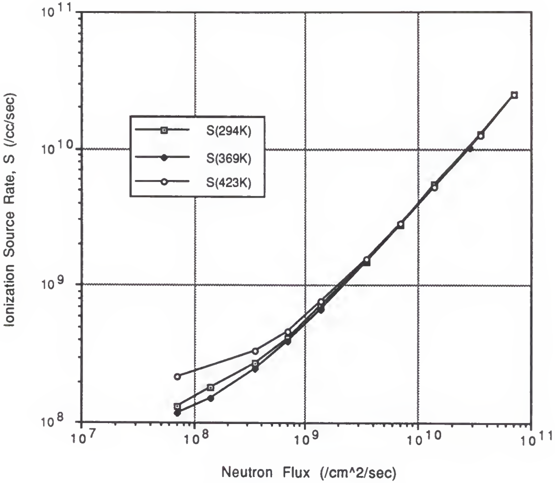

Figure 3.21: Ionization Source Rate Measure by using UFTR, 1 atm He(7.5% UF6)

current. This particular leakage current problem was the main factor that limited the temperature measurement range (to 730 K) for the PIC technique. The ionization source rates measured range from ~1x10^{8} (/cm^{3}-sec) to ~1x10^{12} (/cm^{3}-sec) as the neutron flux varied from 5x10^{7} (/cm^{2}-sec) to 5 x 10^{11} (/cm^{2}-sec). The maximum source generation rate at a given temperature was observed at the He(1% UF_6) composition.

3.3.2. Plasma Loss Coefficient

First order loss. For the He(UF_6) gas mixtures, as discussed in the previous section and as expected, the major electron loss mechanism appeared to be due to electron attachment to the electronegative species present or generated in the He(UF_6) gas composition. In fact, no voltage componenet was observed that could be identified as electron collection (t_c ~ μsec) in the signal voltage profile. For the small diameter chambers, such as those used for the He(UF_6) gas measurements, first order diffusional losses to the walls are also likely loss candidates considered. However, the PIC method, for fixed electrode geometry, gas fill composition and pressure, allowed only combined effects of losses of either first or second order to be observed. Therefore, it is difficult to distinguish between the different loss mechanisms for a particular order of loss. However, comparing the short time (< 10^{-8} sec) required for any kind of electron attachment process [29] to the relatively long average lifetime (τ) of the ions in diffusion processes (~1 sec, as shown in Table 3.2), one can safely conclude that the first order loss coefficient measured in the He(UF_6) experiment was due to diffusion of positive and negative ions. For rare gases, the first order loss coefficients have been shown to be directly related to the diffusion coefficient [10]. Table 3.2 presents a summary of the first order loss coefficient α_1 values and diffusion coefficients calculated using the α_1 values (Eq. 3.12) for a number of representative gases. Also included in the table are columns showing the temperature dependence of the first order loss coefficients and average ion lifetime.

Table 3.2: Summary of 1st Order Loss Results

Gas cmposition	1st-order loss coeff. α_1 (sec^{-1})	Diffusion coeff. D(m^2/sec)	Lifetime τ (sec)	Temp. dependence
1 atm He(%UF_6)	(@T=423K)	(@T=423K)	(@T=423K)	
0.1%	72.17	5.2×10^{-6}	1.92	$T^{-1.55}$
1.0%	92.27	5.5×10^{-6}	1.83	$T^{-1.34}$
3.9%	87.24	2.7×10^{-6}	3.73	$T^{-1.51}$
7.5%	69.72	4.6×10^{-6}	2.18	$T^{-0.52}$

The temperature dependence of the first order loss coefficient follows approximately $T^{-1.5}$ with the exception of the 7.5% UF_6 chamber.

Second order loss. The second order loss coefficients and their temperature dependence for He(UF_6) plasmas generated by using the UFTR is presented in Figure 3.22. Unlike the

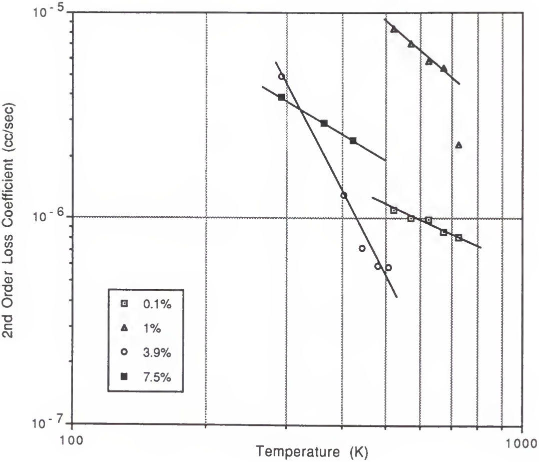

Figure 3.22: 2nd Order Loss vs Temperature Plot
Using the UFTR, 1 atm He(%UF6)

first order loss coefficient which showed a constant $T^{-1.5}$ dependence, the second order loss coefficient showed a temperature dependence which increased from a minimum of $T^{-1.0}$ to a maximum of $T^{-4.05}$. This is shown graphically in Figure 3.22. However, as with the first order loss coefficient, the result for the 7.5% chamber was still an anomaly with a $T^{-0.52}$ dependence. The variation of the second order loss coefficient with UF_6 concentration showed that the second order loss coefficient also appears to peak at 1.0% UF_6 concentration. The results obtained for measurements performed with a fission chamber filled with 10 atm helium, and one filled with 20 atm N_2 are shown in Figure 3.23 and 3.24, respectively. Table 3.3 shows a summary of the second order loss coefficient obtained for the various gases used in this study, including their temperature dependence.

Electrical conductivity calculation. Using the charge collection time t_c, defined earlier, and its relationship established with respect to the electrical conductivity of the ionized medium from which it was experimentally determined, values of the electrical conductivity were calculated. These results are shown in Figures 3.25 through 3.28.

Table 3.4 presents the mobility data calculated using the collection time which was directly measured from the oscilloscope.

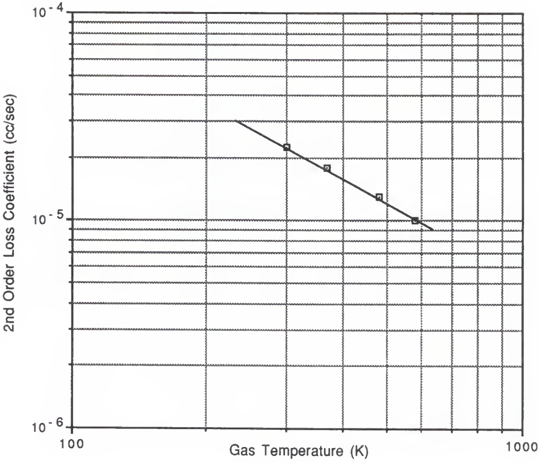

Figure 3.23: 2nd Order Loss Coefficient vs Temperature Plot using the Co-60 Source, 10 atm He(Fission Chamber)

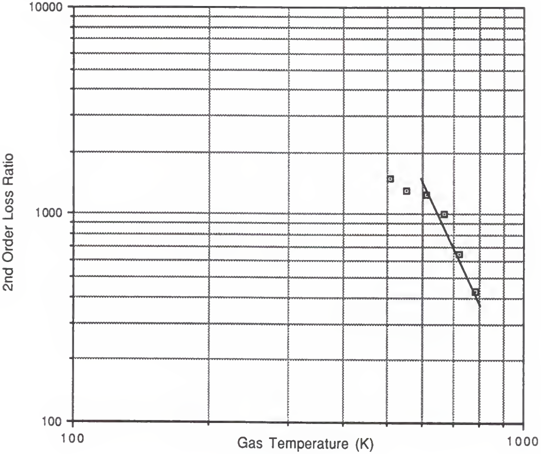

Figure 3.24: 2nd Order Loss Ratio vs Temperature
Plot using Co-60 Source, 20 atm Nitrogen

It was assumed that the plasmas generated in the He(UF_6) gas were composed of negative and positive ions based on their collection time measurement results.

Table 3.3: Summary of 2nd Order Loss Results

Gas	Ionization Source	α_2 (cm^3/sec)	Temperature dependence
1 atm He with:		(@T=523K)	
0.1% UF_6	UFTR	1.12×10^{-6}	$T^{-0.92}$
1.0% UF_6	UFTR	8.27×10^{-6}	$T^{-3.43}$
3.9% UF_6	UFTR	4.09×10^{-7}	$T^{-4.09}$
7.5% UF_6	UFTR	1.72×10^{-6}	$T^{-1.33}$
6 atm He	Co-60	2.1×10^{-5} (@T=293K)	-
20 atm N_2	Co-60	-	$T^{-2.78}$
(Fission Chamber)			
10 atm He	Co-60	1.3×10^{-5}	$T^{-1.15}$
(@T=493K)	UFTR	5.3×10^{-5}	-
1 atm Ar	Co-60	1.1×10^{-5}	-
(@T=293K)	UFTR	4.5×10^{-5}	-

Table 3.4: Summary of Mobility Results of He(UF_6) Gas

Gas	Collection time, t_c (sec)	μ, Measured ($cm^2/V\text{-}sec$)
1 atm He(%UF_6)	(@ 423 K)	(@ 423 K)
0.1%	1.0×10^{-3}	5.05
1.0%	1.0×10^{-3}	5.05
3.9%	2.0×10^{-3}	2.52
7.5%	1.2×10^{-3}	4.21

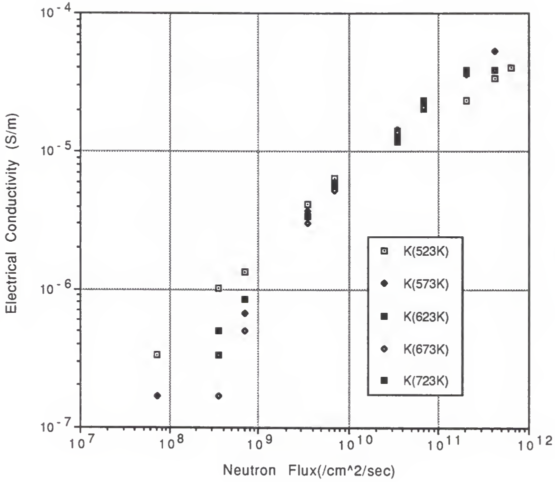

Figure 3.25: Electrical Conductivity vs Neutron Flux Plot using the UFTR, 931 Torr He(0.1% UF6)

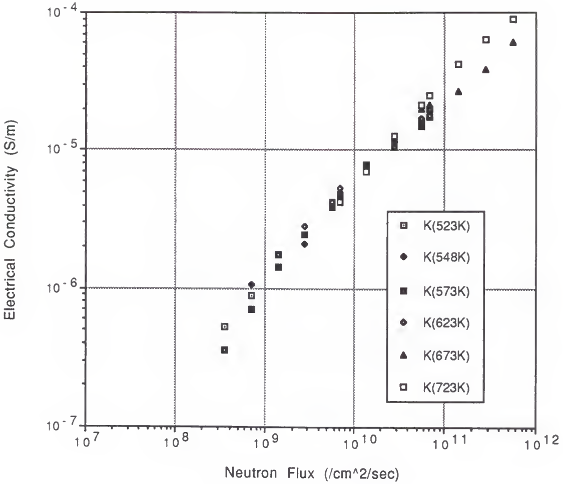

Figure 3.26: Electrical Conductivity vs Neutron Flux Plot using the UFTR, 981 Torr He(1% UF6)

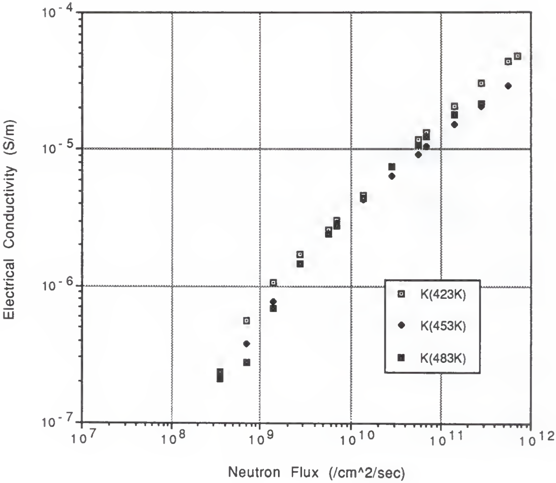

Figure 3.27: Electrical Conductivity vs Neutron Flux Plot
Using the UFTR, 960 Torr He(3.9% UF6)

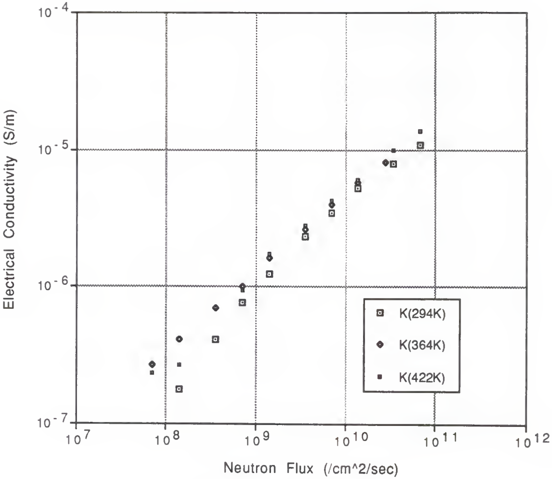

Figure3.28: Electrical Conductivity vs Neutron Flux Plot using the UFTR, 981 Torr He(7.5%UF6)

It was thought that the electrons, initially generated by fission fragments and γ-rays, were attached to the atoms and molecules of the supporting medium to make negative ions. Thus, the electrical conductivity measured for these gases was due mainly to ions and therefore appeared to be too low for $He(UF_6)$ gas compositions to be seriously considered as a fuel and working gas composition of the GCR/MHD system. Even though the measurements were performed at relatively low temperatures with respect to those of the proposed gas core reactor, extrapolation of the experimental data into the higher temperature region indicates that gases of this or similar gas compositions may not be optimum choices. It is noted that an ionized gas (i.e., plasma) must have an electrical conductivity of at least 10 [S/m] to be an effective working medium for a MHD generator [3]. Since the major difficulty derives from electron attachment with fluorine and/or fluorine compounds, gas compositions with reduced fluorine, while still using fissionable uranium as a fuel, would help reduce its tendency toward electron attachment. A suggestion has been advanced for the use of uranium compounds containing less fluorine than UF_6, such as UF_4. Potassium fluoride (KF) could serve as both a seed material and as a fluorine scavenging agent. Such a gas composition would have considerable promise for use in reactor systems [30]. However, this would no longer be a gas core reactor, but rather a vapor core reactor due to the high boiling point of UF_4 at the high operating pressure required.

Exploration of the possibility of developing this type of reactor would require, as a necessity, the addressing of the difficulties associated with vaporization and recovery of metallic uranium.

Columnar recombination. The experimental results obtained with an 1 atm Ar(5% N_2) filled fission chamber and a high pressure (10 atm) helium filled fission chamber showed effects that were attributed to columnar recombination loss predicted by Wilhelm [22]. In these measurements the plasma kinetic characteristics of the gas mixtures are studied independently with both γ-ray field and neutron induced fission fragment ionization sources. Ionization by the γ-ray source was accomplished both with the ^{60}Co irradiator and the UFTR, where, in the latter case, fission reactions were held to a minimum by use of a cadmium thermal neutron filter. Figures 3.29 and 3.30 show the effect of fission induced plasma loss compared to that occurring in γ-ray generated plasmas. At the same plasma production rate, the loss of the fission induced plasma is much higher than that of the plasma generated by the γ-rays. In comparison to plasma losses in the γ-ray generated plasmas, the fission generated plasma lost ~70 % of its density in some type of intermediate process which has been assumed to be columnar recombination before the individual columns homogenized and became subject to volume recombination. The loss coefficients measured with different ionization sources are summarized in the table 3.3. A significantly increased overall recombination coefficient

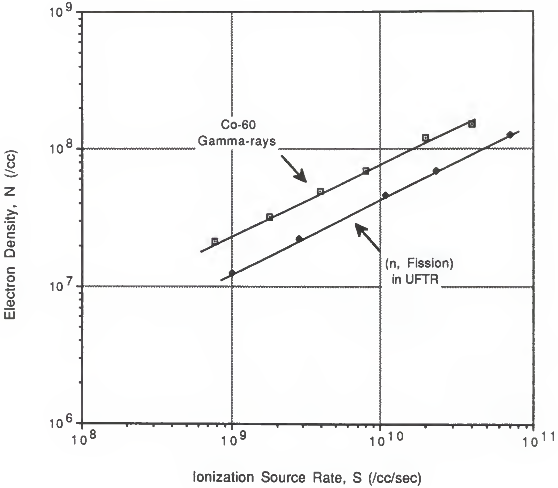

Figure 3.29: Electron Density vs Source Curve for 10 atm He filled fission chamber in UFTR compared with N-S Curve in Co-60 Source

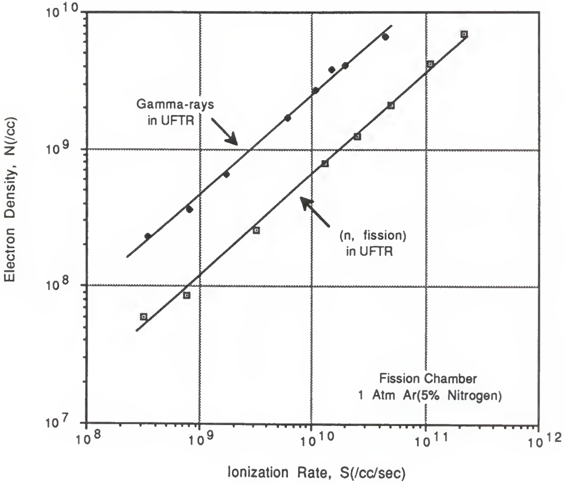

Figure 3.30: Comparision of N vs S for with and Without Fission Fragments in UFTR (1 Atm Ar(5% Nitrogen) Fission Chamber)

was exhibited for the fission fragment induced plasmas as compared to coefficients obtained for γ-rays generated plasmas (see Figure 3.31) which is assumed not to have a columnar recombination loss effect.

3.3.3. Discussion

Sources of error. A possible source of error in the He(UF_6) experiment was chamber positioning inside the thermal column of the UFTR since the experiment used four ion chambers with different gas compositions. Different locations of ion chambers in the reactor would result in errors in evaluating neutron flux as a function of reactor power. Since the system electronics were found to be exceptionally stable, no significant error was thought to be caused by the system electronics. The high voltage pulse amplitude was observed to have ± 0.3% fluctuations between repetitions during 10 hours operation which is normal time required for one experiment to be completed. Over this period the signal base line drift was observed to have been less than ± 1 mV. The method used to determine the system capacitance was thought to have a fairly large measurement error (± 5 %) due to the uncertainty in the values of the three different standard capacitors utilized in indirect capacitance measurement. Other sources of errors are end effects and space charge effects. End effects are electric field distortion near the boundary of the ion chamber

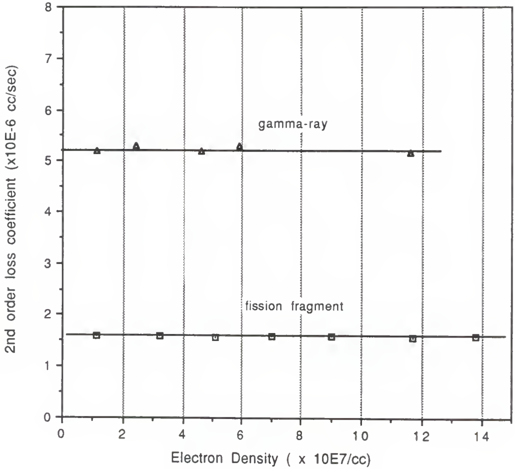

FIgure 3.31: 2nd Order Plasma Loss Coeff. Obtained from 10 atm He-4 Ionized with Fission Fragment and Gamma-Rays

effective volume which have been found to reduce the observed mobility up to 12 % in a variety of gases [31]. The distorted boundary of the ion chamber effective volume can cause error in evaluating plasma density and source generation rate, thereby affecting all the associated parameters calculated using them. Therefore, an absolutely accurate definition of the effective volume is necessary. Space charge effects are when heavier, less mobile ions exert a coulomb force on electrons/lighter ions thus disturbing the observed mobility for the electron/lighter ion (10% to 30%) [29]. The electrons are collected relatively quickly at the anode, leaving behind the positive ions that move much more slowly and gradually diffuse by drifting outward toward the chamber cathode wall. The space charge represented by these net positive charges can appreciably distort the electric field from its value if the space charge were absent. Both of these errors, if present, would have resulted in mobilities and electrical conductivities somewhat lower.

Discussion. In evaluating gas media for application to nuclear/MHD power generation systems, several factors need to be considered. Although a few high purity gases were investigated, other experiments were performed with gases that were easily obtained through reasonable care in system preparation and purification. Such gases which could be easily prepared without requiring extensive care in handling, nor necessitating ultra bake-out of its containment system would be considered as practical working media for our experimental purpose.

Two important findings observed during this study are the confirmation of columnar recombination in the fission fragment generated plasma, and immediate electron loss in the He(UF_6) plasma and resultant low electrical conductivity of the gas. Both facts will affect negatively in the gas core reactor performance if these effects still exist in the proposed high temperature and pressure conditions. The evidence of enhanced plasma loss by columnar recombination observed in the high pressure He and Ar plasmas generated by fission fragments suggested that this type of plasma loss should be studied in depth, since it can play an important role in the proposed gas core reactor/MHD converter system which is also based on fissioning plasma. The electrical conductivities measured for the He(UF_6) gas with varying degree of UF_6 mole percentage were too low to be considered as a possble fuel gas composition for the GCR/MHD system at the present measurement conditions. Experimental conditions, however, for these measuremts were too low in temperature (maximum 730 K) and neutron flux (maximum, $\sim 5 \times 10^{11}$ /cm^2-sec) to be considered as possible simulation of working environment of the gas core reactor. The He(UF_6) gas compositions might not be an optimum combination for the GCR/MHD system due mainly to the high electron affinity of the fuel gas. A possible alternative combination for the fuel and working fluid might be UF_4 with KF as a seed and fluorine scavenging gas. However, this would no longer be a gas core reactor, but rather a vapor core reactor due to the high boiling point of UF_4 at the high operating pressure required. Exploration of the possibility of developing this type of reactor would require, as a necessity, the addressing of the difficulties associated with vaporization and recovery of metallic uranium.

The PIC experiments performed with commercially available ionization chambers were temperature limited due to excessive leakage currents that occurred when the chambers were operated at higher temperatures. Most of the kinetic measurements performed were, thereby, restricted to temperatures below 730 K. To be able to perform measurements at higher temperature one would need to develop chamber systems which could avoid the leakage problem.

From the equilibrium type measurements presented thus far in this study, it can be concluded that the PIC technique for plasma diagnostic is an effective and significant tool for the study of the kinetics of plasmas, particularly in high pressure gases. The newly developed PIC-based plasma diagnostic system has been sucessfully used to measure various plasma parameters such as plasma generation rate, plasma density, and electron/ion mobility. Using the measured parameters it was possible to evaluate the plasma loss mechanisms, including columnar recombination. The close agreement of the results of these measurements with the findings of other investigators demonstrates that the PIC technique is a valid approach.

The principal limitation encountered in applying the PIC technique to the study of high temperature ionized gas (plasma) derive from the excessively high leakage current characteristics observed under high temperature operation with the commercially available ionization chambers used during the study. Therefore, it would be worthwhile to develop an experimental system which basically improves the performance of the PIC technique by extending the working temperature range to higher values than the commercial chambers can normally tolerate. Additionally, there continues to be a need for incorporation or use of other techniques in parallel with the PIC system for intercomparision and complement. This was the principal motivation for undertaking the development of a more versatile and higher capability instrumentation system.

In the following chapter, the development of the concepts and implementation of a computerized multiprobe ionization chamber (MPIC) plasma diagnostic system, which is basically a combination of PIC, conductivity and Langmuir probes, will be described and its performance evaluated. The system is comprised of a multiprobe ionization chamber and associated electronics which is controlled by a microcomputer using the General Purpose Interface Bus (GPIB) protocol [40]. The design of the system also takes into account the need for compatibility with the harsh environments to which it would be subjected, i.e., radiation fields (neutron, γ-rays) and corrosion of materials by fluorides at high operating temperatures.

CHAPTER 4
DEVELOPMENT OF MULTIPROBE IONIZATION CHAMBER (MPIC) PLASMA DIAGNOSTIC SYSTEM

The practical limits envisioned for the PIC system's applications to plasma measurement served as the motivation for and the development of a new plasma diagnostic system. The new Multiprobe Ionization Chamber (MPIC) system, was developed to enable the measurement of plasma characteristics at much higher temperatures and higher densities than the conventional PIC system was capable of reaching. Additionally, the need for intercomparison of the PIC technique with other more traditional methods was considered highly desirable.

4.1. Design and Construction of Multiprobe Ionization Chamber System

In practice, it is quite difficult to develop a single plasma diagnostic system which can perform measurements of all of the characteristic parameters of a plasma system at the same time. Yet there is always a need for having better and more useful plasma diagnostic tools available to help in the research and development of plasma physics systems.

The desirable features of an ideal plasma diagnostic systems may be summarized as follows:

1) parameters; measure all important plasma parameters
2) redundancy; measure each parameter with more than one technique, if possible
3) accuracy; attain accuracy of measurement of a few percent
4) spatial and time resolution; have active region of measurement large enough to be representative but small enough to minimize shape gradients, and to have characteristic sampling time short enough to allow measurement to follow the characteristic time changes of the system operational parameter
5) computer analysis; use computer system to record, store and analyze data
6) experimental technique; use experimental technique which improves signal-to-noise ratios.

The multiprobe plasma diagnostic system is basically a combination of several different techniques to increase the capabilities for measuring various parameters and also of cross-checking parameters measured by different methods at the same time. It consists of the Multi-Probe Ionization Chamber (MPIC) which contains Pulsed Ion Chamber (PIC), conductivity and Langmuir probes, a high temperature heater and cooling system, electronic circuits for system control, and a personal computer (Macintosh series) for data acquisition and analysis. This system thus fulfills many of the features of the ideal diagnostic system cited above.

4.1.1 Description of Multiprobe Ionization Chamber (MPIC)

The design of MPIC and its material composition are shown in Figures 4.1, 4.2, 4.3, and 4.4. The parts list of the MPIC, which is also serve as legend for Fig.4.1, is shown in Table 4.1. Detail specifications of the design are listed in Table 4.2. The main feature of this design is the enclosure of multiple probes in one chamber, including built-in heating and cooling systems for high temperature operation.

Geometry The multiprobe ionization chamber, basically, is an ionization chamber having a coaxial electrode configuration (including a guard electrode) with two additional field probes (also operable as Langmuir probes) inserted between the cathode and anode. Providing a guard electrode in the design is crucial to attaining accurate definition of the sensitive volume of the chamber and in minimizing the leakage current for the extremely high temperature conditions anticipated for the experiment. The chamber was designed and constructed to endure a maximum temperature of 1500 K and a maximum pressure of 50 atmospheres.

A major problem for the design of a high temperature ionization chamber was the drastically reduced electrical resistivity of an electrical insulator when exposed to high temperature. A study of temperature dependence of the

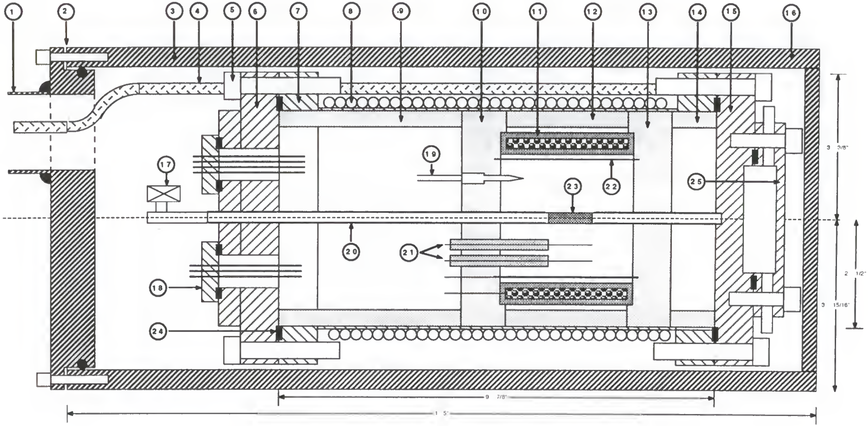

Figure 4.1: MPIC and Chamber Housing

Table 4.1: MPIC Parts List

PART	SPECIFICATION
1. Cable Conduit	Al Tube, 1.875" OD, 1.759" ID, 6'6" L
2. Housing Flange	Aluminum plate 7.875" Dia.
3. Housing Cylinder	Aluminum, 7.25" OD, 7" ID, 16.1875" L
4. Return Gas Tube	Aluminum Tube, 1/4" OD, 2" L
5. Bolts	Hex head, 5/16-24 x 2 1/4"
6. Chamber Flange	304 S.S. Flange OD = 6.75", 18 bolt holes, 0.33" dia, 5.96" bolt circle
7. Pressure Chamber	Full Nipple, Type 304 S.S., Tube OD = 5", T=0.083", L = 9.87", Flange OD=6.75", 18 bolt holes, 0.33" D, 5.96" bolt circle
8. Coolant tube	Aluminum tube wound helically around the Pressure Chamber, OD = 0.186", T= 0.032"
9.12,14. Thermal Insulator	Alumina Tube
10,13. Thermal Insulator	Alumina Disk
11. Heater	Thermocraft model RH251.
15. End Flange	6.75" OD , 304 S.S. flange with coolant channel
16. Housing Flange	7.875" Dia. x 0.375" Thick Aluminum
17. Gas Seal Pipe	1/4" S.S. Tube with Gas Valve
18. Fedthroughs	
19. Thermocouple	K-type
20. Guard Electrodes	Molybdenum tube, OD = 3/8", T= 1/16" L= 4" & 3 1/4"
21. Field Probes	Tungsten probe electrically insulated by Alumina tubes.
22. Cathode	Molybdenum tube, L = 3", T = 0.03", ID = 2.8"
23. Anode	Molybdenum rod, OD = 3/8", L = 1"
24. Copper Gasket	Huntington model# G-675
25. Cooling Flange	4.5" OD, 304 S.S. Flange

Table 4.2: Multiprobe Ionization Chamber Specification

PARAMETER	CHARATERISTICS
Max. Temperature	1500 K
Max. Pressure	50 atm (735 psi)
Anode	Material : Molybdenum (Mo) I.D. : 1/4" O.D. : 1/2" Length : 1/2"
Cathode	Material : Mo I.D. : 2.96" O.D. : 3" L : 3"
Guard Electrode	Material : Mo O.D. : 1/2" I.D. : 3/8" L : 1 x 5 1/2", 1 x 4 1/2"
Sensitive Volume	88 cm^3
Field Probe	Material : Tungsten (W) Diameter : 1/32" L : 1" (exposed section)
Insulator	Material : High purity (≥99%) Alumina (Al_2O_3) Dimension: Refer attached Figures
Flange	Material : Type 304 S.S. Diameter : 6" Thickness: 1" 18 x 13/32"(ϕ) holes, bolt circle r=2 3/4"
Coolant pipe	Material : Aluminum I.D. : 3/16" O.D. : 1/4" (I.D.= 1/4", O.D.= 3/8", L = 4", 3 1/2")
Gas valve	Nupro model SS-2H, or equivalent gas pipe diameter : 1/4" Material : S.S. 304
Connectors	Cathode : BNC Field probes : BNC Anode : BNC Insulator : Alumina

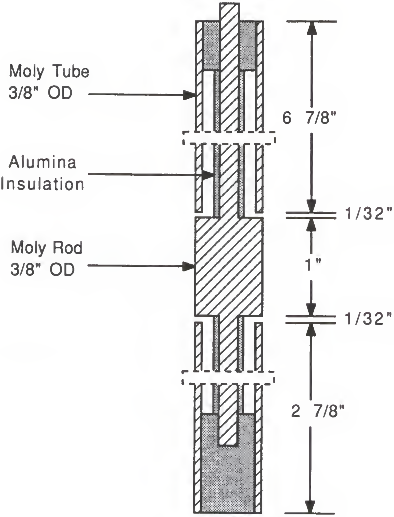

Figure 4.2: Anode & Guard Electrodes Detail

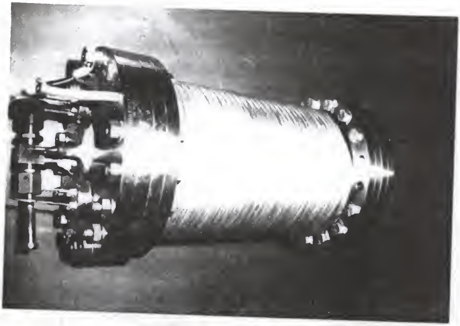

(a)

(b)

Figure 4.3: Photographs of the MPIC System; (a) Assembled MPIC, (b) Cathode and Guard Electrode

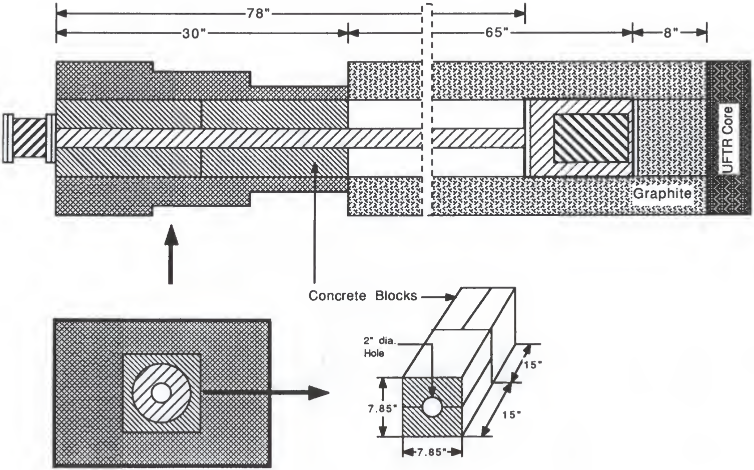

Figure 4.4: Experimental Assembly Inserted in the Thermal Column of the UFTR

electrical resistance for typical metal oxide insulation materials such as MgO, Al_2O_3 and SiO_2 shows a rapid decrease in resistance with increasing temperature [32]. The results, as shown in Figure 4.5, illustrate that while the resistivity of the commercial grade insulators at room temperature is on the order of 10^{14} Ωm, at 900 K the resistivity drops to ~10^6 Ωm. Since the variation in the resistance drop is almost exponential, the situation would be expected to be much worse at the temperature that was planed to be approached (i.e., 1500 K). However, this problem was solved by extending the contact position between the insulator and guard electrode beyond the high temperature region and maintaining an auxiliary water cooling system such as shown in Figures 4.1 and 4.3. Coolant channels are provided in the flange around the connectors, where leakage current might exist at high temperature, to cool down the local temperature even though the temperature inside the chamber is high. The gas was confined within the ceramic (Alumina) thermal insulators to prevent convection of the hot gas out of the sensitive volume and also to provide rapid temperature drop between the sensitive volume and probe connection positions.

Sensitive Volume The sensitive volume chosen for the ion chamber is determined by fission fragment track range in a series of candidate fill gases, for pressures greater than 1 atm. The range of a typical fission fragment is about 1.75 cm in 1 atm air. This is approximately half that of a 5 MeV alpha particle [31]. Estimation of fission fragment range R

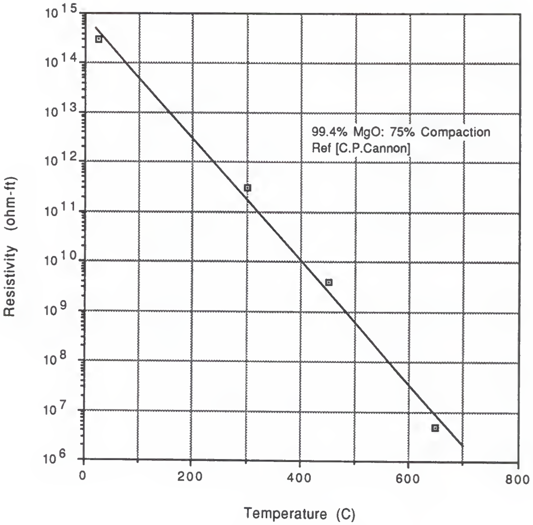

Figure 4.5: Resistivity vs Temperature For Typical MgO Type I Test Cable

in stopping media was obtained relative to the known range in air, R_a, by the relationship [18]

$$R = R_a(\rho_a/\rho)(A/A_a)^{1/2} \text{ cm}, \qquad (4.1)$$

where $\rho(g/cm^3)$ is density and A is atomic mass. The fission fragment range in 1 atm helium gas is then roughly $3.8R_a = 6.6$ cm. For a gas at temperature T(K) and pressure p(Torr), this reduces to

$$R = (20.1)R_a(\sqrt{A}/M)(T/p) \text{ cm}, \qquad (4.2)$$

where M is the molecular weight of the gas. The fission fragment range in 5 atm, 1500 K helium gas is approximately $3.96R_a = 6.9$ cm.

The volume of the chamber had to be large enough to minimize diffusional plasma losses at the wall and to increase the interaction of the radiation within the gas volume rather than with wall materials. However, the size of the chamber also had to be small enough for it to fit into the thermal column of the UFTR where the maximum thermal neutron flux was locally available. The dimensions thus chosen for the chamber, inner diameter of 7.62 cm and height of 7.62 cm, are greater than the fission fragment range, yet are still small enough for the chamber to fit into the thermal column (see Fig.4.1).

The thickness of cylinder shell (chamber housing) under internal pressure was calculated by using an equation recommended by the ASME Boiler & Pressure Vessel Code [33]

$$t = \frac{PR}{SE-0.6P} \tag{4.3}$$

in which:

t = minimum thickness [in]

P = allowable internal pressure [psi]

S = allowable material stress [psi]

E = welded joint efficiency [percent]

R = inside radius [in]

The values adopted for the determination of t are: P = 50 atm (735 psi), R = 2 17/32", S = 115,000 psi and E = 80 %. The minimum yield strength of commercial Type 304 Stainless Steel is 115,000 psi [34]. The calculated thickness with these values is 0.02", therefore, the design value of 0.083" is thick enough to withstand the internal pressure.

Material   Selection of appropriate materials for electrodes and electrical insulators, as well as structural and cladding materials, is difficult since those systems are to be exposed to highly corrosive UF_6 gas at high temperature. In general, the containment of highly reactive fluoride gas at high temperature, requires the use of protective material that will either not react in this environment or will form stable nonvolatile fluorides, thus passivating the surface against further reaction. For our purpose, the container would serve also as an electrode; therefore, its surface material should accommodate high electrical conductivity even after passivation of its surface. Previous studies show that almost all of metals and ceramics which have high enough melting point (>2000 K) react with fluorine and form a fluoride layer [35,36]. The corrosion rate of metals and ceramics is a major concern in this problem and one has to choose the materials which have the lowest corrosion rates. Also, the materials should have low neutron absorption cross-sections. For thermal and electrical insulator, pure alumina (Al_2O_3) is likely to be a best choice in terms of chemical, mechanical and nuclear characteristics. The electrode material of choice is pure molybdenum.

Functions The center electrode (anode) and outer electrode (cathode) were used as PIC probes to measure electron (and/or ion) number density and mobility. Availability of these properties enabled the calculation of electrical conductivity of the plasma through the use of the relationship

$$\sigma = Ne\mu \tag{4.4}$$

where σ is electrical conductivity, and μ is mobility.

In addition, combining these properties with steady state current measurement, provides a means of determining the diffusion coefficient, recombination loss coefficients, and ionization source rate. Since the diffusion of charged particles is related to their mobility, the Einstein relationship allows one to calculate the temperature of the charged particles using the values of the diffusion coefficient and mobility;

$$\frac{D}{\mu} = \frac{kT}{e} \qquad (4.5)$$

where D is the diffusion coefficient, k is Planck's constant and T is the absolute temperature of the gas.

The conductivity probe, which consists of two field probes, anode and cathode, was used to measure the electrical conductivity of the plasma directly and the results were cross-checked with the ones obtained using the PIC probe.

The Langmuir probes, used as field probes when operated as a conductivity probe, provided information pertaining to electron temperature, electron density, and plasma potential.

A system block diagram is shown in Figure 4.6. All of the probes can be operated at the same time or operated separately in certain operating regions where a particular probe measurement may not be applicable.

In order to assure proper performance of the chamber under high temperature conditions, each part of the chamber was cleaned thoroughly before assembly and the chamber vacuum-baked after assembly.

4.1.2 Theory of the measurements

Since the operational theory of the PIC technique already has been presented in Chapter 3.1.1., only the theories which pertain to measurements of the conductivity and Langmuir probes will be presented here.

Conductivity Probe The conductivity probe makes direct use of Ohm's law for electrical conductivity (without

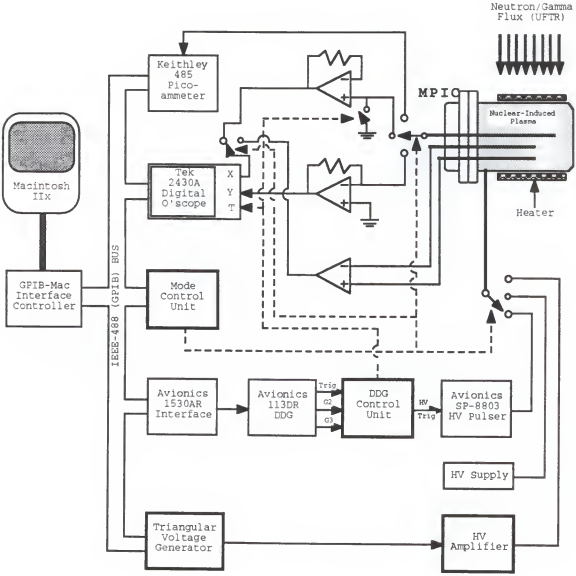

Figure 4.6: Block Diagram of Computer Controlled Multiprobe Plasma Diagnostic System

magnetic field) to measure electrical conductivity σ of a gas.

$$\sigma = \frac{j}{E} \tag{4.6}$$

By obtaining a measure of the total current between the cathode and the anode of the ion chamber, one can calculate the current density, j, based on the geometry of the chamber. For a coaxial chamber,

$$j = \frac{I}{2\pi r l} \tag{4.7}$$

The field strength, E, can be deduced from measurements made with the field probes in which the plasma is sensed at two different radii.

$$E = \frac{V}{r \ln(d/c)}, \quad c \leq r \leq d \tag{4.8}$$

where l is the sensitive length of the center electrode and (d/c) is the ratio between the distances of the two probes from the center axis.

The voltage difference ∂V between the two field probes (positioned at the radii c and d in Figure 4.2) was measured as a function of the current I to the anode with the guard electrode kept at the anode potential (ground). Within a certain range, the relationship between ∂V and I was linear. In that range, for a fixed temperature and reactor power, one can formulate the relationship:

$$\partial V = R_o I + V_o \tag{4.9}$$

with R_o and V_o being constants. The differential voltage difference $d(\partial V)$ as a function of a differential change in I is equal to the differential potential drop in the plasma between the two cylindrical surfaces through the probes, concentric with the center electrode (anode). In that case the relationship between the plasma conductivity σ and R_o which is equal to $d(\partial V)/dI$ is found by inserting equations (4.6) and (4.7) into equation (4.5) to yield

$$\sigma = \frac{\ln(d/c)}{2\pi l R_o} = \frac{G}{R_o} \tag{4.10}$$

where G (= $\ln(d/c)/2\pi l$ = 2.54 [/m]) is a geometrical factor determined by the geometry of chamber and probe locations.

Langmuir (Electrostatic) Probe The standard diagnostic for making measurements of plasma parameters in low-temperature plasmas (temperature <200 eV) is the Langmuir probe [37], a shaped conductor (usually cylindrical, spherical, or planar) which is immersed in the plasma. The current drawn from the plasma by the probe, I, as a function of probe bias V_b, is called the probe characteristic. Figure 4.7 shows the typical Langmuir probe characteristics. Properties of the plasma are inferred by examining the probe characteristics. At voltages very negative with respect to the plasma, the probe repels all electrons and collects a small ion current. As V_b increases all the ions are repelled and the electron current I_e grows exponentially, assuming the

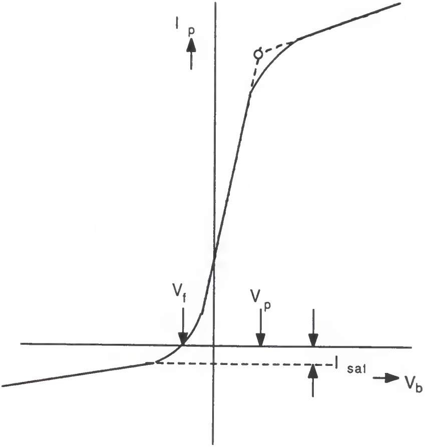

Figure 4.7: Semi-log Langmuir Cylindrical Probe Plot of Probe Current Against Probe Voltage

electrons have a Maxwellian distribution. In this region, I_e is given by

$$I_e = (AN_e e\sqrt{\frac{kT_e}{2\pi m_e}})\exp\left(\frac{e(V_b-V_p)}{kT_e}\right), \qquad (4.11)$$

where A is the probe area, and V_p is the plasma potential (We are using the convention that collected electrons represent a positive current). In order to be able to calculate the plasma electron temperature and electron density, one must plot the data of $(V_b, \ln(I))$ on semilog format as shown in Figure 4.7. Then the expression for the slope, given as

$$\text{slope} = \frac{d(\ln(I))}{dV_b} = \frac{e}{kT_e} \qquad (4.12)$$

permits one to calculate the plasma electron temperature T_e using the linear part of the probe characteristic curve. When the plasma potential is reached, the rate of increase of I slows. Here one collects every electron which reaches the probes. Simple theories predict that at the plasma potential, dI/dV_b will be a maximum [38]. For a cylindrical probe, the collected current continues to grow with increasing probe bias as the sheath around the probe expands. The electron density can be found from

$$N_e = \frac{I}{Ae\sqrt{kT_e/2\pi m_e}} \qquad (4.13)$$

,where I is measured at V_p.

4.1.3. MPIC System Electronics

The entire MPIC system shown in Figure 4.6 was operated and controlled with a Macintosh IIx personal computer and National Instrument LabVIEW [39] software package. All the other commercially available instruments employed in this setup were IEEE-488 (or GPIB) compatible. The General Purpose Interface Bus (GPIB) is defined by ANSI/IEEE Standard 488-1978. The GPIB is an 8-bit parallel digital bus with full handshake and interface management capabilities. It has been used for interfacing programmable devices with computers.

Computerized operation of the system required IEEE-488 compatibility of electronic control circuit and use of IEEE-488 protocols [40]. However, highly sophisticated, microprocessor-based IEEE-488 instrument capability was not needed. A relatively simple system was developed which can be partially compatible with IEEE-488 instruments by developing a circuit which could monitor the IEEE-488 bus-lines and pick up the necessary information from the bus-lines. Thus it was possible to drive the switching system remotely between different functional modes and measuring sequences. Detail system circuit diagrams are shown in Figures 4.8, 4.9, and 4.10.

The system control electronics are comprised of three separate parts for the operation of PIC, conductivity and

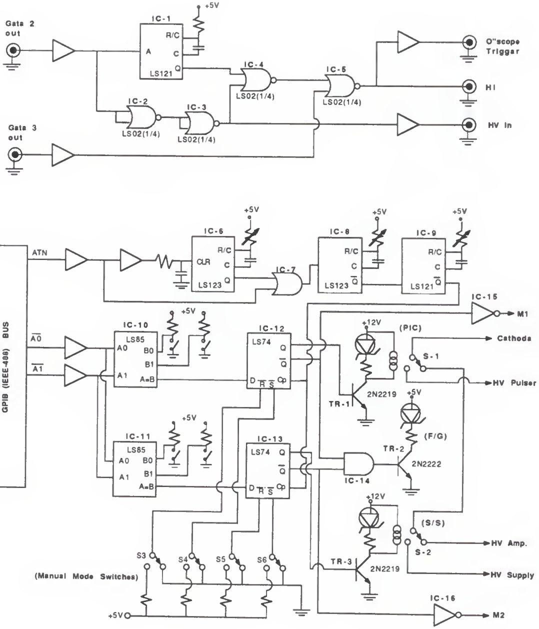

Figure. 4.8 : Electronic Circuit Diagram for the MPIC System

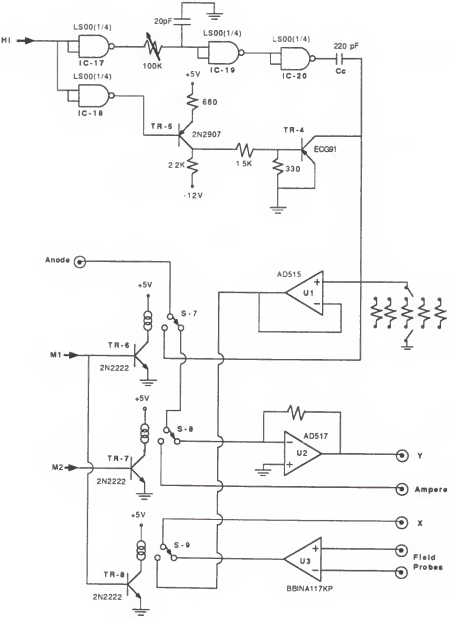

Figure. 4.9: Electronic Circuit Diagram for the MPIC system (continued)

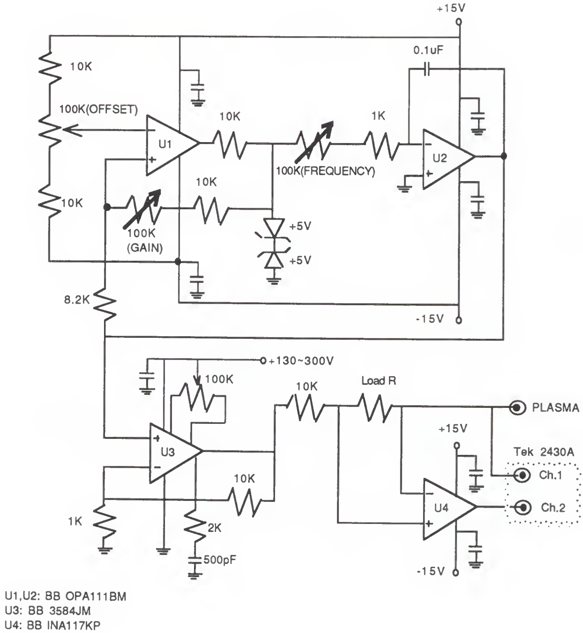

Figure.4.10: Circuit Diagram for Conductivity Measurement

Langmuir probes. In addition to these, a mode control system is provided for computerized control of each different mode.

PIC electronics required a fast rising high voltage pulser (rise time < 100 nsec), an impedance switching circuit and a timing circuit. The high voltage pulser can provide a pulse of up to -1000 V height and 10 msec duration. The characteristics of the high voltage pulser is shown in Table 4.3. The impedance switching and timing circuits are shown in part of Figures 4.8 and 4.9.

The instrumentation systems utilized to set up the plasma diagnostic system were a Tektronics 2430A digital oscilloscope, a Cal Avionics 3-channel digital delay generator and its GPIB interface controller, and a KEPCO high voltage amplifier.

The conductivity measurement circuit (also operable as a Langmuir probe circuit), which is shown in Figure 4.10, consisted of a triangular voltage generator and a high voltage bipolar operational amplifier (KEPCO model BOP100). When a sweeping triangular wave voltage, which can have both polarities (up to ±100 V) without distortion at the transition between the different polarities, is applied between the anode and the cathode of the MPIC (i.e., across the plasma), one can measure the current flowing in the closed circuit and potential drop at the plasma at the same time. With these data one can obtain a characteristic I-V curve which can be used for the deduction of the plasma properties. Generally, the Langmuir probe electronic system

Table 4.3: Specifications of High Voltage Pulser

<table>
<tr><th>PARAMETER</th><th>CHARACTERISTICS</th></tr>
<tr><td>Model</td><td>CAL-AV SP-8804</td></tr>
<tr><td>Pulse Height</td><td>0 to -1000 V continuously variable by using the front panel control knob. Baseline shifts above 850 V</td></tr>
<tr><td>Pulse Rate</td><td>limited by the Pulse Width as shown below
<table>
<tr><th>Pulse width</th><th>Maximum Pulse Rate</th></tr>
<tr><td>9 (msec)</td><td>10 (pps)</td></tr>
<tr><td>6</td><td>20</td></tr>
<tr><td>4</td><td>30</td></tr>
<tr><td>3</td><td>40</td></tr>
<tr><td>2.5</td><td>50</td></tr>
<tr><td>~1.2</td><td>100 maximum</td></tr>
</table></td></tr>
<tr><td>External Load</td><td>~300 pF capacitive loading only</td></tr>
<tr><td>Triggering</td><td>by External Trigger Pulse (2~5 V)
input impedance, 50 Ω</td></tr>
<tr><td>Pulse Width</td><td>determined by external trigger pulse width within the range of 250 μsec ~ 10 msec</td></tr>
</table>

requires a floating power supply and an isolation amplifier to avoid the relatively high voltage burden to the input of the signal measuring amplifier. But recent advances in IC technology have made it possible to produce extremely high common-mode voltage operational amplifier [41], so it was possible to make a Langmuir probe circuit without having to use an expensive isolation amplifier. A detail description of the circuits is presented as follows.

Timing circuit A circuit shown at the top of Figure 4.8 is a timing circuit for the high voltage pulse and impedance switching system. Timing relationships between the components outputs are shown in Figure 4.11.

The GATE 2(G2) OUT of Digital Delay Generator (DDG), which has 3 delay channels, generates a pulse with preset width and period. The pulse is fed into IC-1 (SN74LS121 :monostable multivibrator) and IC-2 simultaneously. IC-1 generates a pulse with fixed width (set by external R and C) and period that is the same as the G2 OUT pulse. IC-2 (and IC-3) works as a inverter and produces a delayed pulse (propagation delay time of ~10 nsec). The output of IC-3 is used to generate a high voltage driving pulse which has the same width and period as that of IC-3. IC-4 generates a pulse with a width that is always greater than G2 OUT. Combining pulses from G3 OUT and IC-4 by use of a NOR gate gives a high impedance pulse which is slightly delayed (~100 nsec) with respect to the leading edge of the high voltage driving pulse.

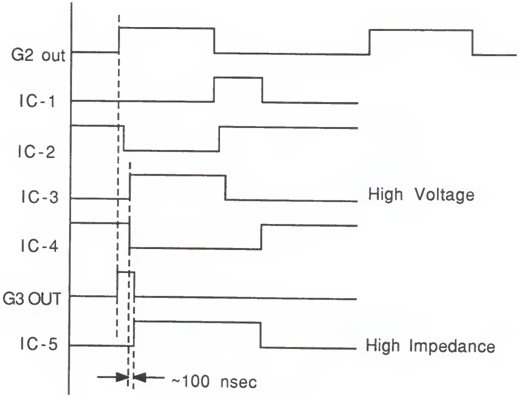

Figure 4.11: Timing Diagram for the High Voltage Pulse and High Impedance Switching

Mode selection & switching circuit The circuit shown at the bottom of Figure 4.8 is the mode selection and switching circuit. The 16 General Purpose Interface Bus (GPIB) signal lines can be divided into three buses: the data bus, the management bus, and the handshake bus. The data bus is composed of eight signal lines that carry data to be transferred on the GPIB. The management bus is composed of five signal lines that control data transfers. The handshake bus is composed of three signal lines that synchronize data transfers between instruments.

When Attention (ATN) is asserted, massages sent on the data bus are interpreted as commands or addresses. This is the key concept we utilized for the automatic mode change.

The last two digits of the data line (A0, A1) and ATN line of the GPIB Bus is monitored by the circuit continuously during operation of the experiment. When one tries to change the mode of measurement (for example; from PIC to steady state current measurement) by using a program written by a LabVIEW software (developed by National Instrument), the ATN management line is activated by the GPIB controller to designate instruments as talkers and listeners for an upcoming data transfer. Immediately following the ATN signal, in this case, is instrument address data. Then the data values are compared with certain preset numbers using 4-bit magnitude comparators (IC-10, IC-11).

When the address data is matched with preset address data, the comparator (IC-10,IC-11) generate an HIGH output which is used to derive D-type Flip-Flops (D-FF)(IC-12,IC-13). Information at input D of the D-FF is transferred to the Q output on the positive-going edge of the clock pulse, which is provided by the monostable multivibrator (IC-9). IC-6 to IC-9 are used to pick up the ATN signal from the GPIB bus and generate a delayed clock pulse which, now synchronized with the address data, can be used to trigger the D-FF (IC-10,IC-11). Therefore, the address data, matched only after the ATN signal is detected, are used to change the modes. When the Q output of IC-12 is HIGH, it turns on the TR-1 and allows current flow into the coil of the relay switch, thus actuating switch S-1. The same technique applies to IC-13 and it actuates switch S-3. When the Q outputs of IC-12 and IC-13 is LOW (then, complementary is HIGH), they actuate TR-2 to turn the LED light on. Therefore, this mode is set as the default mode. Also in this case, the complementary Q output of IC-12 (or IC-13) is fed to IC-15 (or IC-16) which now generate a HIGH output to the base of transistors TR-6 and TR-8 (or TR-7) to derive switches S-7 and S-9 (or S-8). By this means, completely automatic mode selection and switching action is accomplished.

Since only the last two digits of the 8-bit address data were compared, one can control four different instruments with this circuit. But the same technique can be applied to expand the number of controllable instruments up to 16.

For manual control of the mode selection, four toggle switches (S-3~6) are provided on the front panel. These are connected to SET and RESET inputs of the D-FF (IC-12, IC-13). Whenever one applies a HIGH signal to these inputs, using the selection switches, the D-FF generate Q or complementary Q output regardless of their D-input. Therefore, one can interrupt the automatic mode control to set a particular mode by choosing an appropriate combination of manual switches. Table 4.4 shows the combination of switches to choose a particular mode of control by manual.

Table 4.4: Mode Selection by Manual Switch

Operating Mode	Switches*			
	S1	S2	S3	S4
PIC	OFF	OFF	**ON**	**ON**
F/G	OFF	**ON**	**ON**	OFF
S/S	**ON**	**ON**	OFF	OFF

* Switch numbers are different from those shown in the diagram. These #'s represent physical location of switches on the panel ascending order from left side.(S1 for far left, S4 for far right)

Impedance switching circuit The impedance switching circuit consists of NOT gates (IC-17~20) and transistors (TR-4, 5). The transistor (TR-5) changes the level of the impedance switching signal from that of TTL to one ranging from 0 to -12 volts level to drive the other PNP transistor (TR-4). The latter transistor (TR-4) performs the switching operation. The TR-4 has a high unit gain bandwidth characteristic to satisfy the high switching speed requirement set for the system.

The need for the capacitance compensation circuit is explained below with the help of Figures 4.12 and 4.13. Without the compensation circuit, when the transistor (TR-4) turns off under the zero ionization source condition, the waveform at the collector of the transistor (TR-4) would look like that shown in Figure 4.13. The transient response of the collector voltage occurs because of the parasitic capacitance between the collector and the base of the transistor (TR-4). In other words, this phenomenon can be explained as follows. At the leading edge or rise of the switching signal, the collector voltage of the transistor (TR-4) instantaneously follows the base voltage with some small fraction of attenuation, but after there, it exponentially decays to the baseline with a long time constant, since the transistor (TR-4) is now in an OFF state with no appreciable flow of current. This transient response under zero ionization source conditions remains unchanged under normal measurement conditions and can cause erroneous results by inducing displacement of the baseline. Such a undesirable shift of the baseline due to capacitance coupling can be and has been compensated by the use of an added capacitor (C_c) and a compensation signal of opposite polarity (V_n in Figure 4.13) in phase with respect to the impedance switching signal. When the compensating signal (V_n) is

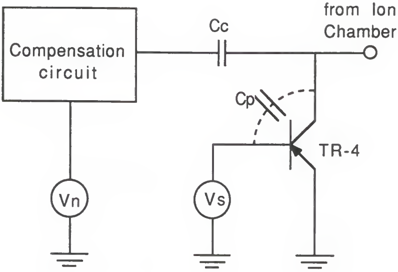

Figure 4.12: Impedance switching transistor and capacitance compensation circuit

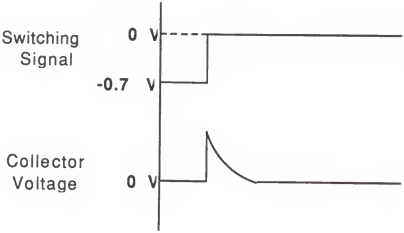

Figure 4.13: Waveform at the collector of transistor (TR-4) without compensation

transmitted through the coupling capacitor (C_c), it results in negative-going transient response at the collector of the transistor (TR-4), if the circuit is adjusted appropriately. The compensation component influences the impedance switching circuit only during the transient period. Even though a complete compensation circuit has not been accomplished, in removing the transient response, practically useful performance has been observed.

The compensation circuit is composed of the NOT gate (IC-17), which is located just after the IC-5, potentiometer (P-1), which is used to adjust the delay time of the compensation signal, two other NOT gates(IC-19,20), and the compensation capacitor (C_c)

Amplifiers A high input impedance operational amplifier (U-1) is used as a buffer amplifier. The amplifier has FET inputs and provides almost interference free measurement of the signal obtained at the collector of the transistor (TR-4). A second high input impedance operational amplifier (U-2) is used as a current-to-voltage converter. The current drawn from the anode during conductivity measurement (or Langmuir probe operation) is converted into a corresponding voltage ($V = -IR$) which is easier to manipulate. The final amplifier U-3 is a precision unity-gain differential amplifier offering high common-mode input voltage range operation. It is used for the electric field intensity measurement using field probes which requires a high common-mode voltage measurement system. The differential amplifier (U-3) provides suitable performance without having to use a costly isolation power supply.

Conductivity measurement circuit A typical conductivity measurement circuit (also operable as a Langmuir probe) basically consists of a triangular-wave generator and a high voltage amplifier (See Figure 4.10). The system described in this work uses an operational amplifier comparator, together with an integrator to generate the triangular-wave. A typical triangular-wave generated by such a circuit *is shown in Figure 4.14.*

When the comparator (U-1) has reached either the positive or negative saturation stage, the matched Zener diodes clamp the voltage V_a at either $+V_z$ (5V) or $-V_z$ (-5V). Let us assume that $V_a = +V_z$ at $t = t_o$. The current flowing into the integrator is $I^+ = V_z/(R_3 + R_4)$ and the integrator (U-2) output becomes a negative-going ramp, or

$$v_o(t) = v_o(t_o) - \frac{1}{C}\int_{t_o}^{t} I^+ dt = v_o(t_o) - \frac{I^+(t - t_o)}{C} \quad (4.14)$$

The voltage at pin 3 of the threshold detector (U-1) is, using superposition,

$$v_3(t) = \frac{R_3 V_z}{R_1 + R_2 + R_5} + \frac{(R_3 + R_4)v_o(t)}{R_1 + R_2 + R_5} \quad (4.15)$$

When $v_3(t)$ goes through zero and become negative, the comparator output changes to the negative-output state and $V_a = -V_z$. At this time, $t = t_1$, $v_o(t_1) = 0$, or from equation (4.12) one finds

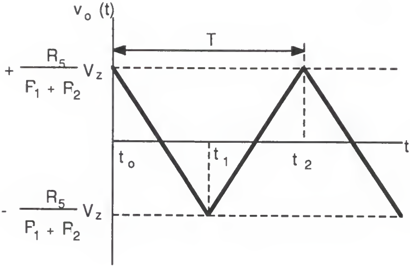

Figure 4.14: Typical triangular-wave generator output waveform

$$v_o(t_1) = -\frac{R_5 V_z}{R_1 + R_2} \tag{4.16}$$

The current supplied to the integrator for $t_2 > t > t_1$ is $I^- = -V_z/(R_3 + R_4) = -I^+$ and the integrator (U-2) output $v_o(t)$ becomes a positive-going ramp with the same slope as the negative-going ramp. At a time t_2, when

$$v_o(t_2) = \frac{R_5 V_z}{(R_1 + R_2)}, \tag{4.17}$$

the comparator (U-1) switches again to its positive output again and the cycle repeats. The frequency of the triangular wave is given by

$$f = \frac{R_1 + R_2}{4(R_3 + R_4)R_5C} \tag{4.18}$$

The amplitude can be controlled by the ratio $R_5V_z/(R_1 + R_2)$. The positive and negative peaks are equal if the Zener diodes are matched. It is also possible to offset the triangle voltage with respect to the ground if a DC voltage is connected to the inverting input of the comparator. The resistor R_7 was used to offset the waveform within the voltage range from -10V to +10V.

A photograph showing the circuits is presented as Figure 4.15.

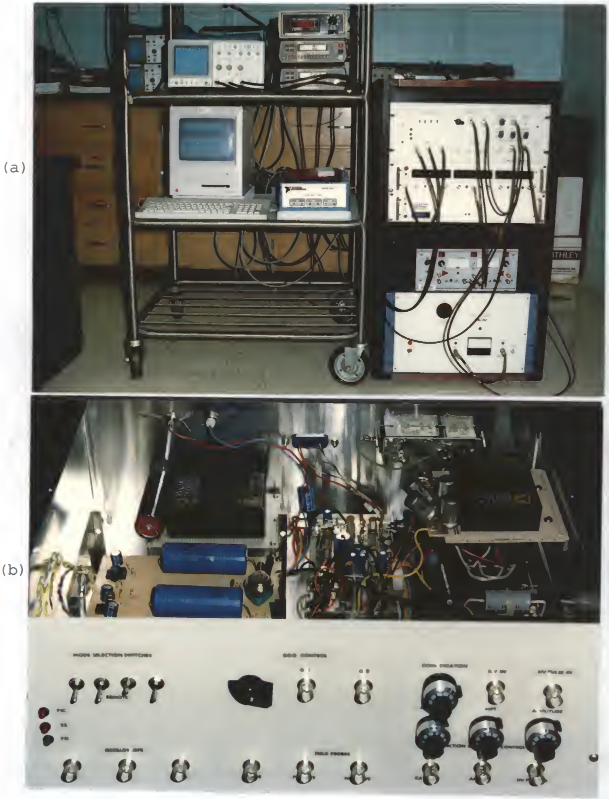

Figure 4.15: Photographs of the MPIC System;
(a) System Layout, (b) MPIC Circuitry

4.2. Multiprobe Ionization Chamber Preliminary Test

4.2.1. Multiprobe Ionization Chamber Preparation

Before the assembly of the MPIC, all of the parts were required to be cleaned, using high purity acetone and alcohol, and to be vacuum-baked. The metallic parts should have also been electropolished, but, unfortunately, electropolishing equipment was not available. Some of the grease deposits on the alumina insulator surfaces occurring during fabrication, could not be removed completely using acetone. The porous alumina fiber-based thermal insulator (ZIRCAR model AL30AA), which was chosen because of its extremely low thermal conductivity at high temperature, showed relatively low electrical insulation resistance when it was exposed to air. Moisture from the air was believed to be absorbed onto and into the insulator material. Figure 4.16 illustrates how the insulation resistance can be restored (or deteriorated) by removing (or allowing) the air moisture from (or into) the insulator. Therefore, the chamber, once assembled, should not be exposed to the air, or if it is, it should be vacuum-baked again.

After assembly, the MPIC integrity was tested by evacuating it using a Varian pumping station. Initially the chamber could not be pumped down below 1 x 10^{-4} torr because of a small leak around the anode feedthrough bond and

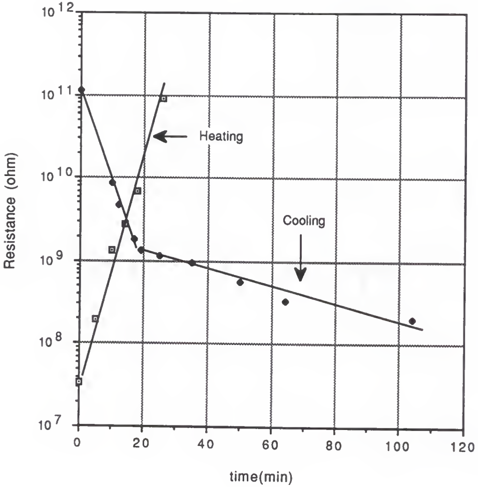

Figure 4.16: Resistance vs Time Plot During Heating and Cooling of ZIRCAR AL30AA Alumina

outgassing from the materials inside the chamber. The release of gas resulting from its desorption inside of an evacuated system is known as outgassing [42]. Once the leak was fixed using a high temperature Epoxy, the chamber was subjected to repeated cycles of baking from room temperature to 600 °C at intervals of 100 °C, with at least 24 hours at each temperature. After each baking cycle was completed, the chamber could be pumped down to 1×10^{-6} torr at room temperature. Once this pressure could be maintained for a day, the chamber was filled with 1 atmosphere research grade ^{4}He gas. It was then possible to test basic functional performance of the MPIC using this gas and the ^{60}Co γ-ray irradiator without activating the chamber. The helium fill gas also served the dual purpose of a flush gas.

4.2.1. MPIC Characteristics Measurements

Chamber capacitance measurement. The multiprobe ionization chamber capacitances were measured by using a capacitance bridge (CIRCUITMATE model PB2000) which enabled direct measurement of the capacitance between the chamber anode and the system ground including all sources of parasite capacitance with an accuracy of ±1 pF. Accurate measurement of the system (chamber + cable) capacitance is crucial for plasma density calculation when the PIC technique is utilized. The capacitance measured between the anode and the ground of the chamber was 40 pF, and that of the cathode to the ground was 56 pF.

MPIC insulation resistance measurements. Electrical insulation resistances between the chamber probes were measured after the baking process was finished. The block-diagram of the test configuration is shown in Figure 4.17. The dotted line in the figure indicates that the ground shields of the cables were not connected to the circuit ground in order to avoid the possibility of measuring cable insulation resistance instead of measuring that of the ceramics. The test results are shown in bar graph form in Figure 4.18. This figure displays the resistance between all the electrical connections comparatively and absolutely. Except for the resistance between the anode and ground, all the resistances between the probes were above $10^{13}\ \Omega$ at room temperature. The low resistance between the anode and ground, which possibly was caused by moisture trapped within the cement bond between the anode and the guard electrode, does not pose a serious leakage current problem since the potential between the two points is near zero (maximum ~ 2 mV; maximum input voltage burden of Keithley-485 picoammeter) due to the presence of the guard electrodes.

MPIC temperature test. The multiprobe ionization chamber, as mentioned earlier, is equipped with its own heating and cooling system. The heating system consists of a heater, thermocouples and a temperature controller. The commercially available heater (cylindrical shape) surrounding

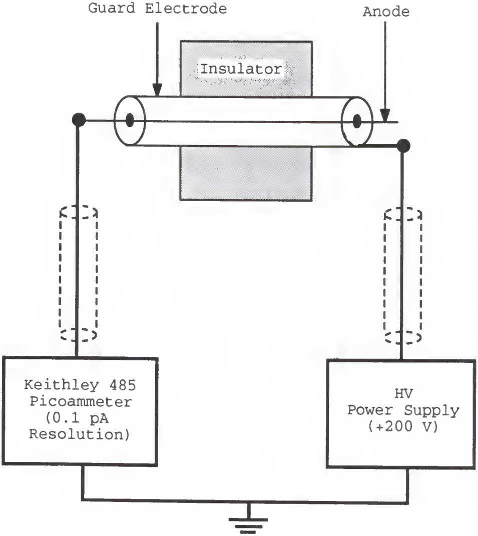

Figure 4.17: Electrical Resistance Measurement between the Probes of MPIC

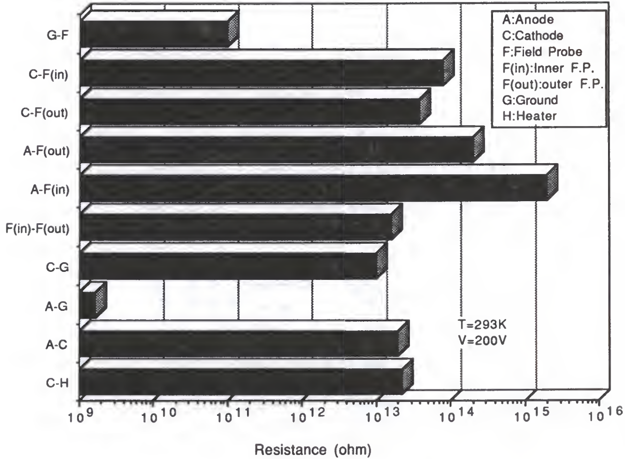

Figure 4.18: Measured Resistance between the Probes of MPIC

the chamber cathode is controlled by a microprocessor-based process controller (OMEGA model CN-9000) to achieve accurate temperature control by using the temperature information provided by the K-type thermocouple inserted into the chamber. The cooling system utilizes deionized water available in the UFTR when the experiment is performed at the UFTR. Test of the heating and cooling system is performed as follows: The chamber is evacuated and maintained under vacuum condition using a pumping station. Then, the water coolant flow rate is measured and is set at the desired rate. The temperature controller set point is set at its maximum (1500 K) preset temperature. Finally the heater is turned on and the temperature is measured at two points; one at the center of the chamber and the other at the hottest spot on the outside of the coolant channel. As shown in Figure 4.19, when the coolant flow is fixed at 5 g/sec, the hottest spot on the outside of the coolant channel is kept below 317 K until the inside chamber temperature reached 1023 K. Even though the heater is rated at temperatures up to 1770 K [43], it is difficult to reach a temperature over 1023 K within a reasonably short time since the cooling water removes the heat so effectively. When the coolant flow rate is reduced to 2.5 g/sec, to allow the chamber inside temperature to increase, the coolant temperature also increased rapidly to above the boiling point. Thus, the heating system is limited to a maximum temperature of 1023 K with cooling water flow rate at 5 g/sec. To go to a higher temperature, the heater

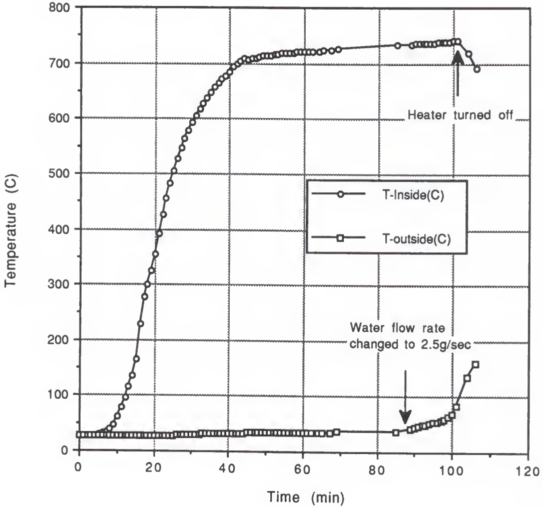

Figure 4.19: Temperature vs Time at inside chamber and at outside wall of coolant tube (coolant flow rate = 5 g/sec)

will have to be provided with a higher current than is possible using the current variac system. The heating time required to reach a particular temperature when the chamber is loaded with gas is longer than the times shown in Figure 4.19, since the thermal conductivity of the gas is higher than that of a vacuum.

Leakage current measurement. The leakage current between the anode and cathode, as a function of chamber temperature, was measured and the results are shown in Fig.4.20. Previously, temperature-dependent PIC measurements were limited by the large leakage current when the commercially available detectors were subjected to high temperatures (~730 K). The multiprobe ionization chamber, which was specifically designed for performing the PIC measurement at higher temperature than commercial detectors, showed a negligible leakage current when the chamber was heated up to 1000 K. Such exceptional performance is attributed to the new electrode/insulation design with guard electrodes and isolation of electrical contact area out of high temperature region. In this figure, one can find the leakage current increases as the temperature of the gas increases. However, up to a temperature of 850 K, the leakage current is negligibly small (less than 1 nA). After 850 K, the leakage current increases rapidly as the temperature increases. At the temperature of 1000 K, the leakage current is ~50 nA, which is large enough to interfere with measurements when the Co-60 source was used as the

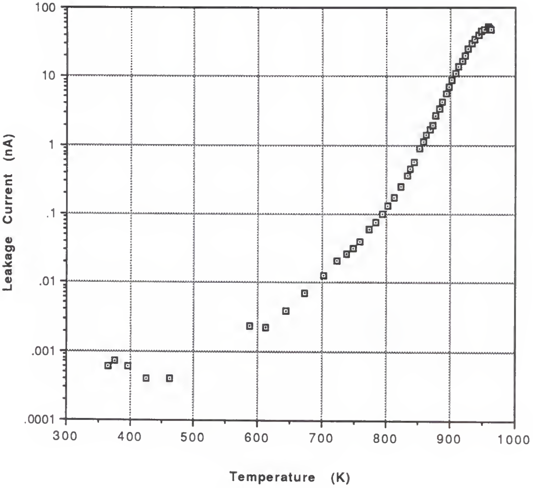

Figure 4.20 : Leakage Current against Temperature Plot

ionization source, but it is still manageably small when the UFTR which can generate a steady-state ionization current of up to 50 μA is utilized as a radiation source. This result shows that one of the main design objectives was accomplished.

4.3. Multiprobe Ionization Chamber Performance Test and Validation

4.3.1. MPIC Test Using Co-60 Irradiator

A 1 atm ^{4}He gas fill and ^{60}Co gamma irradiator were selected for the initial plasma diagnostic test of the MPIC system.

System setup. The PIC system was adjusted to operate with a high voltage pulse width of 10 msec which was selected to assure that sufficient time was allowed for sweeping the chamber free of charged particles that constituted the residual charge from the steady state plasma density. The pulse repetition rate was set at 1 Hz. A collection potential of -400 V was used to ensure rapid collection of the electrons and ions. To test for linearity, gain and zero drift, the system was operated continuously for a week while these functions were monitored. The system's response remained linear and its gain constant within a ±1 % accuracy over the entire period of operation. The PIC system had a minimum voltage measurement resolution of 1 mV.

PIC mode measurement. The MPIC was filled with 1 atmosphere ^{4}He gas and installed inside the ^{60}Co irradiator for its performance test. An operating voltage of 400V was selected by reference to the characteristic curve shown in Figure 4.21 and the PIC voltage and steady state current measurements were performed. The PIC voltage signal pulse profile shown in the Figure 4.22 was acquired by use of a Tektronix 2430A digital oscilloscope and was transferred to a Macintosh microcomputer using the LabVIEW program (see Appendix C). Typical PIC voltage signal performance was observed with respect to peak voltage and pulse rise time, (i.e., electron collection time). The electron collection time was measured to be ~10 μsec at -400 V bias voltage.

A second measurement set was performed with identical chamber setup except with different He gas pressure (0.4 atm). This allowed the pressure dependent characteristics of the MPIC to be observed, as well as providing a comparative check of the 1 atm chamber results. The results of the PIC plasma diagnostic measurements with the MPIC for 1 atm ^{4}He exposed to the gamma field are shown in Figures 4.23 and 4.24. The plot displays a distinctly characteristic first order loss region (slope = 1), as well as an additional region due to second order loss (slope = 1/2). Comparison of this plot with earlier measurements performed with commercial He-filled ion chambers (Figure 3.11) indicates that the MPIC is functioning according to the design objectives for the PIC mode of operation. The electron densities (Figure 4.24)

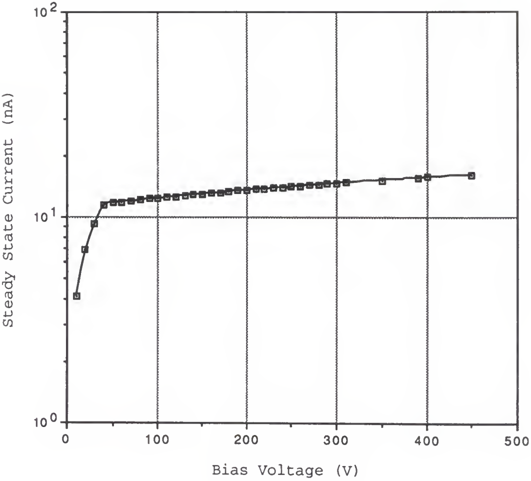

Figure 4.21: Characteristic I-V Curve of the MPIC (1 atm He)

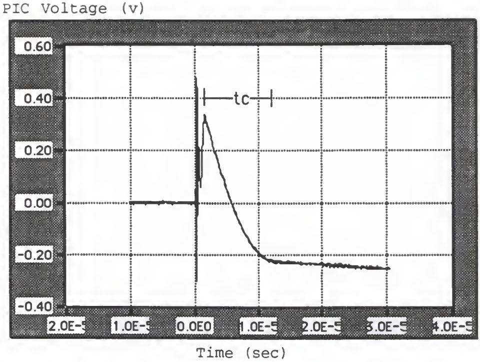

Figure 4.22 : Typical PIC Voltage Signal
From the 1 atm ^{4}He Filled MPIC

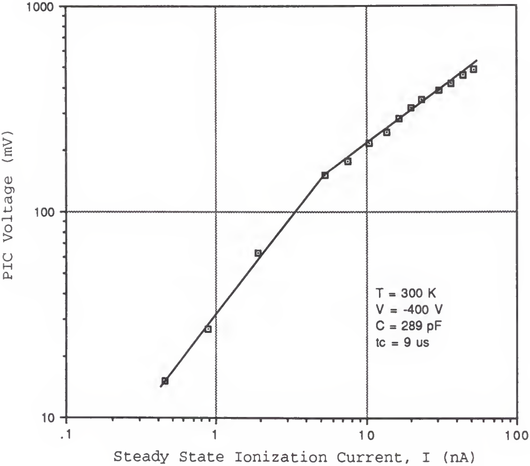

Figure 4.23: PIC Plasma Diagnostic Plot using
Co-60 Source, 1 atm He Filled MPIC

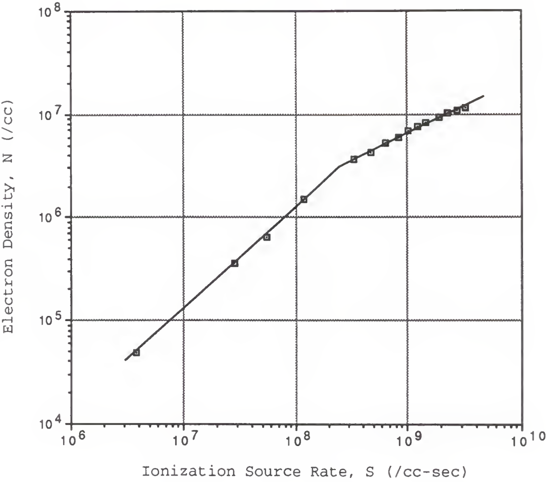

Figure 4.24: Electron Density vs Ionization Source Rate using Co-60 Source, 1 atm He filled MPIC

generated by the ^{60}Co γ-ray source ranged from 5×10^{10} to 1×10^{13} (electrons/m^3) and corresponding electrical conductivities (Figure 4.25) from 5×10^{-9} to 6×10^{-7} (Siemen/m). Displayed in Figure 4.26 is an example of graphical analysis which can be used to solve for the first and second order loss coefficients. As shown in the figure, the coefficients approach their asymptotic limit in an orderly fashion in a well-defined manner which is another indication that the MPIC is functioning according to the design objectives for the PIC mode of operation.

Conductivity and Langmuir probe measurement. When the conductivity probe was applied for measuring the plasma conductivity, it was found that, under the conditions of the measurement, the conductivities were too low for direct observation using the conductivity measurement circuit in use at that time. The minimum detection limit of the conductivity measurement circuit was determined to be approximately 1×10^{-5} (Siemen/m). The limiting value in this instance was due to the low input impedance of the differential amplifier used in the circuit, which is quite common. From earlier descriptions it was noted that the conductivity and Langmuir probes were designed for the measurement of higher density plasmas for which the conventional PIC technique might not be suitable. To avoid interference due to excessive loading of the measurement system, a high impedance buffer was introduced between the plasma probe and the differential amplifier. The buffered

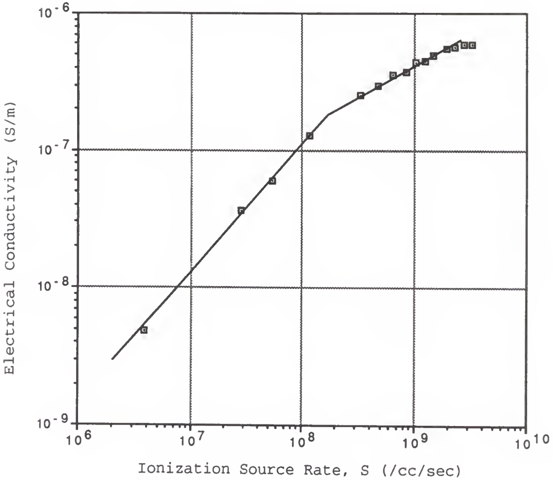

Figure 4.25: Electrical Conductivity vs Ionization Source Rate Using Co-60 Source, 1 atm He Filled MPIC

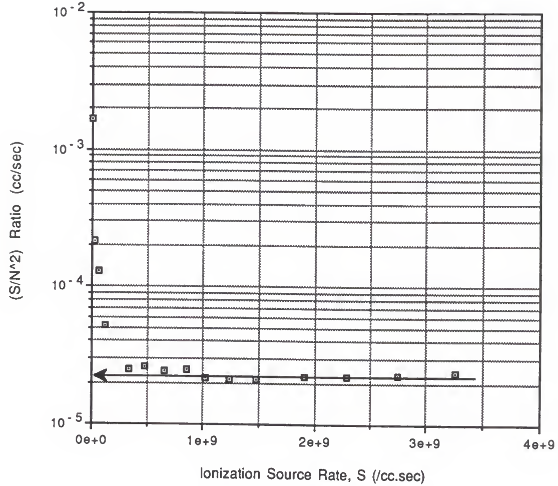

Figure 4.26: 2nd order loss plot, 1 atm He Filled MPIC

measurement system enabled conductivity measurements as low as 10^{-10} (Siemens/m) to be performed; however, capacitance loading could interfere and hinder the low conductivity plasma measurements.

When the conductivity or Langmuir probes were in operation, the MPIC was connected to the time-varying voltage source (triangular voltage wave) through a coaxial cable which has a capacitance of 29 pF/foot (type RG-58). Such capacitive loading on the circuit can induce an unwanted current to flow through the circuit even in the absence of a plasma within the chamber. The level of this capacitively induced current flowing through the circuit is given by the expression;

$$I = C\frac{dV}{dt} = 2CfV_{p-p} \qquad (4.19)$$

where, C is the system capacitance, f is frequency of time-varying voltage source and V_{p-p} is peak-to-peak height of the voltage source. For example, with the lowest frequency of the function generator selected at 2.5 Hz and a 10V V_{p-p} wave, the slew rate is (10V/0.2sec =) 50 V/sec. A typical capacitance for the system used in the ^{60}Co irradiator setup was 200 pF. Then the capacitive current induced by the loading would be 10 nA. This level of current would be large enough to interfere with the measurements of conductivity and with the measurements of Langmuir probe when the ^{60}Co source was used as the plasma generation source (The maximum ionization current generated was ~40 nA as shown in

Fig.4.23). In order to minimize capacitive current interference, one has to reduce either the frequency of the voltage wave or the height of V_{p-p}, since the system capacitance is already fixed.

4.3.2. MPIC Test Using the UFTR

System setup. The MPIC was filled with mixture of ^{3}He and ^{4}He gas to test the chamber performance under high density plasmas generated by ^{3}He(n,p)T reaction. The ^{3}He gas was obtained from the Los Alamos National Laboratory. Filling the MPIC with ^{3}He gas was accomplished by use of the following procedures: The MPIC was connected to a ^{3}He gas supply bottle through a liquid helium cold trap (see Fig.4.27). After the MPIC was evacuated to 1 x 10^{-6} torr using a pumping station, the ^{3}He gas was admitted slowly into the MPIC through the liquid helium cold trap. Thus, even trace amounts of impurity gases, other than ^{3}He, were condensed out in the trap and not allowed to pass into the multiprobe ionization chamber.

The experimental assembly which consisted of the multiprobe ionization chamber and a protective chamber housing as shown in Figure 4.28, was inserted into the thermal column of the UFTR and adequate shielding was provided to reduce radiation streaming from the thermal column (Figure 4.4). Once the system was tested for proper operation, the reactor was brought up to power and was set at

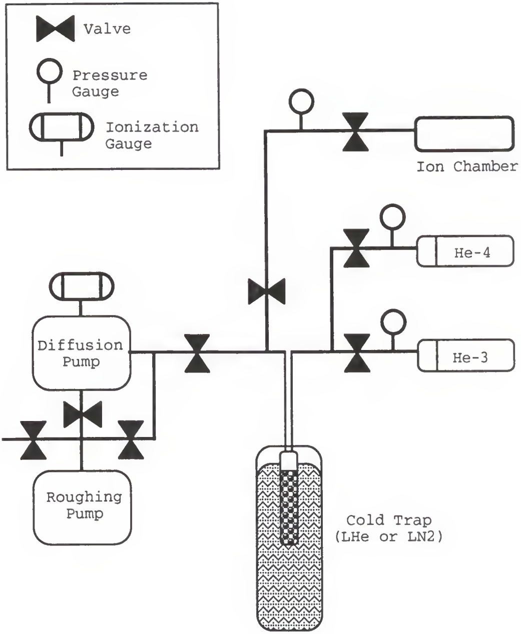

Figure 4.27 : Gas Handling System

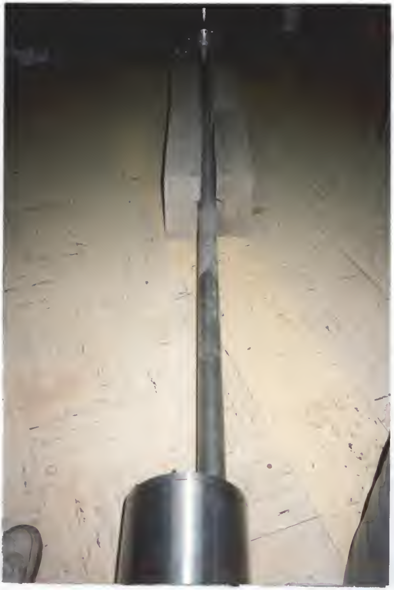

Figure 4.28: A Photograph of the MPIC Experimental Assembly

a low level (~ 1 watt) at which a minimum observable PIC voltage signal was generated. At this fixed level of reactor power and temperature (300 K), the system operational modes were exercised, i.e., the steady state current, PIC voltage, Langmuir and conductivity probe measurements were performed sequentially by use of the automated MPIC computer controlled operation system. Each data set (or parameters) obtained with the different modes of measurement was analyzed and stored in the computer for later retrieval and further analysis. The reactor power was then raised to a higher level and the measurements were repeated. This procedure was continued until the reactor power had been raised to the 30 KW level.

PIC probe measurement. Typical of the results obtained with the PIC voltage measurements are those shown in Figure 4.29 where the PIC voltage is plotted as a function of reactor power. It is seen that the PIC voltage increases with reactor power. Initially and up to a reactor power of 1 KW, the PIC voltage, which is proportional to electron density, follows the reactor power with a slope of 1/2 on a log-log scaled graph, as predicted by theory. Above 1 KW, however, the PIC voltage is seen to deviate from the above trend and to follow a new slope that is somewhat less (~1/4). Possible explanations for this behavior are (1) that electrons generated by nuclear ionization are experiencing an enhanced loss rate due to increased recombination or the initiation of other loss mechanisms above a certain level or

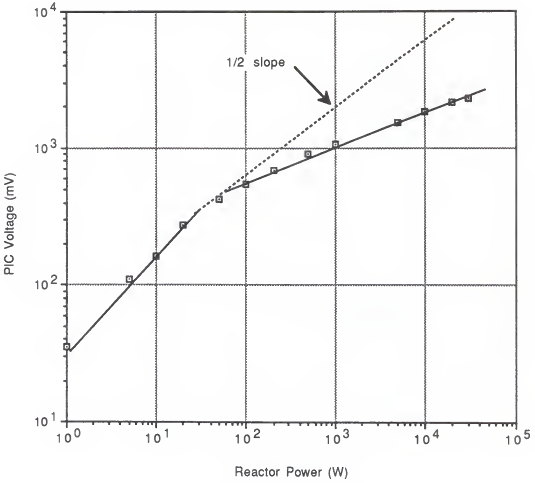

Figure 4.29 : PIC Diagnostic Plot Using UFTR, 16.7 psi He (3.5% He-3) Filled MPIC

(2) electron attachment to neutral atoms or molecules which had been presumed not to be present are removing electrons from active participation and replacing them with negative ions, determining the electron signal voltage component. Previous experience with high purity helium gas measurements has shown that within the plasma source generation rate range of this experiment (Figure 4.30) the electron density follows the typical slope of 1/2. Thus, the former assumption of an enhanced recombinational loss rate is ruled out as an explanation. For the latter explanation, the source of impurity atoms or molecules, if any, must be addressed. One possible source of impurities is outgassing from the surface of the materials which are located within the gas fill volume of the chamber. Such impurities have been found to be removed from surfaces by the bombardment of high energy charged particles, neutrons and γ-rays as the reactor power and/or radiation field intensities increase. Another source of impurities could be due to an air leak which could allow molecular species such as oxygen, nitrogen and water vapor to enter the chamber by diffusion through cracks and pores with their concentration increasing with storage time. The PIC theory presented in CHAPTER 3 is based on the assumption that the ion pairs generated by charged particles are composed of only electrons and positive ions, whose number densities are equal. When negative ions co-exist with electrons and positive ions, the theory as stated must be modified to include the effects caused by the presence of the negative

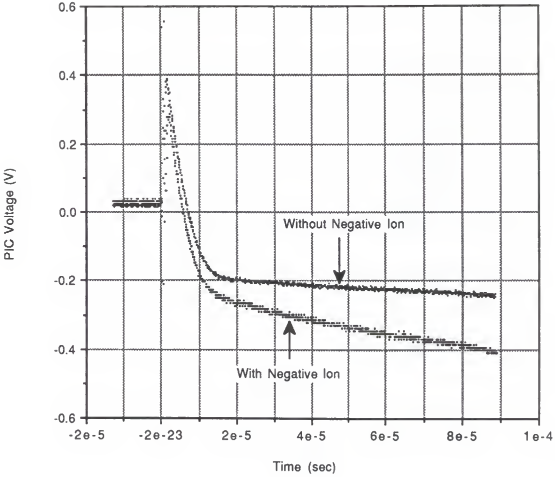

Figure 4.30 : PIC Signal Voltage Profiles
with & without Negative Ion Presence

ions. In equation 3.1, the PIC voltage measured at the electron collection time is related to the electron density only through the geometrical factors.

$$v(t_c) = -\left[\frac{N_s eU}{C}\right]\left[1 - \frac{1}{2\ln(b/a)}\right] \qquad (3.1)$$

The factor {1-1/(2ln(b/a)} occurs due to the assumption of an unaltered positive ion distribution, which is assumed to remain approximately constant during the collection of electrons. However, the formula relating the PIC voltage to the electron density is not affected by the presence of the negative ions since the electron mobility is far greater than that of either the negative or positive ion. In this case, however, the electron number density is no longer equal to the positive and negative ion densities. Only the summed effects of the densities of both positive and negative ions can be observed for the PIC signal at the time of ion collection ($t_e << t_i,t_n$). From the time characteristics of the two PIC signal voltage profiles shown in Figure 4.30, one can directly observe the difference of ion collection rated or slopes with and without negative ions. The time profile where negative ions are known to be present, shows an added slope due to the motion of both negative and positive ions. The presence of negative ions was also confirmed by the Langmuir probe measurements which are to be discussed later. The electron density, then, with the electron collection time, used to calculate electrical conductivity (Eq. 3.17) and the results are shown in Figure 4.31.

Conductivity probe measurement. The electrical conductivity of the plasma was measured directly using conductivity probes. The two conductivity probes were located in between the cathode and the anode of the multiprobe ionization chamber (MPIC). The conductivity of plasma was measured by applying a triangular voltage to the cathode and recording any voltage drop between the two probes and the current flow measured at the anode at the same time. The results of the measurements are summarized in Figure 4.32. The electrical conductivities were deduced from the slope of the curve and geometrical factor as shown in Equation (4.10). Electrical conductivities which were measured directly using the conductivity probe are plotted as function of reactor power in Figure 4.33. Also plotted are the results calculated with the information (voltage and collection time) measured by PIC probe. Both results are in good agreement with each other except for the low conductivity region where the conductivity probe was subject to large error due to the capacitive loading effect.

Langmuir probe measurement. The Langmuir probe system was operated in the "single probe" mode. Plasma characteristics were measured by applying a triangular voltage wave to the probe and monitoring the corresponding current flow. The current was measured by observing the voltage drop across a resistor whose value was well known.

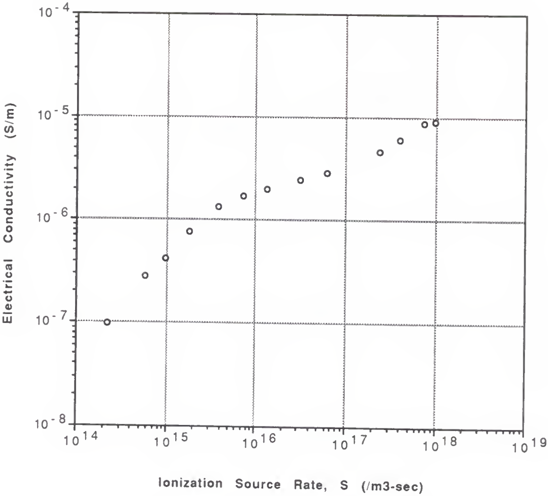

Figure 4.31: Electrical Conductivity vs Ionization Source Rate, 16.7 psi He(3.5% He-3) Filled MPIC

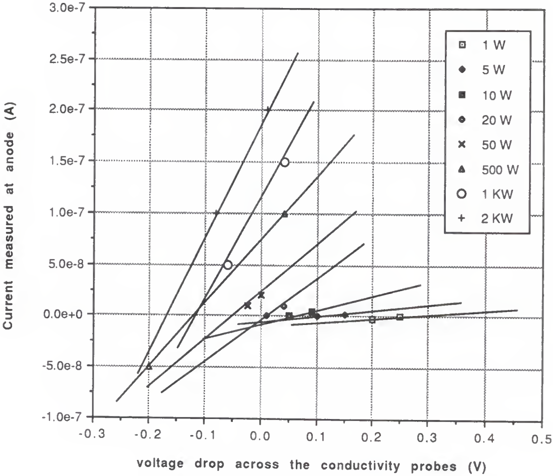

Figure 4.32 : Conductivity Probe Measurement Results
at Varying Reactor Power
(16.7 psi He-filled MPIC, 3.5% He-3)

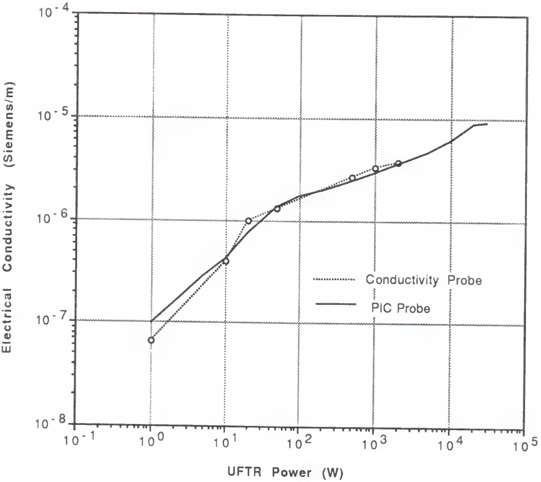

Figure 4.33 : Electical conductivity measured by Conductivity Probe, 16.7 psi He(3.5% He-3) Filled MPIC

The probe which was cylindrical in shape and one inch long, had a diameter of 0.03125 inch. The characteristic curves obtained are shown in Figure 4.34. The curves show the typical Langmuir probe I-V curve characteristic. Through the analysis of such curves several useful parameters can be deduced. Electron temperatures of ~4,000 K and electron density ranges between 1×10^{11} [/m^3] and 1×10^{13} [/m^3] were measured. The electron temperature was much higher than that of ions and neutral atoms (~300 K) in the gas. Since collision exchange of kinetic energy between electrons and heavy particles in a slowing down medium is highly inefficient, the electron temperature is considerably higher than the ion temperature.

Comparing the results obtained here with those obtained with earlier PIC measurements, indicates that some of the electrons generated by nuclear ionization were lost by electron attachment to impurity atoms or molecules, thereby reducing electron number density.

Wu et al. [11] established a probe theory for the presence of negative ions. In the absence of negative ions,

$$n_e = n_i \qquad (4.20)$$

Since the saturation current is proportional to the charged particle number density through a relationship, we have electron and ion saturation currents as follows:

$$I_e = (An_e e\sqrt{\frac{kT_e}{2\pi m_e}}), \qquad (4.21)$$

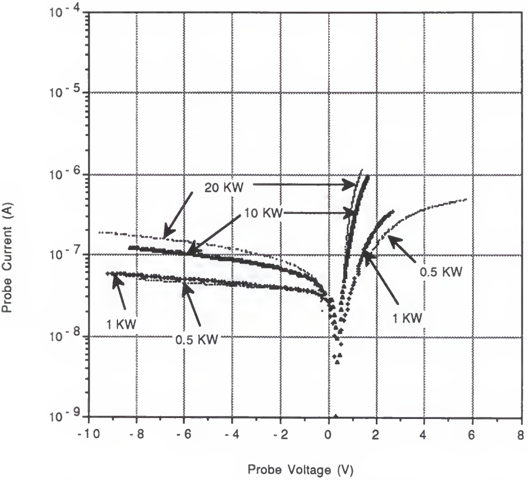

Figure 4.34: Langmuir Probe Characteristics Curves Obtained at Different Reactor Power (negative currents are converted to positive for display purpose)

$$I_i = (An_i e\sqrt{\frac{kT_i}{2\pi m_i}}) \qquad (4.22)$$

Thus the ratio of the electron saturation current and the ion saturation current is expressed as;

$$\frac{I_e}{I_i} = \sqrt{\frac{m_i T_e}{m_e T_i}} \qquad (4.23)$$

and for T_e = 4000 K and T_i = 300 K, the ratio $\frac{I_e}{I_i}$ is ~ 300. However in the result shown in the Figure 4.34, for example for the 10 KW data set, the ratio is only 180. Therefore this result strongly supports the presence of negative ions.

When negative ions are present, the current drawn from the probe, when the probe was biased strongly positive, is the sum of both electrons and negative ions.

$$n_e + n_n = n_i \qquad (4.24)$$

One can determine positive ion density, n_i, through the measurement of positive ion saturation current. Also from the electron saturation and negative ion saturation current one can determine values of the electron density. Since the magnitude of negative ion current is often so small due to its larger mass and lower temperature (Equation 4.22) versus the electron, it can be safely calculated from Equation (4.24).

4.3.3. Discussion

The principal goals for the multiprobe ionization chamber plasma diagnostic system, which was designed and constructed for the study of nuclear-generated plasmas, has been accomplished. The system's proven capability includes computerized control of the overall measurement system and on-line data acquisition and analysis, by use of the IEEE-488 (GPIB) bus control, and data transfer protocols, with a Macintosh series microcomputer. Basic chamber characteristics studies show that the system does not suffer from excessive leakage current problems even up to temperature of 1000 K. Performance testing of the system using the ^{60}Co irradiator, which generates a low density plasma (maximum electron density; ~ 1 x 10^{13} #/m^3) in the 1 atm helium filled MPIC, showed that the chamber functions according to design when operated in the PIC mode. This was demonstrated by comparison of its performance with the results of earlier measurements. The conductivity and Langmuir features are also shown to be functioning properly over their low density ranges with high impedance buffers. Measurements into higher density regimes, using ^{3}He(n,p)T ionization sources in the UFTR, showed the system's overall plasma diagnostic capability. Responses of the three measurement features exhibited regions of overlap under these conditions as expected. The three independent types of probe developed to compensate each other have proven to be quite useful in determining a variety of plasma characteristics and cross checking their performance under identical plasma conditions. The conductivity and Langmuir probes have an upper measurement range of 1 [S/m] and electron density of

10^{18} [$/m^3$]. Therefore, these new features added to the original PIC measurement capability enhance the overall systems capability.

Experience gained during the multiprobe ionization chamber manufacturing and operational testing suggests several areas for improvement. The multiprobe ionization chamber suffered gas contamination problems when gas was sealed over an extended period of time (several days for subatmospheric pressure and about a month for over atmospheric pressure). The main reason for this apparent leakage is due to the chamber not being completely vacuum tight due to tiny cracks that developed during the welding process for the electrical feedthroughs. This factor is the main reason for the current chamber not being tested under high pressure conditions. Another possible reason for the gas contamination is outgassing from the materials located inside the chamber. The heater element was located within the chamber volume due to restrictions imposed on the size of chamber set by the UFTR thermal column space, while still maintaining a reasonably large effective chamber volume.

Limitation of the sensitivity of the Langmuir and conductivity probes stemmed from the capacitive loading. In order to reduce the capacitance loading, which is mainly due to the long signal cables extending out from the reactor core, one can think of installing electronic circuits close to the chamber with appropriate radiation shielding. In this case checking or repairing the circuits during the operation would be impossible. However, the circuits are sensitive enough to measure most plasma conditions which was designed to measure.

CHAPTER 5
CONCLUSION

This dissertation research led to the development of new, multiple-faceted plasma diagnostic system which, in particular, can be used to measure certain critical parameters of gas core reactor/MHD converter systems Initially, it was thought that the pulsed ionization chamber (PIC) technique alone, with its multi-parameter measurement capability, could meet the requirements since its measurement environment more closely simulated the gas core reactor system than any of the other method available. As a preliminary study, a new PIC system based on state-of-the-art electronics was developed and applied to various gases including candidate fuel gas, He(UF_6) to demonstrate its capability to study nuclear-generated plasma kinetics as proof-of-principle experiments.

The parameters measured include plasma generation rate, plasma density, electron/ion mobility, plasma loss coefficients and electrical conductivity. The recombination loss results obtained with the high purity rare gases (He, Ar, Xe), ionized with gamma rays, fission fragments and the ^{3}He(n,p)T reaction products, have in general followed trends predicted by theory, following a $T^{-9/2}$ dependence above 600 K. Enhanced columnar recombination effects in fission fragment generated plasmas have been observed for both helium and argon, indicating that ~70% of the ionization produced along a fission track for 10 atm He and 1 atm Ar would be lost during the early stages of track expansion and would not be available for plasma buildup. Plasma loss coefficients for gases comprised of molecular components, in general, have been observed to exhibit a $T^{-3/2}$ temperature dependence, but at a higher pressure and for electronegative species such as UF_6, evidence of cluster formation has been observed with an approximate T^{-4} plasma loss temperature dependence.

Electron and ion mobilities and, thus, electrical conductivities, have also been determined. The measured conductivities of He(UF_6) gases at the experimental conditions (maximum 730 K) are not high enough for the gas to be used as a fuel and working gas of a GCR/MHD system mainly due to the high electron affinity, and subsequently forming negative ions, of the fluorine containing gas. However, further experiments at high temperature must be carried out before a conclusion on the usefulness of UF_6 as a fuel gas of the gas core reactor system can be drawn. A possible alternative combination for the fuel and working fluid might be UF_4 with KF as a seed and fluorine scavenging gas to prevent or reduce electron attachments process in the fissioning fuel gas. However, this combination could also suffer from columnar recombination losses due to fission fragment ionization. Exploration of the possibility of developing this type of reactor would require, as a necessity, the addressing of the difficulties associated with vaporization and recovery of metallic uranium. Another factor which must also be considered in evaluating practical gas media for application in nuclear/MHD power generation systems is that the working media not only must have sufficiently high electrical conductivity throughout the power generation cycle, but also, from an engineering standpoint, they must be procurable without requiring extensive care in handling and without necessitating an ultra bake-out of its containment system, since contamination of the gas by impurity gas will reduce the conductivity of the gas substantially.

From the equilibrium-type measurements presented in this study, it can be concluded that the PIC technique for plasma diagnostic is an effective and significant tool for characterizing the kinetics of plasmas particularly in high pressure gases. The close agreement of the results of these measurements with the findings of other investigators demonstrates that the PIC technique is a valid approach. The only limitation of applying the PIC technique to the study of high temperature ionized gas (plasma) arises from the inappropriate characteristics of commercially available ionization chambers under high temperature operation.

The subsequent development and implementation of a computerized multiprobe ionization chamber (MPIC) plasma diagnostic system, which is basically a combination of the PIC, conductivity and Langmuir probes, improved the performance of the PIC technique by extending the working temperature higher than the commercial chambers can tolerate, and also provided the means to extend the measurement range and parameters. The design and building of the computer controlled MPIC plasma diagnostic system took considerable time and effort, but the end result was success.

The principal goals for demonstration of the multiprobe ionization chamber plasma diagnostic system have been accomplished. Performance testing of the new system using the ^{60}Co source and the UFTR shows that the chamber is functioning according to design for the PIC mode, as demonstrated by comparison of its performance with those of earlier measurements. The conductivity and Langmuir features have also been shown to be functioning properly over their low-density ranges with the help of the high impedance buffer. Measurements using ^{3}He(n,p)T ionization source performed in the UFTR, in order to test the system's overall plasma diagnostic capability show the response of the three measurement features exhibit regions of overlap under high plasma density condition. The chamber was not able to be tested under high pressure and high temperature conditions to meet the ultimate design goal due to a leak problem occurred during manufacturing process. However, the measurement of temperature test shows that the chamber does not suffer the excessive leakage current problem up to 1000 K, which validates the design concept. Another positive feature obtained from the new guard electrode design is better definition of the effective volume of the chamber since it reduces end-effect significantly. The system's proven capability includes computerized control of the overall measurement system and on-line data acquisition and analysis, by use of the IEEE-488 (GPIB) bus control, and data transfer protocols, with Macintosh series microcomputers. The technique developed for the remote switching between the GPIB instruments can also be used for sequencing and switching up to 16 GPIB instruments without using a microprocessor, which is useful for small-scale lab automation.

In conclusion, the PIC-based multiprobe ionization chamber concept has been proven to be useful as a nuclear-generated plasma diagnostic tool, particularly for the high pressure gases to be encountered in the study of gas core reactor/MHD converter systems. With development of a better chamber by addressing the problems experienced during the manufacturing processes, the multiprobe ionization chamber should be well suited for high temperature and high pressure applications. Another field this system can be applied is in the study and development of Langmuir probe theory in high pressure gas system.

APPENDIX A
PIC SYSTEM ELECTRONICS

1. PIC Electronic Circuit

1.1. System Block diagram

A block diagram of the PIC system is presented in Figure A.1. The electronic parts of the PIC system essentially consist of three main components: 1) the pulse generator, 2) the high voltage pulser, and 3) the signal detector.

The pulse generator provides TTL pulses whose period and width are controlled by thumbwheel switches mounted on the front panel with ranges from 1 msec to 10 sec and 1 μsec to 10 msec, respectively.

The high voltage pulser converts the TTL level pulses, which are derived from the pulse generator, into high voltage pulses by using a high speed MOSFET operated as a switching device. To accommodate high speed switching requirement for the high voltage pulses, a N-channel MOSFET has been used for negative voltage switching by use of a ground separation technique. For this purpose, an extra ground isolated power supply has been used. With this high voltage pulser, rise time as fast as 30 nsec has been obtained under a capacitive

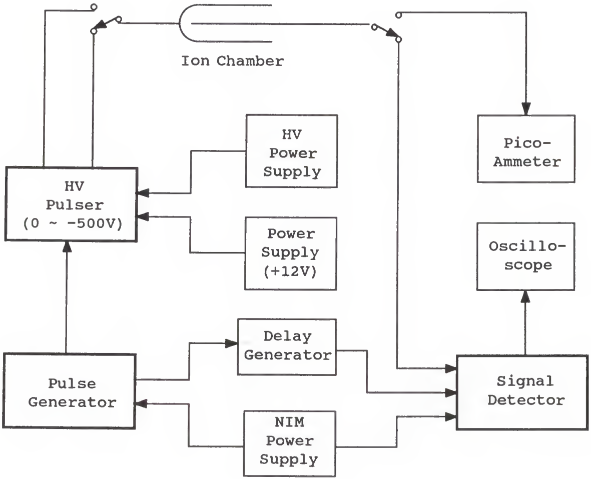

Figure A.1: Block Diagram of PIC System

load of approximately 400 pF for high voltage pulses of up to 500 volts.

The signal detector consists mainly of impedance switching circuits, capacitance compensation circuit, and a buffer amplifier. The heart of the signal detector is the impedance switching. Using a fast PNP type bipolar transistor with an f_t of 150 MHz has allowed the fast switching speed requirement of this circuit to be met with a rise time of approximately 50 nsec. A special technique has been used to compensate for the effect of the switching transistor capacitance and so, to linearize the base line of signal. An FET input operational amplifier, which has an extremely high input impedance of 10^{14} Ω, has been used to provide the signal to the oscilloscope without disturbing the measurement system.

1.2. Pulse Generator

The circuit of the pulse generator and its operational timing diagram are presented in Figure A.2 and Figure A.3, respectively.

The crystal oscillator (IC-1) generates 1 MHz TTL level pulses and sends them to ÷10 (divided by 10) counter (IC-2) or to ÷1000 counters (IC-3,4,5) according to the selection of the switch (SW-1). The switch (SW-1) selects the ranges of the output pulse parameters; pulse period of from 1 msec to 999 msec or from 10 msec to 9.99 sec, and pulse width of from

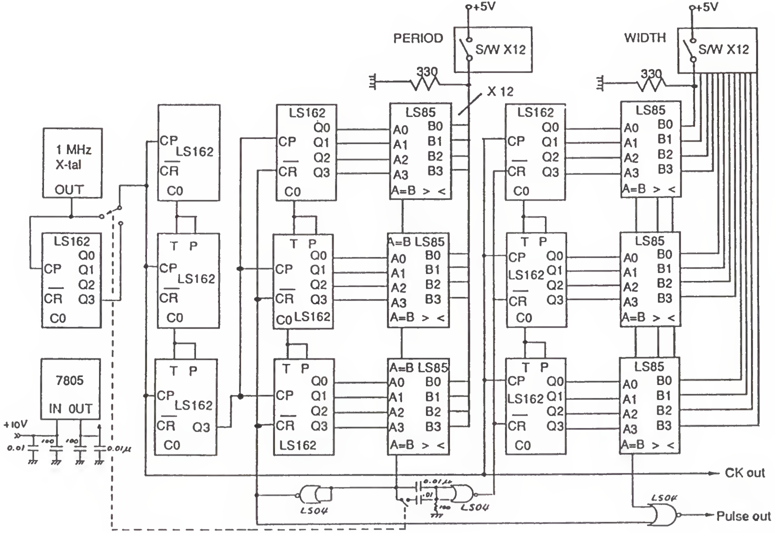

Figure A.2 : Electronic Circuit Diagram for the PIC System

(Pulse Generator and Timing Circuit)

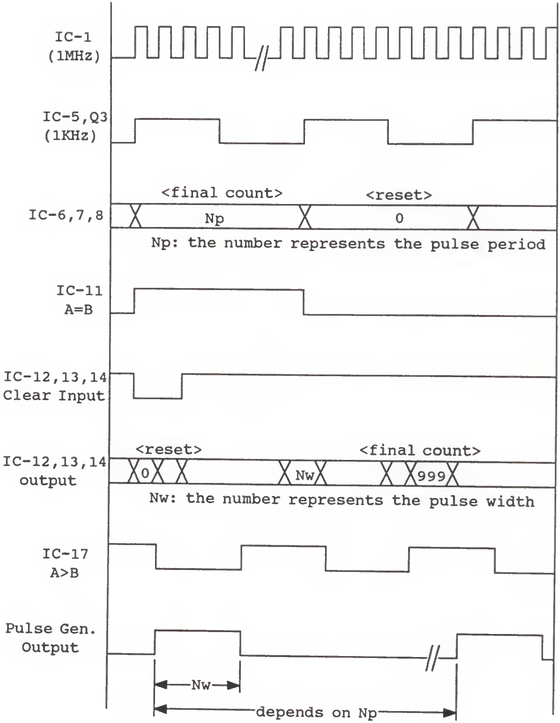

Figure A.3: Timing Diagram for the Pulse Generator

1 μsec to 999 μsec or from 10 μsec to 9.99 msec. Former settings will be designated as Mode-1 of SW-1, and latter settings as Mode-2.

Assume that the Mode-1 has been selected as denoted in the circuit diagram, then, the output pulses of ÷1000 counters (Q3 of IC-5) has the frequency of 1KHz. These pulses are provided to programmable counters (IC-6,7,8) whose counting number is determined by the comparators (IC-9, 10,11). These comparators receive the binary number (N_p in Figure A.3) to be compared from the thumbwheel switch (TSW-1). This means that the TSW-1, in effect, determines the period of the output pulses.

The output of the comparator (A=B pin of IC-11) is sent to the clear inputs of the programmable counters (IC-6,7,8) via a NOT gate, and to another set of programmable counters (IC-12,13, 14) via a differential circuit preceded by a NOT gate, respectively. The time constant of the differential circuit is changed according to the selection of the switch (SW-2) by a factor of 10. The two switches (SW-1,2) change their states simultaneously. The state of the switch SW-2 in the circuit diagram also denotes the Mode-1 operation.

The programmable counters (IC-12,13,14) which receive clock pulses from the crystal oscillator (IC-1) are cleared by the NOT gated output of the comparators (IC-9,10,11). This allows that the two programmable counters for determining the pulse period and the pulse width start counting at the same time. The timing diagram shows this relationship between the two counters. The output of the programmable counters (IC-12,13,14) is compared with predefined binary number (N_w in Figure A.3) which is provided by the thumbwheel switch (TSW-2). The output of the comparator (IC-14) sustains high value during the period when the outputs of the programmable counters (IC-12,13,14) are less than those of the thumbwheel switch (TSW-2). By combining the NOT gated output of the comparator (IC-17) with the clear input of the programmable counters (IC-6,7,8) in a NOR gate, pulses whose period and width can be controlled by the thumbwheel switches (TSW-1,2) are eventually obtained at the output of the NOR gate. These pulses are transmitted to the high voltage pulser and the impedance switching circuit.

1.3. High Voltage Pulser

The circuit diagram of the high voltage pulser and its operational timing diagram are presented in Figure A.4 and Figure A.5, respectively.

The pulses which is provided from the pulse generator passes two NOT gate (IC-20) to be delayed with respect to the delay generator trigger signal. This signal triggers the delay generator which provides delayed pulses to the impedance switching circuit. The output of NOT gate may have some jitters because of the high voltage switching section in next stage. The corrupted signal is cleaned up at the Delay Flip-Flop (D-FF,IC-21) by retiming with the clock signal.

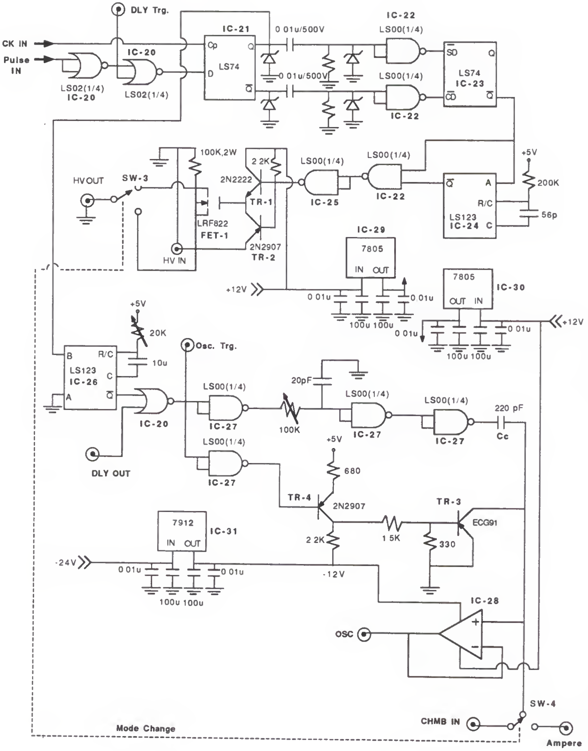

Figure A.4: Electronic Circuit Diagram for the PIC system (HV Pulser and HI Switching Circuit)

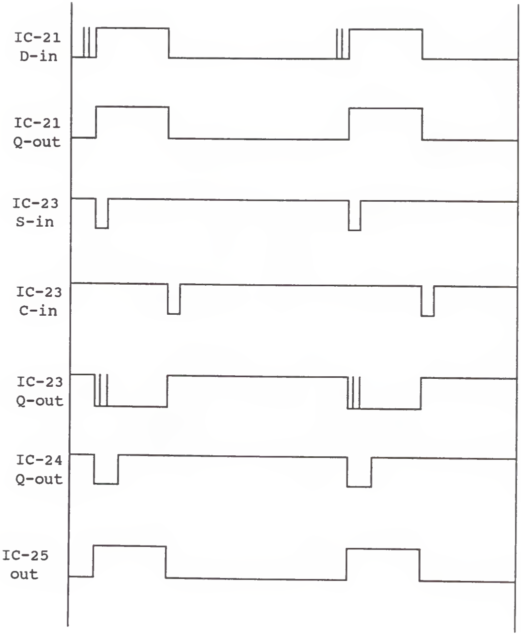

Figure A.5: Timing Diagram for the High Voltage Pulser

The zener diodes (D-1,2) at the outputs of the D-FF (IC-21) are used to protect the circuit against the surge voltage which is induced when the high voltage MOSFET (FET-1) turns on or off. The high voltage capacitors (HC-1,2) block the DC current between the pulse generator and the high voltage pulser and constitute the differential circuit with the resistors at the input of the NOT gate (IC-22). The two ends of the high voltage capacitors have different ground voltage. This is the reason why different symbols are used to denote the each ground point. Two other zener diodes are used at the other sides of the high voltage capacitors with the same reason described above. When the pulses which are sent from the pulse generator pass through the differential circuit, only rising and falling edges are preserved. The D-FF (IC-23) recovers the original pulses by making use of the edge signals. The recovered signal goes to the monostable multivibrator (IC-24) to be cleaned up. The timing diagram shown in Figure A.5 explains by itself details about this process.

The open collector NOT gate (IC-25) drives the complementary transistor circuit and eventually the high voltage MOSFET (FET-1). The NPN transistor (TR-1) rapidly supplies the charging current to the parasitic capacitor at the gate of the MOSFET and the PNP transistor (TR-2) rapidly draws out the discharging current from the capacitor. In conjunction with the high speed switching capability of the MOSFET, this complementary transistor circuit makes the strict design condition about switching speed easy to resolve.

The operation of the MOSFET is illustrated in Figure A.6. When the MOSFET turns on, the charging path is from the high voltage source to the load capacitance (C) through the turn on resistance (r) of the MOSFET whose value is quite low (2 ~ 5 Ω). The time constant of this loop is given by rC which is approximately 400 pF x (2 ~ 5 Ω) = 0.8 ~ 2 nsec for typical cable and chamber combinations. Meanwhile, the time constant of the discharging path is given by RC. Fortunately, because there is no strict requirement on the turn off time, one can choose the value of R arbitrarily large, approximately 100 KΩ or above. The large value of R results in very low steady state current through the MOSFET and eventually, highly stable operation of the MOSFET.

1.4. Signal Detector

1.4.1 Impedance switching signal generator

Basically, the impedance switching signal is generated by two delay circuits. One is for very accurate and stable adjustment of the time delay (TD-1) and the other is for coarse adjustment of the time delay (TD-2), as shown in Figure A.7.

The time delay (TD-1) is adjusted by the commercial delay generator to guarantee stable operation. However, the other time delay (TD-2) is adjusted by simple delay circuit

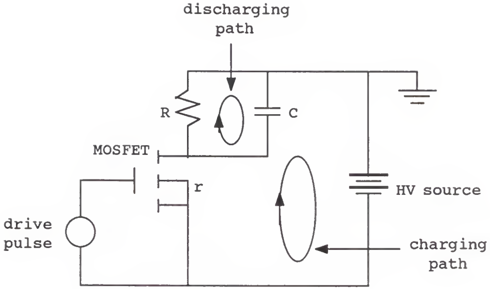

Figure A.6: MOSFET Switching

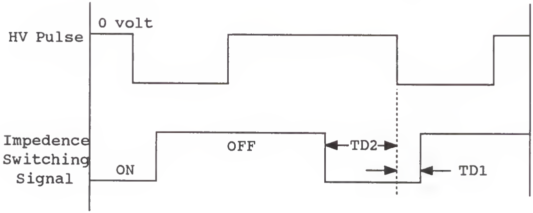

Figure A.7: Timing Relationship between the High Voltage Pulse and the Impedence Switching Signal

using a 74LS123 monostable multivibrator. The monostable multivibrator (IC-26) is derived by the output of the D-FF (IC-21). The delay time is determined by the setting of a potentiometer (P-1) which is mounted on the front panel. The output of the monostable multivibrator (IC-26) is combined with the delay generator output at the NOR gate (IC-20). The output of the NOR gate is final impedance switching signal. The operational timing diagram of the impedance switching signal generator is presented in Figure A.8. Also, the impedance switching signal is used as an external trigger signal of the oscilloscope.

1.4.2.Impedance switching & capacitance compensation circuit

The impedance switching circuit consists of the NOT gate (IC-27) and transistors (TR-3,4). The transistor (TR-3) changes the level of the impedance switching signal from that of TTL to from 0 to -12 volts level to derive the other PNP transistor (TR-4). The latter transistor (TR-4) performs the switching operation. To meet the switching speed requirement, a transistor which has high unit gain bandwidth has been used. The need for the capacitance compensation circuit is explained as follows with the help of Figures A.9 and A.10.

Without the compensation circuit, when the transistor (TR-4) turns off under zero ionization source condition, the waveform at the collector of the transistor (TR-4) would look like that shown in Figure A.10.

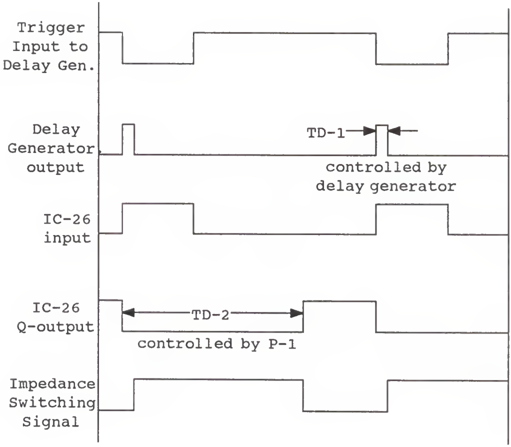
Trigger Input to Delay Gen.
Delay Generator output
TD-1
controlled by delay generator
IC-26 input
IC-26 Q-output
TD-2
controlled by P-1
Impedance Switching Signal

Figure A.8: Timing Diagram for the Impedance Switching Signal Generator

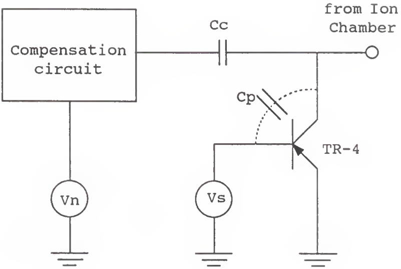

Figure A.9: Impedance switching transistor and capacitance compensation circuit

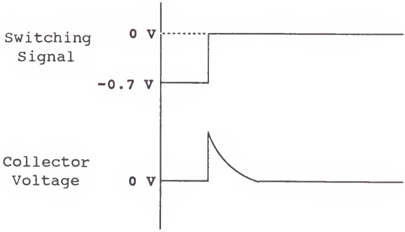

Figure A.10: Waveform at the collector of transistor (TR-4) without compensation

This transient response of the collector voltage occurs because of the parasitic capacitance between the collector and the base of the transistor (TR-4) which is explained as follows. At the leading edge or rise of switching signal, the collector voltage of the transistor (TR-4) instantaneously follows the base voltage with some small fraction of attenuation, but subsequently, it exponentially decays to the baseline with a long time constant, since the transistor (TR-4) is now in an OFF state with no appreciable flow of current. This transient response under zero ionization source conditions remains unchanged under normal measurement conditions and can cause erroneous results by inducing displacement of the baseline. Such a undesirable shift of the baseline due to capacitance coupling can be and has been compensated by the use of an added capacitor (C_c) and a compensation signal of opposite polarity (V_n in Figure A.9) in phase with respect to the impedance switching signal. When the compensating signal (V_n) is transmitted through the coupling capacitor (C_c), it results in negative going transient response at the collector of the transistor (TR-4), if the circuit is adjusted appropriately. The compensation component influences the impedance switching circuit only during the transient period. Even though a complete compensation circuit has not been accomplished, in removing the transient response, practically useful performance has been observed.

The compensation circuit, shown in part of Figure A.4, is composed of the NOT gate (IC-27), a potentiometer (P-2), which is used to adjust the delay time of the compensation signal, two other NOT gates (IC-27), and the compensation capacitor (C_c).

1.4.3. Buffer amplifier

A high input impedance operational amplifier (IC-28) is used as a buffer amplifier. The amplifier (IC-28) has FET inputs and provides almost interference free measurement of the signal obtained at the collector of the transistor (TR-4). A potentiometer (P-3) is used to adjust DC offset in the output of the operational amplifier.

2. PIC System Operation Manual

2.1. Installation

The PIC system should be connected as illustrated in Figure A.11. To make proper and safe operation of the system, compliance with the following precaution must be assured.

A. The ground of the power supply which provides +12 volts must be separated from the overall system ground. Usually, the system ground is connected to the earth ground through power cables. Ground separation of a typical power supply can be achieved by simply leaving the GROUND terminal of the power supply alone. Do not connect the terminal to either -V nor +V terminal.

B. Make sure that the polarity of the high voltage power supply is selected to be negative.

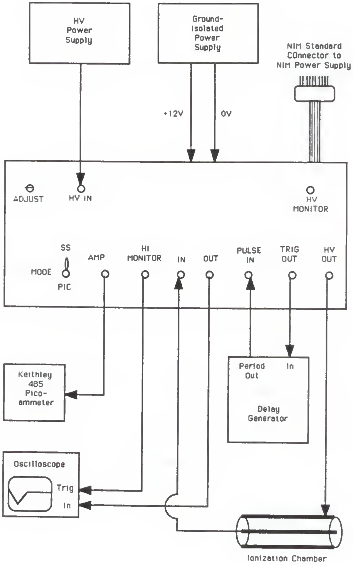

Figure A11: Installation of the PIC system

C. Polarity selection switch on the front panel of the delay generator must be set to negative.

D. The period output terminal of the delay generator must be used to connect the delay generator to the PIC system. Do not use the routing or fast output terminal.

2.2. Operational Procedures

A. Install the PIC system as shown in Figure A.11. Keep in mind the cautions mentioned in section 2.1.

B. Make sure that the initial voltage of the high voltage power supply is set to zero volt.

C. Select the PIC mode.

D. Turn on the system power using the power switch of the NIM standard rack.

E. Turn on the isolated ground power supply.

F. Turn on the high voltage power supply.

G. Measure the PIC voltage using the oscilloscope.

H. In order to change the operational mode of the system, reduce the output voltage of the high voltage power supply to less than 50 volts.

I. Change the mode switch to steady state mode.

J. Recover the high voltage power supply to initial output level.

K. Measure the current using the picoammeter.

L. Whenever change the mode switch, make sure that the high voltage is less than 50 volts. Occasionally, measure the high voltage pulse using the high voltage pulse monitor terminal on the front panel, and oscilloscope.

APPENDIX B
SAFETY REPORT SUBMITTED TO THE UFTR SAFETY COMMITTEE

I. Introduction

A series of temperature dependent plasma kinetics measurement using He(UF_6) gas mixture was carried out successfully in the UFTR previously by Dr. W.H. Ellis, W. Choi and M. Baumgartner. Since the earlier experiments were performed with limited range of operating temperature of up to 550 °C, there continues to be a need for further investigation in order to consider much higher temperature characteristics. For this purpose, we developed a Multi-Probe Ionization Chamber (MPIC) System which will allow us to measure various plasma characteristics at much higher temperatures than the previous experiments. The MPIC system has extra features such as Langmuir and conductivity probes in addition to PIC probe, and will be tested by using He(^{3}He) gas mixture at first, which is relatively simple to handle, as a buffer or source gas. Later, the system will be filled and operated with He(UF_6) gas mixtures.

II. Proposal

Consideration and approval are requested for the insertion and use of an experimental assembly in the thermal column of the UFTR for temperature dependent plasma kinetic measurements using a special ionization chamber that will be filled with a series of differing gas compositions and operated with a heater and chamber housing configuration as a secondary containment to be described in more detail below. The ion chamber of interest, which is commercial grade and is specifically built for high temperature and high pressure ion chamber operation, is to be operated in the pulsed ionization chamber (PIC) mode, conductivity probe and Langmuir probe mode to study plasma production and loss kinetics and behavior of plasma properties, including electrical conductivity, as a functions of radiation field (gamma and neutron fluxes) and chamber gas temperature. For presently planned experiment, the chamber will be filled with noncorrosive He(^{3}He) gas to test the system performance. For future experiments the ion chamber will be filled with a series of corrosive He(UF_6) gas mixtures. Therefore, greater part of this report describes the safety aspect of future experiments except for the testing of the chamber integrity under the physical conditions common to both cases.

III. Description of Apparatus

A. Chamber The multiprobe ionization chamber is an ionization chamber equipped with extra probes to increase the capability of measuring as many parameters as possible. The chamber has been designed by the investigators and fabricated by the RTS Laboratory to ensure the quality of the chamber to meet the standards set by the UFTR Safety Committee.

The multiprobe ion chamber (Figure B.1) is made of Molybdenum and Type 304 S.S. for high temperature and high pressure operation in corrosive environments. It has coaxial electrode geometry with two field probes (also operable as Langmuir probes) inserted between the electrodes, a volume of 1700 cm^3 and rated at 1200 °C and 50 atmospheres. It is provided with a valved gas fill connection for the exchange of the fill gases. The thickness of the chamber walls have been calculated using standard equation recommended in the ASME code of boiler and pressure vessels. It also comprises an electrical heater and alumina thermal insulators inside the chamber. The thickness of the alumina thermal insulator was determined by calculating the required temperature drop across the insulator, assuming that all the heat generated will flow horizontally across the insulator (which is a conservative assumption). To make us sure that the S.S. chamber will not melt under the worst set of circumstances, a layer of flowing water coolant has been added. The water coolant in the coils, wrapping the ion chamber, will also serve as a neutron moderator.

B. Chamber Housing A gas tight chamber housing was designed and built to provide a controlled, sealed environment for the ion chamber. Its material and dimensions are shown in Figure B.2. Aluminum has been chosen because of good nuclear characteristic. The chamber housing has a long

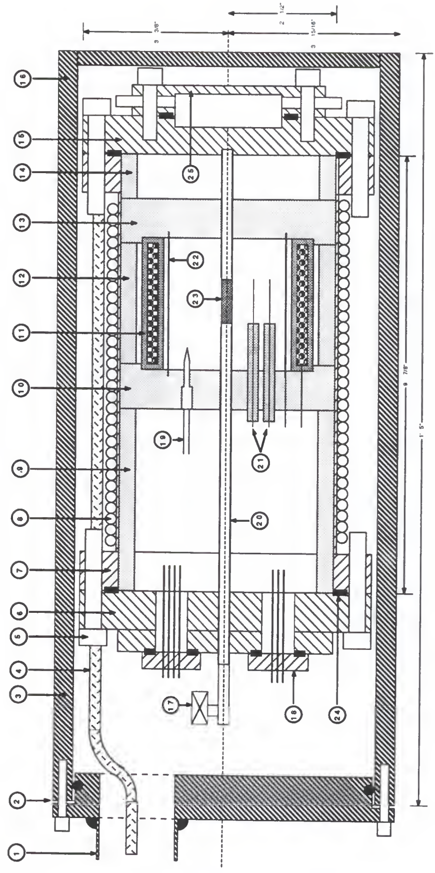

Figure B.1: MPIC and Chamber Housing

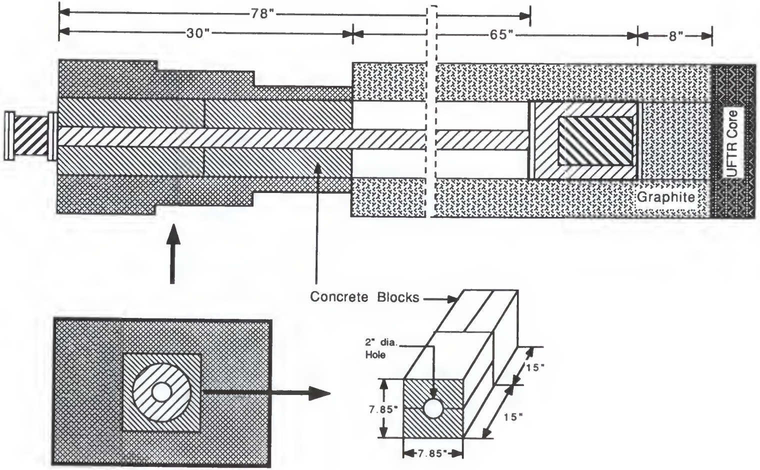

Figure B.2: Experimental Assembly Inserted in the Thermal Column of UFTR

conduit made of an Aluminum pipe to allow convenient connections between the ion chamber and the chamber housing connection box which will be extended outside of the UFTR.

C. Purge assembly A gas purge assembly will be connected to the chamber. This assembly (Figure B.3) will consist of a bottled nitrogen gas supply feeding the chamber housing through Nylon tubing. The nitrogen gas will be exhausted through a return line. When uranium fluoride gas compositions are studied the purge gas will also be passed by an installed fluorine detector, then bubbled first through a solution of NaOH and then through a solution of NaI. The NaOH will react with any uranium to remove it from the gas and the NaI will react with any fluorine that might be present. The exhausted gas will then be passed through a cold trap to remove any remaining uranium fluoride or moisture and finally removed through the core vent system.

IV. Description of Experiment

The access port shield blocks to the thermal column will be removed and four 4" x 4" x 48" graphite stringers will be taken out. The experimental assembly will be inserted to a point eight inches from the end of the thermal column. Instrumentation and control cabling will be extended to the outside of the thermal column through the chamber housing conduit and the special port shield blocks which can accommodate the conduit geometry will be installed as shown

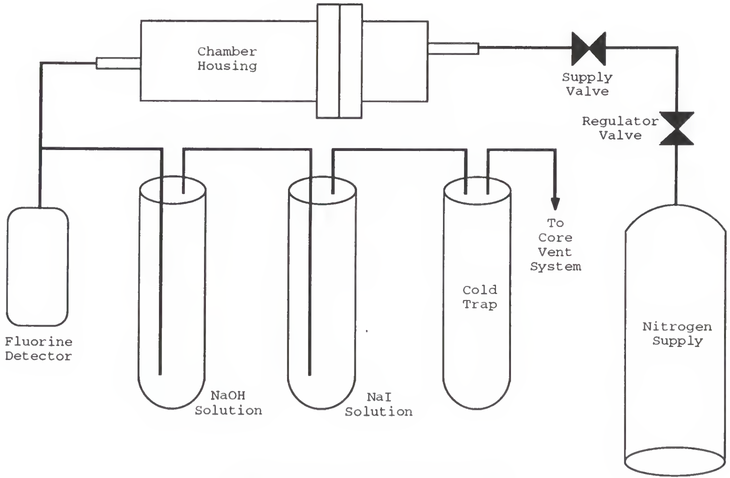

Figure B.3: Gas Purge System

in Figure B.2. Additional lead brick shielding will be positioned to compensate for the removal of the graphite stringers.

Prior to reactor startup, the gas purge system and the water cooling system will be placed into operation and their flow through the system verified by the bubbles. Furthermore, the system instrumentation will be energized and checked for proper operation prior to installation. Once this has been completed, leakage current measurements and chamber characteristic current measurements will be taken by operating the system in current mode and utilizing a picoammeter. Following these measurements, the system will be reconfigured for the multiprobe mode of operation and the reactor startup shall be commence.

During reactor startup, radiation level will be continuously monitored to prevent exceeding allowable limits. The highest reactor power possible commensurate with thermal limits and radiation levels will be established. Once power is stabilized, a series of source ionization measurements will be undertaken, beginning at ambient temperature and increasing to a maximum of 1200 °C. During the period of time the heater is energized, both the ion chamber and experimental assembly outer wall temperatures will be monitored to prevent the chamber temperature from exceeding 1200 °C and the experimental assembly outer wall temperature exceeding 85 °C (maximum center island core graphite temperature observed during extended (5 hrs) full power operation).

After the experimental data has been collected, the heater will be turned off and the reactor shutdown. The gas purge system and the water cooling system will be left in operation to assist in cooling the chamber. The experimental assembly will be left in the thermal column or in a shielded storage area in the reactor cell until radiation levels have been decayed to an acceptable level.

V. Safety consideration

The performance of nuclear generated plasma measurements using either depleted UF_6 or ^3He gases involves factors which must be considered for the safety of the investigators and for the UFTR. These are A)the use of high temperature heater inside the UFTR graphite moderator, B)the heating of a sealed chamber with no pressure relief path, C)the use of a toxic gas - UF_6, D)the activation of experimental assembly materials, E)the production of radioactive fission products from uranium, F)the heat generation inside the chamber from the fission of uranium. Each of these will be considered in turn.

A. Use of a high temperature heater inside the UFTR graphite moderator The operation of a heater inside the UFTR could lead to graphite damage if the assembly were poorly insulated or if the temperature of the assembly went unmonitored. These possibilities will be prevented by both system design and operating procedure.

The heater system has been designed and built using 1" thick alumina fiber insulation rated to 1600 °C. This temperature rating well exceeds the experimental temperature planned to be achieved in this experiment. Calculation performed with the heater system show that the steady-state outer wall temperature will be lower than 27 °C when the heater is stabilized at 1200 °C (the maximum temperature for this experiment) if cooling water were provided into the cooling channel with a minimum mass flow rate of 144 g/min (refer Section X.C). Both of these facts will ensure that the insulation will provide proper protection for the core if the heater were operated properly.

To provide the means to operate the heater properly, two thermocouples will be installed inside and outside of the heater assembly, and another thermocouple will be mounted against the aluminum housing outer wall. These thermocouples will be monitored during heater operation. In addition, an automatic heater temperature controller will be used to prevent over-ranging the heater rheostat when a new temperature is desired. Finally, temperature limits of 1200 °C for the heater and lower than 85 °C for the box outer wall will be established which will require the heater to be secured in order to prevent chamber and/or graphite damage. To prevent accidental coolant water loss caused by leakage of water inside the chamber housing, a special electronic circuit for detection of leakage water is provided. The circuit will actuate an alarm to warn the operator in case of water leakage inside the chamber housing.

B. Heating of a sealed chamber without pressure relief path The pressure inside the chamber will initially be one(1) to five(5) atmospheres at 25 °C. The maximum temperature at which the chamber will be operated is 1200 °C. This temperature increase will result in a pressure increase to 5 to 25 atmospheres. This is well within the range of the maximum design pressure of 50 atmospheres. In addition, if the chamber should rupture, the chamber housing will be able to absorb any resultant recoil energy.

C. Use of a toxic gas - UF_6 UF_6 reacts with atmospheric moisture to form UO_2F_2 and HF. UF_6, UO_2F_2 and HF are all dangerous compounds causing severe burns to body tissue. HF and F_2 are highly toxic. UO_2F_2 and UF_6 are also toxic especially if inhaled. To protect the individual from these dangers, OSHA has set the limits for UF_6 to be 0.05 $mg(U)/m^3$ and 2.5 $mg(F)/m^3$.

The chamber considered for use in this experiment has a volume of ~1700 cm^3. The maximum concentration of UF_6 to be used in this chamber will be 1.0 percent by volume. The amount of UF_6 this represents is:

$$\text{Amount } UF_6 = \frac{(1700\ cm^3)(0.01)(1\ \text{liter}/1000cm^3)(352\ g/\text{mole } UF_6)}{(22.4\ \text{liter}/\text{mole } UF_6)}$$

$$= 267.1\ mg(UF_6)$$

$$\text{Amount U} = \frac{(267.1\ \text{mg}(UF_6))(238\ \text{g/mole U})}{(352\ \text{g/mole}\ UF_6)} = 180.6\ \text{mg(U)}$$

Amount F = Amount UF_6 - Amount U = 86.5 mg(F)

It is obvious that, depending upon the volume in which the UF_6 is diluted, there is sufficient material present to exceed OSHA limits.

To prevent personal injury due to a loss of chamber integrity, the chamber will be tested leak-tight over the full temperature operating range prior to being used in the UFTR. In addition, the chamber will be mounted inside a chamber housing which will in turn be purged with nitrogen through solutions of NaOH and NaI as well as through a cold trap. Thus, in the event of a leak, the UF_6 will be scavenged by the liquid scrubbers or will solidify on the cold trap walls before it is able to reach the atmosphere or react with atmospheric moisture.

D. Activation of experimental assembly materials The experimental assembly is constructed of Aluminum (7450 g), Molybdenum (398 g), Type 304 stainless steel (7640 g), and Alumina (Al_2O_3, ~1000 g). After six hours of exposure to a neutron flux of 10^{10} n/cm^2-sec, these materials including coolant water will activate to form the radioactive nuclides summarized in Table B.1.

These nuclides will constitute a significant β- and γ-ray source immediately after reactor shutdown (past experiments showed radiation levels of up to 500 mr/hr immediately after shutdown). However, due to their short

Table B.1: Activation of experimental assembly materials

	Nuclide	Half-life	Activity
Short-lived	N^{16}	7.1 sec	90 μCi
	Al^{28}	2.3 min	11.49 Ci
	Mn^{56}	2.58 hr	4.79 Ci
	Cr^{55}	3.5 min	0.038 Ci
	Mo^{99}	66.7 hr	0.005 Ci
	Mo^{101}	14.6 min	0.012 Ci
		Total	16.335 Ci
Long-lived	Ni^{59}	$1x10^5$ yr	8.68 μCi
	Fe^{55}	2.6 yr	480 μCi
	Fe^{59}	45 d	186 μCi
	Mo^{92}	>100 yr	0.15 μCi
		Total	674.83 μCi

half-lives, storing the assembly in a shielded radiation area or leaving it in the thermal column to decay will significantly reduce the radiation problem. The long-lived nuclides will not pose a personnel hazard because of their low activity. The activities of long-lived nuclides (half-life longer than a year) shown above is based on 600 KW-hr neutron irradiation. This number would be somewhat underestimated. The total accumulated activity after expected experiment schedule (~100 KW-hr/experiment x 10 experiments = 1000 KW-hr) will be about 1.7 times higher, i.e., total of ~ 1.147 mCi. This amount of activity will not pose a personnel hazard. Data and sample calculations are shown in Section X.A.

E. Production of radioactive fission products from the fission of U The fuel being used is a depleted UF_6. Thus, the amount of fissionable U^{235} is:

$$U^{235} \text{ atoms} = (180 \text{ mg(U)})(0.0072\ U^{235}/U)(1 \text{ mole } U^{235}/235 \text{ g}) \times (6.023 \times 10^{23} \text{ atoms/mole}) = 3.32 \times 10^{18} \text{ atoms } U^{235}$$

$$U^{235} \text{ fission rate} = \sigma\Phi_{th}N = (5.822\times10^{-22} \text{ cm}^2)(10^{10} \text{ n/cm}^2\text{-sec}) \times (3.32\times10^{18} \text{ atoms}) = 1.93 \times 10^7 \text{ fissions/sec}$$

The amount of U^{238} available to undergo fast fission is:

$$U^{238} \text{ atoms} = (180 \text{ mg(U)})(0.9928\ U^{238}/U)(1 \text{ mole } U^{238}/238 \text{ g}) \times (6.023 \times10^{23} \text{ atoms/mole}) = 4.52 \times10^{20} \text{ atoms } U^{238}$$

$$U^{238} \text{ fission rate} = \sigma\Phi_{f}N = (0.58 \times 10^{-24} \text{ cm}^2)(10^{10} \text{ n/cm}^2\text{-sec}) \times (4.52 \times10^{20} \text{ atoms}) = 2.62 \times10^6 \text{ fissions/sec}$$

The fission products of interest are those with a yield above 1.0% and a half-life less than one year but greater than three minutes. A list of these fission products for both U^{235} thermal fission and U^{238} fast fission is included in Appendix B. These elements have half-life ranging from 52.2 minutes to 65 days. Assuming the reactor was operated a full six hour run at 100 KW, the maximum fission product activity produced would be ~236 μCi (sample calculations are shown in

Section X.B). This activity would be negligible compared to the activity produced in the chamber materials.

F. Heat generation inside the chamber from the fission of U Heat generation in the ion chamber could lead to chamber failure if it were to be a significant contribution to that of the heater. Assuming a combined fission rate of 2.94 x 10^7 fissions/sec and 200 MeV/fission, the heat generation rate would be 5.88 x 10^9 MeV/sec. Converting this to watts, the value would be 9.4 x 10^{-4} watts (assuming 1 MeV = 1.6x10^{-13} watt-sec). This will not be significant compared to other heat source and will not pose a safety hazard (the heater consumes 850 watts for the generation of heat needed to raise the chamber temperature to 1200 °C).

VI. Reactivity contribution

The results of the observed reactivity contribution by inserting an experimental assembly, which is almost identical as the one proposed to be used for this experiment, into the thermal column of the UFTR were tabulated below.

Table B.2: Measured Reactivity Contribution to the UFTR by Inserting an Experimental Assembly

condition	reactivity contribution	date
with assembly	0.095% $\delta k/k$	15 July, '88
w/o assembly	0.080% $\delta k/k$	12 July, '88
with assembly	0.070% $\delta k/k$	03 June, '88
with assembly	0.073% $\delta k/k$	17 May, '88

By the results one can safely conclude that the reactivity contribution by inserting the proposed experimental assembly into the thermal column of the UFTR will be less than 0.1% δk/k, which is far less than the limit value of 0.6% δk/k required by the UFTR Tech. Spec. Reactivity Limitations on Experiments.

VII. Maximum credible accident

Chamber filled with UF_6 Gas The maximum credible accident would occur if the chamber were to be handled and break immediately after reactor operation. Assuming the chamber was filled with 1.0% UF_6 by volume, this would result in the release of 267.1 mg UF_6 (180.6 mg U and 86.5 mg F). Assuming expansion of the UF_6 to occupy one-half the cell volume (excluding the control room and reactor volume), the different concentration would be:

$$[U] = \frac{180\ mg(U)}{(0.5)(5.18 \times 10^5\ ft^3)(1\ m^3/3.54\ ft^3)}$$

$$= \frac{180\ mg(U)}{7.3 \times 10^4\ m^3} = 2.46 \times 10^{-3}\ mg(U)/m^3$$

$$[F] = \frac{86.5\ mg(F)}{7.3 \times 10^4\ m^3} = 1.18 \times 10^{-3}\ mg(F)/m^3$$

These concentrations are far below OSHA limits. They are also below the 10CFR20 limit of 0.2 mg/m^3 for a soluble depleted uranium mixture. In reality, the concentration could be expected to be lower still due to the UF_6 plating out on materials as it cooled below 56 °C.

The break in the chamber would also release any fission products which had been produced. Assuming that the products expanded to fill the entire cell volume, the airborne activity released would be:

$$\text{Activity} = \frac{(236\ \mu\text{Ci})(1\ \text{m}^3/1\text{x}10^6\ \text{ml})}{1.46\text{x}10^5\ \text{m}^3} = 1.6 \text{ x } 10^{-9}\ \ \mu\text{Ci/ml}$$

This activity would take approximately 15 minutes to diffuse throughout the cell volume and, during that time, the activated F^{19} (half-life: 11.2 sec) also released would decay to a negligible value. This concentration would be below regulatory concern. (See Section X.B)

The maximum credible accident will be avoided by not removing the ion chamber from the experimental assembly until it has cooled below 56 °C. This will allow time for the fission product to decay as well as allow for the UF_6 to plate out on the ion chamber inner surface.

Chamber filled with ^{3}He Gas The maximum credible accident would occur if the chamber were to be handled and break after maximum time of neutron irradiation caused by full power reactor operation. Assuming the chamber was filled with 1 atm ^{3}He (4.56×10^{22} atoms in 1700 cm^3), this would result in the release of 5.417×10^{16} Tritiums by ^{3}He(n,p)T reaction (σ = 5500 b) after 6 hours of irradiation by the thermal neutron flux of 10^{10} n/cm^2-sec. Assuming expansion of the T to occupy one-half the cell volume (excluding the control room and reactor volume), the airborne activity released would be:

$$\text{Activity} = \frac{(2623\ \mu\text{Ci})(1\ \text{m}^3/1\text{x}10^6\ \text{ml})}{1.46\text{x}10^5\ \text{m}^3} = 1.7 \text{ x } 10^{-8}\ \mu\text{Ci/ml}$$

This concentration would be still below regulatory limit of 1 x 10^{-7} μCi/ml.

VIII. Experimental Procedures

A. Prior to insertion

1. Use the gas handling system to fill the ion chamber with the desired gas mixture
2. Leak test the exposed ion chamber and chamber housing
   a. Seal the chamber by shutting the fill valve.
   b. Seal the chamber housing after inserting ion chamber into the chamber housing
   c. Shut the purge line return valve.
   d. Open the purge line supply valve.
   e. Adjust the nitrogen bottle regulator to supply nitrogen at 20 psig.
   f. Soap check the chamber housing flange and penetration for leaks after 15 minutes.
   g. Repair any detected leaks.
   h. Upon completion of the soap test, shut the nitrogen bottle.
   i. Initiate gas purge system.
   j. Cycle the heater and ion chamber over the entire range of operating temperature.
   k. During the temperature cycling, check for UF_6 leak using a portable monitor.
   l. If no leak is detected, shut down gas purge system and proceed to B.

   m. If a leak is detected, secure the heater, forcibly cool the ion chamber below 56 °C, and repair the leak.

B. Prior to reactor startup

1. Install the experimental assembly into the UFTR thermal column and add the necessary lead brick shielding.
2. Check equipment for proper operation. Perform leakage current and characteristic current measurements.
3. Initiate the gas purge and check for proper operation.

C. During reactor operation

1. Commence reactor startup and monitor radiation levels.
2. Establish the highest steady-state reactor power possible commensurate with thermal limit and allowable radiation levels.
3. Commence measurements for varying temperatures up to a maximum ion chamber temperature of 1200 °C.
4. Following data collection, turn off the heater and shutdown the reactor.

D. Following reactor shutdown

1. Leave the experimental assembly in the thermal column or place it in the cell radiation area to decay to acceptable radiation levels.

CAUTION: Do not handle the ion chamber or chamber housing until they have cooled to less than 56 °C.

IX. Emergency Procedures

A. In the event of ion chamber leak:

1. If the ion chamber is outside the chamber housing prior to reactor operation:
   - a. Maintain the ion chamber temperature below 56 °C.
   - b. Attempt to seal the chamber by tightening the fill

gas valve and flange bolts.

c. Check the area for the presence of fluorine using the portable monitor.

d. Clean up any UF_6 deposit using a solution of NaOH.

2. If the chamber is inside the chamber housing:

    a. Secure both the heater and the reactor if operating.

    b. Start or maintain operation of the nitrogen purge system.

    c. Check the area for the presence of fluorine.

    d. Remove the experimental assembly for cleanup when the ion chamber temperature has ben reduced less than 56 °C.

B. In the event of a purge system or thermocouple failure, the experiment shall be stopped until the effected component can be repaired or replaced.

X. Supplementary Calculations

X.A. Experimental Assembly Activation Calculation

The activation of experimental assembly materials was determined by weighing or approximating the weight of the individual components, determining the weight of particular element present in that component, and then determining its activation rate knowing the thermal neutron capture cross-section and the thermal neutron flux.

For example, the Type 304 stainless steel part of ionization chamber weighs ~7640 g. Iron forms 68% (by weight) of Type 304 stainless steel. Fe^{54} comprises 5.84% of all iron. Therefore, there is ~303 g of Fe^{54} present in the chamber. Fe^{54} undergoes a neutron capture reaction (σ_c = 2.9b) to form radioactive Fe^{55} (half-life = 2.6 yrs).

Assuming a thermal neutron flux of 10^{10} n/cm^2-sec, the amount of radioactive Fe^{55} formed after a six hour run at 100 KW would be (neglecting decay):

$$\begin{aligned}\text{Amount Fe}^{55} &= (303\ \text{g})(1\ \text{mole}/54\ \text{g})(6.02\text{x}10^{23}\ \text{atoms/mole})\text{x} \\ &\quad (10^{10}\ \text{n/cm}^2\text{-sec})(2.9\text{x}10^{-24}\ \text{cm}^2)(6\ \text{hrs})\text{x} \\ &\quad (3600\ \text{sec/hr}) \\ &= 2.11 \text{ x } 10^{15}\ \text{atoms Fe}^{55}\end{aligned}$$

The activity of Fe^{55} would be:

$$\begin{aligned}\text{Act.of Fe}^{55} &= \frac{(2.11\text{x}10^{15}\ \text{atoms})(0.693)(1/2.6\text{yrs})(3.17\text{x}10^{-8}\text{yr/s})}{3.7 \text{ x } 10^{10}\ \text{dps}} \\ &= 480\ \mu\text{Ci}\end{aligned}$$

All activities were computed in this manner with the exception of Al^{28}, N^{16} and Cr^{55} for which the equilibrium concentrations were used. The following tables include activities for the major elements contained in each component.

Radioactivity of the coolant water was calculated as follows: Minimum 2.4 g/sec of water mass flow rate is required to keep the outer wall temperature of the experimental assembly below room temperature (Refer Section X.C). Total volume of the water channel is ~265 cm^3. Considering the water density of 1 g/cc, (265 g ÷ 30 g/sec =) 110 sec is needed to completely refresh the water inside the channel. In other words, the coolant water passing through the coolant channel will take about 110 seconds before it return to the outside of the reactor core. Therefore average residence time of 110 sec in the reactor core under the thermal neutron flux of 10^{10} n/cm^2-sec results in the activation of Oxygen in water by $O^{16}(n,p)N^{16}$ reaction. The average water weight staying in the core in 110 second

Table B.3 Activation of Type 304 SS (7640 g):
Fe-68%,Cr-20%,Ni-10%,Mn-2%

Element	Abundance	Weight	σ_c	$T_{1/2}$	Daughter	Activity
Fe^{54}	5.84 %	303 g	2.9 b	2.6 yrs	Fe^{55}	480 µCi
Fe^{58}	0.31 %	15.7 g	1.1 b	45 d	Fe^{59}	186 µCi
Cr^{50}	4.31 %	65.5 g	17 b	27.8 d	Cr^{51}	0.88 mCi
Ni^{58}	67.8 %	517 g	4.4 b	10^5 yrs	Ni^{59}	8.68 mCi
Mn^{55}	100 %	152 g	13.3b	2.6 hr	Mn^{56}	4.79 Ci
Cr^{54}	2.36 %	35.7 g	0.36b	3.5 min	Cr^{55}	38.7 µCi

Table B.4 Activation of Aluminum (7450 g)

Element	Abundance	Weight	σ_c	$T_{1/2}$	Daughter	Activity
Al^{27}	100 %	7450 g	0.24b	2.3 min	Al^{28}	10.77 Ci

Table B.5 Activation of Molybdenum (398 g)

Element	Abundance	Weight	σ_c	$T_{1/2}$	Daughter	Activity
Mo^{92}	15.86 %	62.07 g	0.3b	>100 y	Mo^{92}	0.1 µCi
Mo^{98}	23.75 %	92.95 g	0.51b	66.7 h	Mo^{99}	4.9 mCi
Mo^{100}	9.62 %	37.65 g	0.2b	14.6 m	Mo^{101}	12 mCi

Table B.6 Activation of Alumina (1000 g)

Element	Abundance	Weight	σ_c	$T_{1/2}$	Daughter	Activity
Al^{27}	100 %	529 g	0.24b	2.3 m	Al^{28}	722 mCi
O^{16}	99.8 %	471 g	1.9×10^{-5}b	7.1 s	N^{16}	90 µCi

residence time is 265 g. Oxygen occupies ~88.8% of water. Therefore, the Oxygen weight is ~235 g.

$$\begin{aligned}\text{Amount } N^{16} &= (235\text{ g})(1\text{ mole}/16\text{ g})(6.02 \times 10^{23}\text{ atoms/mole})\text{x}\\ &\quad (10^{10}\text{ n/cm}^2\text{-sec})(1.9 \times 10^{-29}\text{ cm}^2)\\ &= 1.68 \times 10^6 \text{ atoms } N^{16}\text{ /sec}\end{aligned}$$

The activity of N^{16} would be:

$$\begin{aligned}\text{Activity of } N^{16} &= \frac{(1.68 \times 10^6 \text{ atoms/sec})}{(3.7 \times 10^{10}\text{ dps})}\{1-e^{-(0.693\text{x}110/7.1)}\}\\ &= 45.4\ \mu\text{Ci}\end{aligned}$$

Because of its short half-life, this activity will drop to less than $1\text{x}10^{-6}$ μCi after 3 minutes later, which is negligible.

X.B. Fission Product Activity Calculation

The individual fission product activity was calculated by using the thermal fission rate of U^{235} (or the fast fission rate for U^{238}), multiplying it with a given nuclide's fission yield, multiplying this again with the appropriate decay constant and six hours of run time, and dividing by 3.7×10^{10} dps. For example, Sr^{89} has a thermal fission yield of 4.79% and a half-life of 50.5 days. Assuming a thermal fission rate of 1.93×10^7 fissions/sec, the activity of Sr^{89} would be:

$$\begin{aligned}\text{Activity of } Sr^{89} &= (1.93 \times 10^7 \text{ fissions/sec})(0.0479)(0.693)\text{x}\\ &\quad (6\text{ hr})(21600\text{ sec}/6\text{ hrs})(1/50.5\text{ days})\text{x}\\ &\quad (1\text{ d}/8.64\text{x}10^4\text{ sec})(1/3.7 \times 10^{10}\text{ dps})\\ &= 0.085\ \mu\text{Ci}\end{aligned}$$

All activities were calculated using this method with the exception of I^{134} and Ba^{139} for which equilibrium concentrations were used. The following Tables B.7 and B.8 list the fission products considered for fast and thermal fission, their activities in μCi, their dispersed activity concentration in μCi/ml, and the appropriate 10 CFR 20 limit also in μCi/ml.

X.C. Calculation of the Temperature at the Outside of Insulator

1)Without water cooling

Figure B.4 shows the geometry and dimensions of the heater, insulator and cooling system. Let us assume that heat flow is zero in axial direction and equal in all radial direction. And assume $T(a) = T(b)$, since $k_i \ll k_h$. Therefore, all the heat generated by the heater will flow out of the outer surface of the heater. Then, the temperature at the outside wall of the insulator,

$$T(c) = T(a) - \frac{q''a^2}{4k_h}[(b/a)^2 - 2\ln(b/a) - 1] - \frac{q''a^2}{2k_i}\ln(c/b)[(b/a)^2 - 1]$$

$$\approx T(a) - \frac{q''a^2}{2k_i}\ln(c/b)[(b/a)^2 - 1]$$

where, $q'' = \frac{q}{[\pi(b^2-a^2)L]} = 9.7996 \times 10^5 \ (W/m^3)$

Inserting all the numbers to calculate T(c) gives

$$T(c) \approx 1500(K) - 1096(K) = 404\ (K) = 131\ (^{\circ}C) = 393\ (^{\circ}F)$$

which is too high to be inserted in the thermal column of the UFTR (outside wall temperature of the assembly should be

Table B.7. Fission Products from Fast Fission of U^{235} at the Fast Flux of 10^{10} n/cm^{2}-sec for 6 hrs

F.P.	%Yield	Half-life	Activity (μCi)	Dis. Activity (μCi/ml)	10CFR20 Limit(μCi/ml)
Sr^{89}	2.9	50.5 d	5.38x10^{-3}	3.68x10^{-14}	3x10^{-8}
Mo^{99}	6.3	66.5 h	1.08x10^{-1}	7.39x10^{-13}	2x10^{-7}
Ru^{103}	6.6	39.7 d	2.78	1.90x10^{-11}	8x10^{-8}
Te^{132}	4.7	77.0 h	1.94x10^{-2}	1.38x10^{-13}	1x10^{-7}
Ba^{140}	5.7	12.8 d	1.82x10^{-1}	1.24x10^{-12}	4x10^{-8}
Nd^{147}	2.6	11.1 d	2.78x10^{-2}	1.90x10^{-13}	2x10^{-7}
Pm^{149}	1.8	53.1 h	9.86x10^{-2}	6.75x10^{-13}	2x10^{-7}

Table B.8. Fission Products from Thermal Fission of U^{235} at the Thermal Flux of 10^{10} n/cm^{2}-sec for 6 hrs

F.P.	%Yield	Half-life	Activity (μCi)	Dis. Activity (μCi/ml)	10 CFR 20 limit(μCi/ml)
Sr^{89}	4.8	50.5 d	8.50x10^{-2}	5.86x10^{-13}	3x10^{-8}
Sr^{91}	5.8	9.7 h	12.9	8.71x10^{-11}	3x10^{-7}
Y^{91}	5.4	58.0 d	8.30x10^{-2}	5.71x10^{-13}	3x10^{-8}
Sr^{92}	5.3	2.7 h	41.76	2.85x10^{-10}	3x10^{-7}
Y^{93}	6.1	10.3 h	12.89	8.78x10^{-11}	1x10^{-7}
Zr^{95}	6.2	65.0 d	8.50x10^{-2}	5.68x10^{-13}	3x10^{-8}
Zr^{97}	5.9	17.0 h	7.39	5.05x10^{-11}	9x10^{-8}
Mo^{99}	6.1	66.5 h	1.95	1.34x10^{-11}	2x10^{-7}
Ru^{103}	3.0	39.7 d	6.75x10^{-2}	4.62x10^{-13}	8x10^{-8}
I^{131}	3.1	8.05 d	3.37x10^{-1}	2.31x10^{-12}	9x10^{-9}
Te^{132}	4.7	77.0 h	1.29	8.78x10^{-12}	1x10^{-7}
I^{133}	6.9	20.8	6.7	4.62x10^{-11}	3x10^{-8}
Xe^{133}	6.6	5.27 d	1.10	7.48x10^{-12}	1x10^{-6}
I^{134}	7.8	52.5 m	40.53	2.77x10^{-10}	5x10^{-7}
I^{135}	6.1	6.7 h	19.65	1.34x10^{-10}	1x10^{-7}
Xe^{135}	6.3	9.2 h	14.73	1.00x10^{-10}	4x10^{-6}
Ba^{139}	6.6	83.0 m	33.77	2.31x10^{-10}	1x10^{-6}
Ba^{140}	6.4	12.8 d	4.42x10^{-1}	3.02x10^{-12}	4x10^{-8}
La^{141}	6.4	3.8 h	36.23	2.47x10^{-10}	3x10^{-9}
Ce^{141}	6.0	33 d	1.59x10^{-1}	1.08x10^{-12}	2x10^{-7}
Ce^{143}	5.7	33 h	3.68	2.52x10^{-11}	2x10^{-7}
Nd^{147}	2.7	11.1 d	2.14x10^{-1}	1.46x10^{-12}	2x10^{-7}

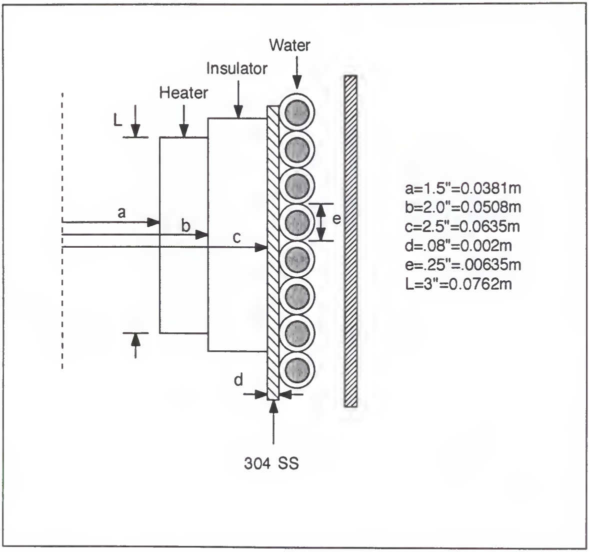

Figure B.4: Cross-Sectional View of Experimental System

maintained lower than 85 °C). Therefore another means of insulation is needed.

2) With water cooling

Additional water cooling system should lower outside wall temperature of experimental assembly to acceptable level. One can safely neglect temperature drops across S.S. wall since the thermal conductivity of 304 SS (16.3 W/mK) is much higher than that of insulator (0.2 W/mK) and water (0.6 W/mK). Then the bulk temperature of the coolant T(e) is given as

$$T(e) \approx T(a) - \frac{q''a^2}{2}[(b/a)^2 - 1][\frac{1}{k_i}\ln(c/b) + \frac{1}{hc}]$$

where, h is heat transfer coefficient of the water.

For heat transfer of water flowing in a circular tube with large temperature drop across the film, the Sieder-Tate equation is useful for finding h values;

$$Nu = \frac{hD_e}{k} = 0.023\ Re^{0.5}\ Pr^{0.4}\ (\frac{\mu_w}{\mu})^{0.14},$$

where, Nu = Nusselt number = hD_e/k
Re = Reynolds number = $D_eV\rho/\mu$
Pr = Prandtl number = $c_p\mu/k$

One needs to know the mass flow rate to calculate the heat transfer coefficient. Or if one chooses an h value first, then one can calculate the mass flow rate (m) to maintain the chosen h value (and fluid temperature) by using the relationship

$$m = \rho VA_c = \mu A_cD_e[\frac{43.478h}{kPr^{0.4}(\frac{\mu_w}{\mu})^{0.14}}]^2,\ \text{lb/hr}$$

where, ρ = density of coolant, lb/ft^3
A_c = cross-sectional area of channel, ft^2
h = heat-transfer coefficient (Btu/hr-ft^2-°F)
D_e = 0.25" = 0.02083 ft
V = velocity of coolant, ft/hr
k = thermal conductivity (Btu/hr-ft-°F)
c_p = specific heat = 0.9975 (Btu/lb-°F) @ T = 80 °F
μ = viscosity = 2.048 (lb/hr-ft) @ T = 80 °F
μ_w = viscosity = 0.52 (lb/hr-ft) @ T = 268 °F

For example, if we want to keep the water bulk temperature at 300 K, the required heat transfer coefficient of the water is calculated as below.

From $T(e) \approx T(a) - \frac{q''a^2}{2}[(b/a)^2 - 1][\frac{1}{k_i}\ln(c/b) + \frac{1}{hc}]$,

$$h \approx (1/c)\{\{[T(a)-T(e)]/[q''a^2/2][(b/a)^2 - 1]\} - (1/k_i)\ln(c/b)\}^{-1}$$

$$= (15.748)\{[1200/(1181.7\text{x}0.7777)] - 1.1157\}^{-1}$$

$$= 82.868\ (\text{W/m}^2\text{-K}) = 14.584\ (\text{Btu/hr-ft}^2\text{-°F})$$

where, 1 (W/m^2-K) = 0.176 (Btu/hr-ft^2-°F)

Since we know the heat transfer coefficient, we can calculate the required mass flow rate to keep the water temperature at 300 K from the relationship,

$$m = \rho V A_c = \mu A_c D_e \left[\frac{43.478h}{k\Pr^{0.4}\left(\frac{\mu_w}{\mu}\right)^{0.14}} \right]^2$$

$$= (2.048)(3.409\text{x}10^{-4})(0.0208)\left[\frac{(43.478)(14.584)}{(0.3532)(5.25^{0.4})\left(\frac{0.327}{2.048}\right)^{0.14}} \right]^2$$

$$= 19.04\ (\text{lb/hr}) = 0.317\ (\text{lb/min})$$

$$= 144\ (\text{g/min}) = 0.038\ (\text{Gal/min})$$

APPENDIX C
LabVIEW PROGRAMS

1. Introduction to LabVIEW™

Connecting instruments to computer over a common bus is actually a networking problem. This is becoming more evident with the increasingly sophisticated instruments being manufactured today. The GPIB or IEEE-488, and RS-232 and RS-422 standards address the electrical and mechanical issues of networking quite well but address the functional issues only to a limited extent [25].

The GPIB is a link, or bus, or interface system through which interconnected electronic devices communicate. Hewlett-Packard invented the GPIB, which they call the HP-IB, to connect and control programmable instruments manufactured by them. Because of its high system data rate ceiling of 250 Kbytes to 1 Mbytes/sec, the GPIB quickly become popular in other applications such as intercomputer communication and peripheral control. It was later accepted as the industry standard and is defined by ANSI/IEEE standard 488-1978. The versatility of the system prompted the name General Purpose Interface Bus (GPIB).

The Laboratory Virtual Instrument Engineering Workbench (LabVIEW), developed by National Instrument [24], is designed to simplify programming scientific computation, process control, and test and measurement applications.

The central concept underlying LabVIEW is the virtual instrument (VI). A VI is similar in modularity and function to a physical instrument; however, it is constructed out of software. A VI is hierarchic; that is, one VI can include a variety of other VIs as components. The hierarchical modularization applies to all levels of an application form the bottom level corresponding the physical instrument or primitive computation to the top level corresponding to the measurement or analysis system. A VI consists of a front panel for interactive control, a block diagram that specifies flow of control and data, and an icon to represent instrument when it is used within the diagram of another VI.

One can build a VI by constructing a front panel from a palette of built-in controls and indicators, drawing a diagram incorporating icons of previously designed VIs or built-in VIs, and finally, designing an icon to represent the new VI.

A VI is operated directly from its front panel by simply configuring the inputs and clicking with the mouse connected to Macintosh personal computer to execute. Any VI can be configured to log data each time it executes. At the end of execution, the complete front panel is logged by run number and time stamped. The user can interactively or programmably access the logged data.

2. LabVIEW Programs for the Experiment

VIs built for the instruments and experiment utilized in this study are described in detail below. The programs representing each VI are generated by using the report generation feature of the LabVIEW.

2.1. 485 Picoammeter

This VI represents the Keithley 485 picoammeter. It can be used to control a input current range or to take data from the instrument remotely (Figure C.1).

2.2. Running 485

The VI "Keithley 485 picoammeter" was used as a sub-VI in this VI for multiple data acquisition and analysis. After multiple data acquisition, a mean and a standard deviation of the data are calculated and displayed on the front panel. A graphical display of the data fluctuation between the multiple measurements is also provided (Figure C.2).

2.3. Voltage at Time

This VI, when executed, picks up a PIC voltage value at electron (or ion) collection time. It uses a sub-VI which is built for the control of Tektronix 2430A digital oscilloscope. The collection time is a control variable and it has to be configured before execution (Figure C.3).

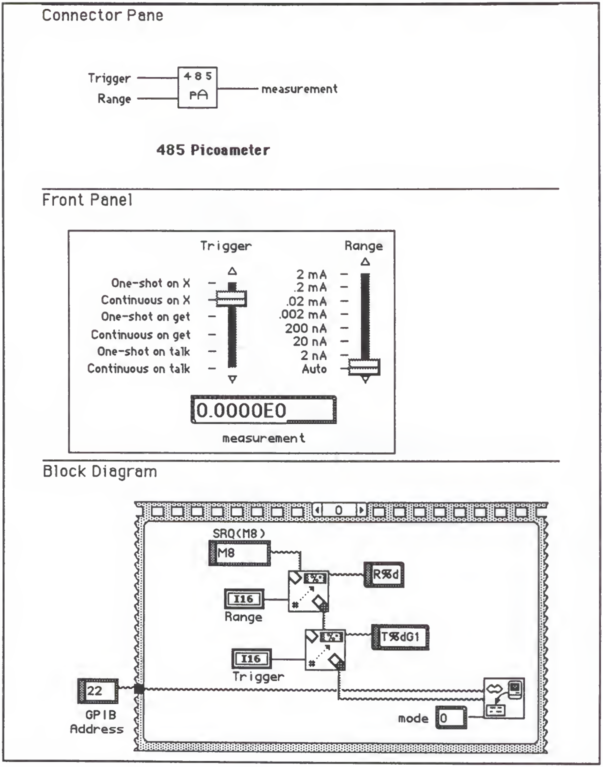

Figure C.1: Program "485 Picoammeter"

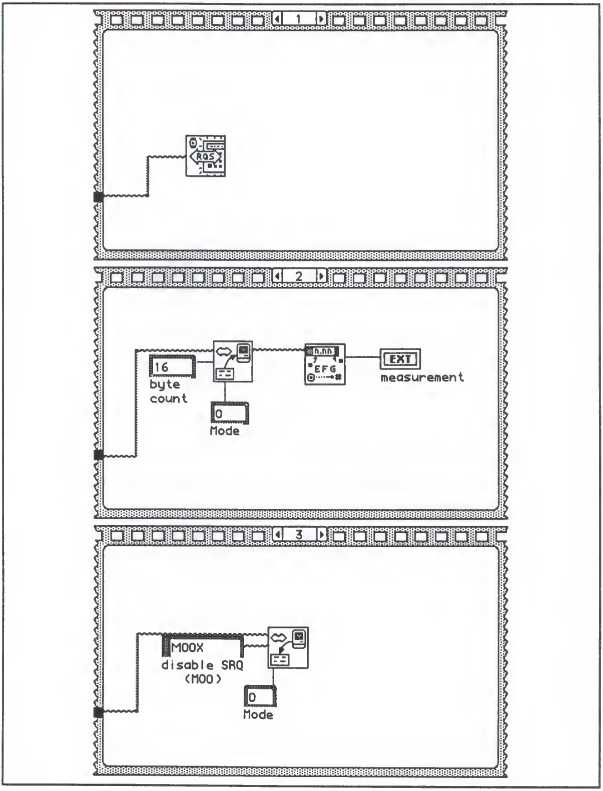

Figure C.1: Program "485 Picoammeter" (continued)

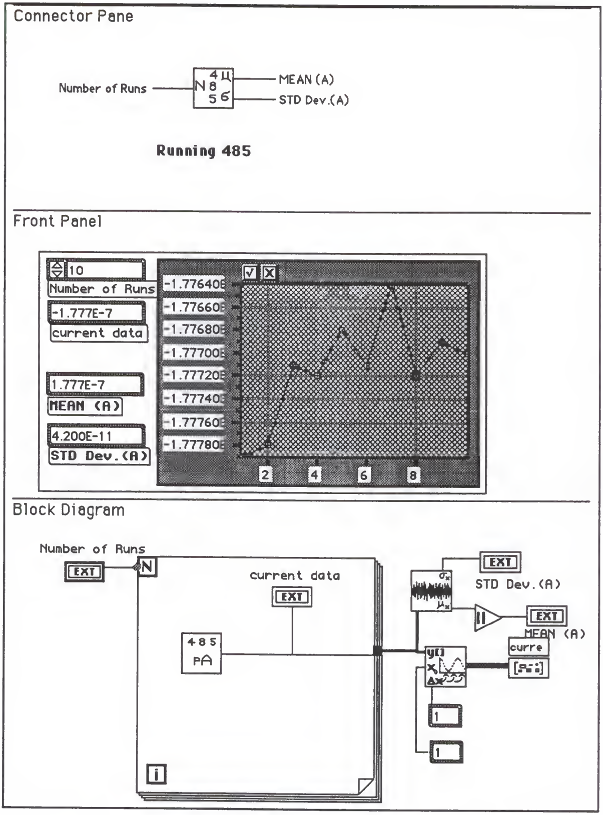

Figure C.2: Program "Running 485"

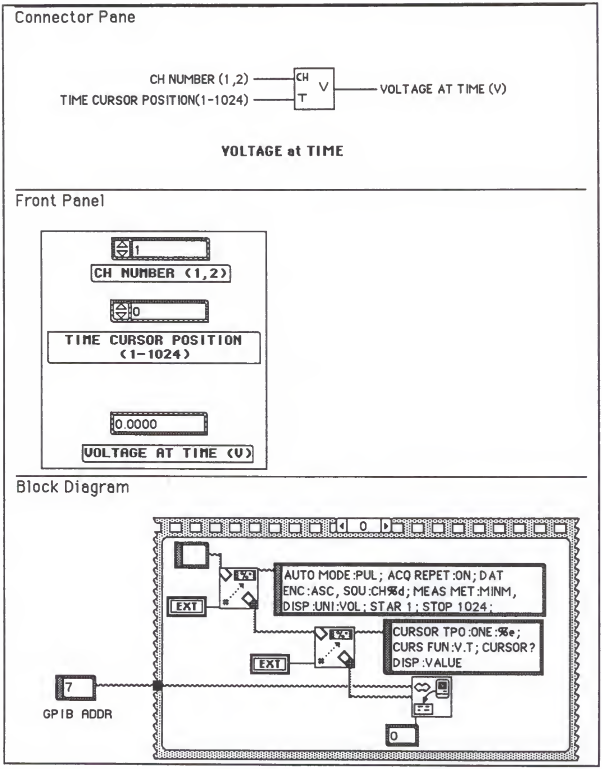

```
AUTO MODE:PUL; ACQ REPET:ON; DAT
ENC:ASC, SOU:CH%d; MEAS MET:MINM,
DISP:UNI:VOL; STAR 1; STOP 1024;
```

```
CURSOR TPO:ONE:%e;
CURS FUN:V.T; CURSOR?
DISP:VALUE
```

Figure C.3: Program "Voltage at Time"

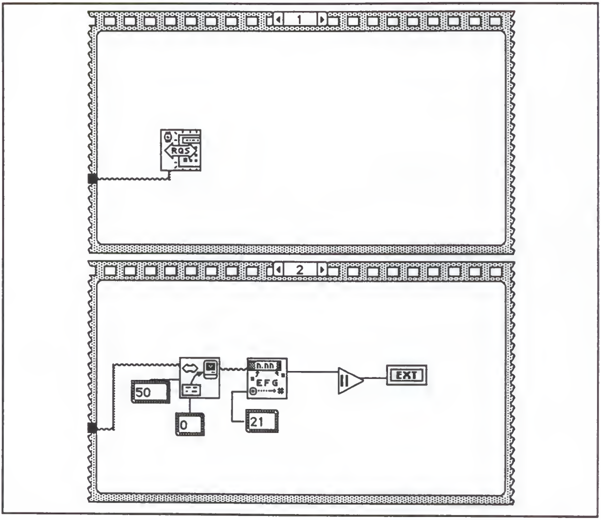

Figure C.3: Program "Voltage at Time" (continued)

2.4. Running 2430

The VI "Voltage at Time" was used as a sub-VI in this VI for multiple data acquisition and analysis. After multiple data acquisition, a mean and a standard deviation of the data are calculated and displayed on the front panel. A graphical display of all the data fluctuation between the multiple measurements is also provided (Figure C.4).

2.5. PIC Instrument

This VI is built for programmable retrieval of the logged data from the VIs "Running 485" and "Running 2430", and plotting the characteristic I-V plot for the PIC mode operation of the MPIC system (Figure C.5).

2.6. 113DR DDG

This VI represents the Avionics 113DR Digital Delay Generator which has three delay independent channels. By using this program one can remotely set delay times for the three delay channels which represent high voltage pulse rate, high voltage pulse duration and high impedance delay time (Figure C.6).

2.7. Conductivity Probe

The conductivity probe VI, shown in Figure C.7, is built for direct measurement of electrical conductivity of plasma

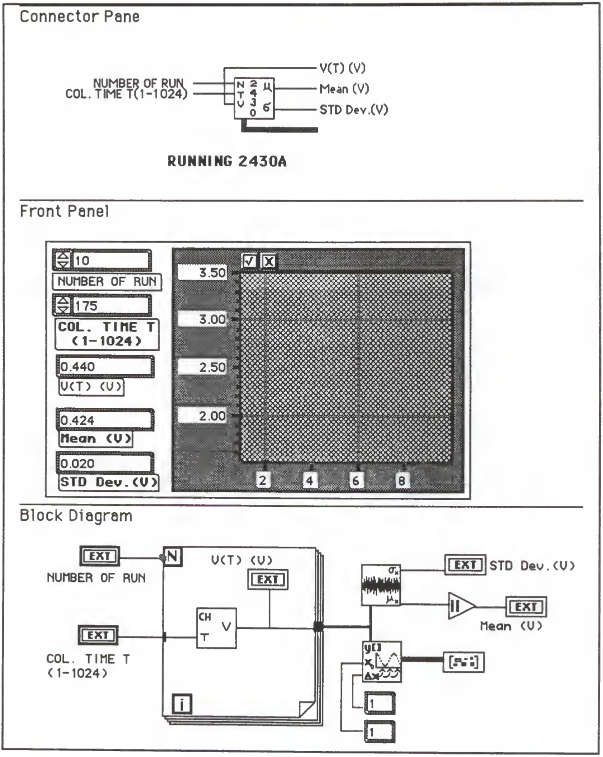

NUMBER OF RUN: 10

COL. TIME T (1-1024): 175

V(T) (V): 0.440

Mean (V): 0.424

STD Dev.(V): 0.020

Figure C.4: Program "Running 2430"

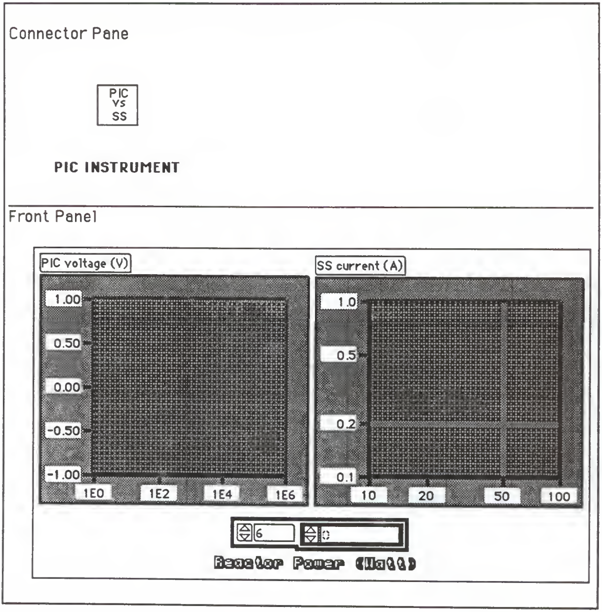

Figure C.5: Program "PIC Instrument"

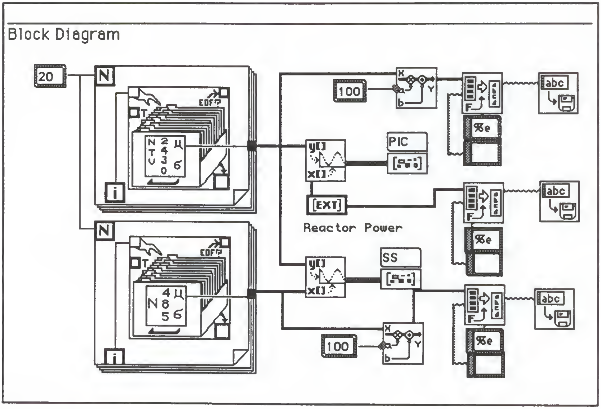

Figure C.5: Program "PIC Instrument" (continued)

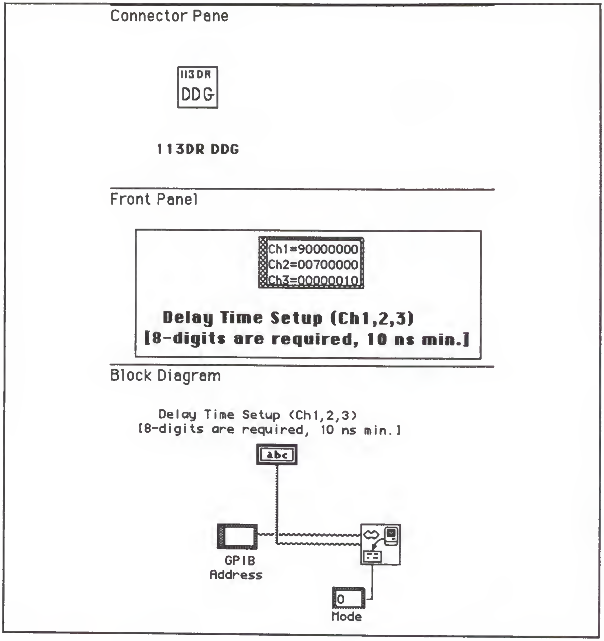
Connector Pane
113DR
DDG
113DR DDG
Front Panel
Ch1=90000000
Ch2=00700000
Ch3=00000010
Delay Time Setup (Ch1,2,3)
[8-digits are required, 10 ns min.]
Block Diagram
Delay Time Setup (Ch1,2,3)
[8-digits are required, 10 ns min.]
abc
GPIB
Address
0
Mode

Figure C.6: Program "113DR DDG"

Front Panel

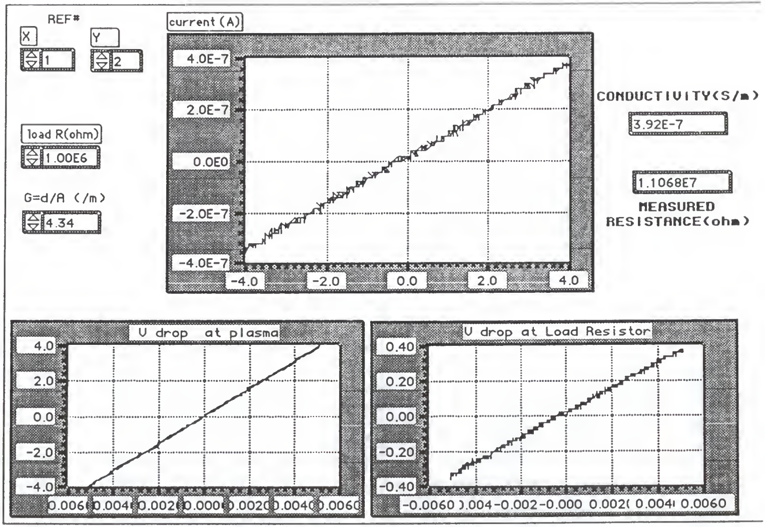

REF#

X 1

Y 2

load R(ohm) 1.00E6

G=d/A (/m) 4.34

CONDUCTIVITY(S/m) 3.92E-7

MEASURED RESISTANCE(ohm) 1.1068E7

Figure C.7: Conductivity Probe

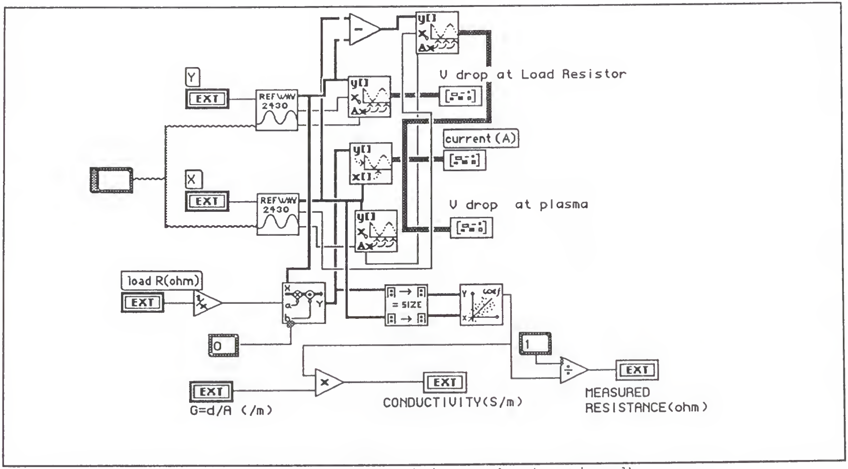

Figure C.7: Conductivity Probe (continued)

in the multiprobe ionization chamber (MPIC). Voltage drop across the anode and the cathode of the MPIC and current flowing through the two plasma probes inserted in the MPIC are recorded by the digital oscilloscope. Operator needs to provide the value of "load resistor" and "G (geometrical factor)" to calculate the conductivity. The front panel will display the voltage drop at plasma and voltage drop at the load resistor, which will be used to calculate the current flow in the plasma. The current and voltage values which consisted of over 1000 pairs of (V,I) data are linearly fitted to find the slope which is directly related to the plasma resistance. After the plasma resistance is determined, the electrical conductivity of the plasma is calculated by multiplying a geometrical factor to the plasma resistance.

LIST OF REFERENCES

1. N.J. Diaz, S. Anghaie, E.T. Dugan and I. Maya, "Gas Core Reactor and Energy Conversion Research Program," Innovative Nuclear Space Power & Propulsion Institute Final Report INSPI-FR-UF-001 to 004, Vol. 1 to 4 (1988)

2. C. Collins, S.C.P. Wang, S. Anghaie, "Investigation of High-Temperature Materials for Uranium-Fluoride-Based Gas Core Reactor System," ANS Trans., Vol.57, 84 (1988)

3. R.J. Rosa, "Magnetohydrodynamic Energy Conversion," McGraw-Hill, Inc, New York, (1968)

4. J. Braun, K. Nygaard, E. Witalis, "On Plasma Through Neutron Irradiation," Proc. Int. Symp. on MHD Power Generation, Paris, paper 10 (1964)

5. K. Imani, "MHD Electric Power Generation with Nuclear Pre-ionization in Helium-Cooled Fast Breeder Reactor," Ph.D dissertation, University of Florida (1971)

6. H. Zinko, "Experimental Investigation of Conductivity-Lifetime in a Helium Aftergrow Plasma," Proc. 5th Int. Conf. on MHD Electrical Power Generation, Vol.2, 25 (1971)

7. C.B. Leffert, D.B. Rees and F.E. Jamerson, "Noble Gas Plasma Produced by Fission Fragments," J. Appl. Phys., Vol.37, 133 (1966)

8. D.B. Rees, C.B. Leffert and D.J. Rose, "Electron Density in Mixed Gas Plasma Generated by Fission Fragments," J. Appl. Phys., Vol.40, 1844 (1969)

9. J.E. Deese and H.A. Hassan, "Anaysis of Nuclear Induced Plasma," Proc. of Princeton University Conference on Partially Ionized and Uranium Plasma, 52 (1976)

10 W.H. Ellis and K. Imani, "Kinetic studies of Fission Fragment, ^{3}He(n,p)t, and Gamma Ray Produced Plasmas," Proc. 2nd Symp. on Uranium Plasma, Atlanta (1971)

11. J.C. Wu, J.R. Williams, J.C. Handley and B.P. Cooper, "Some Properties of a Flowing Uranium Hexafloride Seeded Plasma," Proc. 2nd Symposium on Uranium Plasmas:Research and Applications, Atlanta, Georgia, 83 (1971)

12. W.H. Ellis and M.J. Baumgartner, "Pulsed Ion Chamber Diagnostics Studies on Nuclear Seeded Plasma," ANS Trans., Vol.56, 84 (1988)

13. N.L. Kracella, "The Emission Characteristics of Uranium Hexafluoride at High Temperature," Proc, Partially Ionized and Uranium Plasma, 146 (1976)

14. W.C. Roman "Properties of Radio-Frequency Heated Argon Confined Uranium Plasma," Proc, Parcially Ionized and Uranium Plasma, 136 (1976)

15. J.H Lee et al.,"Production of Fissioning Uranium Plasma to Approximate a Gas-Core Reactor Conditions," Nuclear Technology, Vol.22 (1974)

16. S.H. Kim and W.H. Ellis, "Voltage Pulse Profile Characteristics with Space Charge of a Loaded Pulsed Ionization Chamber," J. Appl. Phys., Vol.43, No.7, 3027 (1972)

17. B.J. Kaiser, "Applying the Pulsed Ionization Chamber Methodology to Full Range Reactor Power Measurements," Ph.D dissertation, University of Florida (1977)

18. R.D. Evans, "The Atomic Nucleus," McGraw-Hill, Inc. New York (1955)

19. R.A. Gerber and J.B. Gerardo, "Ambipolar-to-Free Diffusion: The Temporal Behavior of the Electrons and Ions," Phys. Rev., Vol A7, 781 (1973)

20. D.R. Eletsky and B.M. Smirnov, "Elementary Nonradiative Processes," Handbook of Basic Plasma Physics I, ed. A.A. Galeev and R.N. Sudan, North-Holland Publishing Company, New York, 49 (1983)

21. D.R. Bates, "Recombination" Case Study in Atomic Physics, Academic Press, Vol.4, 57-92 (1974)

22. H.E. Willhelm, "Recombination in Columns," J. Chem. Phys, Vol 47, 4356 (1967)

23. D.R. Bates and A. Dalgarno, "Electronic Recombination" in Atomic and Molecular Processes, Ed. D.R. Bates, Academic Press, 245 (1962)

24. B. Makin and J.C. Keck, Phys. Rev. Letters, Vol 11, 281 (1963)

25. LND Inc., 3230 Lawson Blvd, Oceanside, New York 11572

26. P.M. Whaley and W.G. Vernetson, "UFTR Reactor Design, Experimental and Operational Characteristics," University of Florida Training Reactor Report, University of Florida (1986)

27. E. Hinnov and J.G. Hirschberg, "Electron-Ion Recombination in Dense Plasma," Phys. Rev., Vol 121, 795 (1962)

28. E. Nasser, "Fundamentals of Gaseous Ionization and Plasma Electronics," John Wiley & Sons, Inc., New York, 172 (1971)

29. S.C. Brown, "Basic data of Plasma Physics," John Wiley & Sons, Inc., New York, (1959)

30. E.T. Dugan, G.E. Welch and S. Kahook, "Ultrahigh Temperature Vapor Core Nuclear Reactor/MHD Generator Rankine Cycle Space Power System," Proc. 24th Intersociety Energy Conversion Eng. Conf. (1989)

31. G.F. Knoll, "Radiation Detection and Measurement," John Wiley & Sons, New York, 55 (1979)

32. C.P. Cannon, "High Voltage Instrument Cables for 650°C, In-Vessel Breeder Reactor Service," IEEE Trans. Nucl Sci., NS-27, 852 (1980)

33. R. Chuse, "Pressure Vessels-The ASME Code Simplified," 5th ed., McGraw-Hill Book Company, New York (1985)

34. G.S. Brady and H.R. Clauser, "Materials Handbook," 12 ed., McGraw-Hill Book Company, NY (1986)

35. C. Collins, S.C.P. Wang, S. Anghaie, "Investigation of High-Temperature Materials for Uranium-Fluoride-Based Gas Core Reactor System," ANS Trans., Vol.57, 84 (1988)

36. E.D. Whitney, D.J. Kim, D.S. Tucker, "A Study of Corrosion-Resistant Materials for Pulsed Gaseous Core Nuclear Systems," Nucl. Technol., Vol.69, 154 (1985)

37. F.F. Chen, "Electrostatic Probes," Plasma Diagnostic Techniques (ed. by R. Huddlestone and S. Leonard), Academic Press, New York (1965)

38. P.M. Chung, L. Talbot and K.J. Touryan, "Electric Probes in Stationary and Flowing plasmas: Theory and Application," Springer-Verlag, New York (1975)

39. National Instruments Corporation, "LabVIEW 2, User Manual," 6504 Brige Point Parkway, Austin, Texas 78730 (1990)

40. D.C. Loughry, "IEEE Standard Digital Interface for Programmable Instrumentation: IEEE Recommended Practice for Code and Format Conventions for Use with ANSI/IEEE Std 488-1978," (1983)

41. Burr-Brown Corporation, "Integrated Circuit Data Book," Vol. 33, International Airport Industrial Park, Tucson Arizona (1989)

42. A. Roth, "Vacuum Technology," North-Holland Publishing Company, New York (1976)

43. Thermcraft, 3950 Overdale Rd, Winston-Salem, North Carolina 27117

BIOGRAPHICAL SKETCH

Won Young Choi was born March 24, 1958, at Pusan, Korea. In February, 1981, he received the degree of Bachelor of Science with a major in nuclear engineering from the Seoul National University, Korea. In February, 1983, he received the degree of Master of Science with a major in nuclear engineering from the Seoul National University.

From 1984 until 1985, he worked for the Korea Power Engineering Company at Seoul, Korea, as a nuclear engineer.

In August, 1985, he enrolled in the Graduate School of the University of Florida. He has been working as a graduate research assistant in the Department of Nuclear Engineering Sciences, Department of Physics, and Innovative Nuclear Space Power Institute. Until the present time, he has pursued his work toward the degree of Doctor of Philosophy. Currently, he is working for Nanoptics Inc., Gainesville, as a project scientist to build a scanning proton microprobe (SPM) which will have the world's highest resolution.

He married the former Haeja Yeon in May, 1985 and has a daughter, Hali. He is a member of Alpha Nu Sigma. He received the James E. Swander Memorial Scholarship Award in 1990.

I certify that I have read this study and that in my opinion it conforms to acceptable standards of scholarly presentation and is fully adequate, in scope and quality, as a dissertation for the degree of Doctor of Philosophy.

William H. Ellis, Chairman
Associate Professor of
Nuclear Engineering Sciences

I certify that I have read this study and that in my opinion it conforms to acceptable standards of scholarly presentation and is fully adequate, in scope and quality, as a dissertation for the degree of Doctor of Philosophy.

Samim Anghaie

Samim Anghaie
Associate Professor of
Nuclear Engineering Sciences

I certify that I have read this study and that in my opinion it conforms to acceptable standards of scholarly presentation and is fully adequate, in scope and quality, as a dissertation for the degree of Doctor of Philosophy.

William G. Vernetson
Associate Engineer of
Nuclear Engineering Sciences

I certify that I have read this study and that in my opinion it conforms to acceptable standards of scholarly presentation and is fully adequate, in scope and quality, as a dissertation for the degree of Doctor of Philosophy.

Isaac Maya
Associate Engineer of
Nuclear Engineering Sciences

I certify that I have read this study and that in my opinion it conforms to acceptable standards of scholarly presentation and is fully adequate, in scope and quality, as a dissertation for the degree of Doctor of Philosophy.

Robert J. Hanrahan
Professor of Chemistry

I certify that I have read this study and that in my opinion it conforms to acceptable standards of scholarly presentation and is fully adequate, in scope and quality, as a dissertation for the degree of Doctor of Philosophy.

Calvin C. Oliver
Professor of Mechanical Engineering

This dissertation was submitted to the Graduate Faculty of the College of Engineering and to the Graduate School and was accepted as partial fulfillment of the requirements for the degree of Doctor of Philosophy.

December, 1991

Herbert G. Bevis
for Winfred M. Philips
Dean, College of Engineering

Madelyn M. Lockhart
Dean, Graduate School